

Yaşar Akdoğan

**SYNTHESIS, CHARACTERIZATION AND CHEMICAL
BEHAVIOUR OF SMALL PARAMAGNETIC Pt SPECIES
INSIDE ZEOLITES STUDIED BY EPR, XAS AND FTIR**

**INSTITUT FÜR PHYSIKALISCHE CHEMIE
DER UNIVERSITÄT STUTTGART
March 2009**

**SYNTHESIS, CHARACTERIZATION AND CHEMICAL
BEHAVIOUR OF SMALL PARAMAGNETIC Pt SPECIES
INSIDE ZEOLITES STUDIED BY EPR, XAS AND FTIR**

Von der Fakultät Chemie der Universität Stuttgart zur
Erlangung der Würde eines Doktors der Naturwissenschaften
(Dr. rer. nat.) genehmigte Abhandlung

vorgelegt von

Yaşar Akdoğan

aus Aksaray, Türkei

Hauptberichter: Prof. Dr. Emil Roduner

Mitberichter: Prof. Dr. W. Kaim

Tag der mündlichen Prüfung: 31.03.2009

INSTITUT FÜR PHYSIKALISCHE CHEMIE
DER UNIVERSITÄT STUTTGART

March 2009

Acknowledgements

First of all I would like to thank **Prof. Dr. Emil Roduner** for giving me the opportunity to become a member of his group and for the supervision of my PhD work. I am very grateful for his warm support, thoughtful guidance and encouragement to perform different techniques and to present our activities on numerous conferences, workshops, and seminars.

I would like to thank **Prof. Dr. Wolfgang Kaim** and **Prof. Dr. Helmut Bertagnolli** for being my PhD committee members.

I wish to thank all my group members for their assistance in the measurements. My special thanks go to **Dr. Herbert Dilger** for helping me with every experimental problem and to **Christopher Jensen** for his support and his great help when I was lost in official jobs. I also thank Christopher very much for the Zusammenfassung part.

I would like to present my deep gratitude to all those who collaborated in this study, making possible to have it done;

- **Prof. Dr. Helmut Bertagnolli, Matthias Bauer** and **Sankaran Anantharaman** for XAS experiments, analyses and fruitful discussions.
- **Prof. Dr. Juan Bartolomé** and **Dr. Fernando Bartolomé** from Zaragoza University for the XMCD measurements and discussions.
- **Prof. Dr. Goutam Kumar Lahiri** from Indian Institute of Technology Bombay for the FTIR discussions.
- **Shadi Yasin** from 1. Physikalisches Institut, Universität Stuttgart, for the SQUID measurements.

A very special thank to **Sankaran** for critical reading and correcting my thesis, and I also thank my wife **Gülçin**, my dear friends **Dr. Ümit Akbey** and **Mustafa Diken** for correcting my thesis.

I thank **Mrs. Inge Blankenship** who helped me for all the administration and official jobs. The support by the mechanical, the electronical and the glassblower workshop is kindly acknowledged.

I would also like to thank The Graduate College “Modern Methods of Magnetic Resonance in Materials Science” for scientific and financial contribution.

I am very glad to thank my friends, especially **Serkan, Orkan** and **Cüneyt** for their support and understanding, and for contributing a pleasant living environment in Stuttgart.

My warm thanks to my friends, in particular **Aynur** who is one of the best friends I have ever met, and **Zeynep, Bahadır, Özlem, Özgür, Ömer, Andreea, Bogdan, Arzu, Oğuz** and **Onur** for sharing good times through three years in Heidelberg.

My special thanks go to my dear cousin **Mustafa Aydoğdu** for being kind and helpful everytime.

I am very grateful to my **parents** for everything that they have done for me.

Finally I would like to thank my beloved wife **Gülçin**, without her love, support and encouragement, this work would not have been completed.

Table of Contents

Acknowledgements.....	3
Table of Contents.....	5
1 Introduction.....	8
2 Basics.....	13
2.1 Zeolites.....	13
2.1.1 NaA, NaX, and NaY zeolites	14
2.1.2 Metal introduction into zeolites.....	17
2.1.3 Acidic and basic sites.....	18
2.2 EPR Spectroscopy.....	19
2.2.1 Introduction.....	19
2.2.2 Magnetic interactions.....	20
2.3 X-Ray Absorption Spectroscopy.....	24
2.4 Types of Magnetic Behaviour	26
2.4.1 Paramagnetism.....	26
2.4.1.1 Curie-type paramagnetism.....	27
2.4.1.2 Curie-Weiss paramagnetism.....	27
2.4.1.3 Pauli paramagnetism.....	28
2.4.2 Diamagnetism.....	28
2.4.3 Ferromagnetism and antiferromagnetism.....	29
2.4.4 Superparamagnetism.....	29

2.5	FTIR Study of CO Adsorption on Pt.....	30
3	Experimental Details.....	32
3.1	Sample Preparation.....	32
3.1.1	Pt cations and Pt dimer.....	32
3.1.2	Pt ₁₃ clusters.....	33
3.1.3	Adsorption of H ₂ and CO.....	34
3.2	EPR Measurements and Simulations.....	34
3.3	XAS Measurements.....	35
3.4	FTIR Experiments.....	37
4	Pt Species in the Pores of NaX, NaY and NaA Zeolites.....	38
4.1	Calcined Pt Species.....	38
4.2	Results and Discussion.....	39
4.2.1	XANES and EXAFS study of Pt in NaX, NaY and NaA.....	39
4.2.2	X-band EPR of Pt ⁺ and Pt ³⁺ in NaX.....	44
4.2.3	Autoreduction control.....	46
4.2.4	Adsorption of hydrogen.....	53
4.2.5	CO adsorption on Pt ⁺ and Pt ³⁺ /NaX.....	54
4.2.6	X-band EPR characterization of Pt ⁺ in NaY.....	57
4.2.7	X-band EPR characterization of Pt ₂ ^{x+} in NaA.....	59
4.2.8	General symmetry conditions.....	63
4.2.9	EPR parameters.....	67
5	Reconstruction of Pt₁₃ Clusters into Pt₂(CO)_m on CO Addition in NaY Zeolite.....	70
5.1	Reactivity of Pt ₁₃ toward CO.....	70

5.2	Results.....	71
5.2.1	XANES and EXAFS study before and after CO adsorption.....	71
5.2.2	X-band EPR measurements.....	76
5.2.3	C-O stretching via FTIR.....	78
5.3	Discussion.....	81
5.3.1	Electronic and coordination structure.....	81
5.3.2	X-band EPR characterization.....	84
5.3.3	Pt-CO bonding.....	86
6	Magnetism of Pt₁₃ Clusters.....	90
6.1	Introduction.....	90
6.2	Experimental Part.....	93
6.3	Results and Discussion.....	94
6.3.1	X-ray absorption spectroscopy.....	94
6.3.2	XMCD measurements.....	97
6.3.3	Fraction of magnetic Pt ₁₃ clusters.....	100
6.3.4	Comparison of XMCD and SQUID results.....	102
7	Summary.....	107
	Zusammenfassung.....	111
	Abbreviation.....	116
	List of Figures.....	120
	List of Tables.....	124
	Bibliography.....	125
	Curriculum Vitae.....	132

1 Introduction

Platinum in zeolites is one of the most widely used catalysts in industrial and scientific areas. Commercially important applications, like the oxidation of CO and residual hydrocarbons in automotive exhaust catalysis, NO conversion into less harmful gases, *e.g.* N₂, hydrogenation in petrochemistry and oxygen reduction in polymer electrolyte membrane fuel cells (PEMFC) are some examples of the areas using supported Pt catalysts [1-5]. Catalytic activity is strongly dependent on the catalyst particle size and increases with decreasing cluster size because the reaction takes place on the surface of the catalyst. The dispersion, which designates the fraction of atoms at the surface, is higher for smaller particles compared to bigger ones. Besides the catalytic activities, small Pt clusters show enhanced magnetism that is not possible in the bulk phase [6, 7]. Therefore, synthesizing uniform small Pt clusters with known geometric and electronic structure has been the aim of the many nanocatalysis studies.

The highly symmetrical icosahedral structure with one of the smallest clusters matching a magic number, 13, can be synthesized in zeolite supercages by means of the so-called “ship-in-a-bottle” method. Recently, a well-defined Pt₁₃ cluster in NaY zeolite has been prepared and its characterization in terms of electronic configuration, structure, and magnetization have largely been elucidated by X-band electron paramagnetic resonance (EPR), extended X-ray absorption fine structure (EXAFS) and superconducting quantum device (SQUID) measurements and additionally supported by density functional theory (DFT) calculations [7, 8]. These Pt₁₃ samples, in principle, would be model systems to understand the catalytic activities and the magnetism of small nanoparticles due to several factors listed below:

- 1) The Pt₁₃ clusters are ideally small monodisperse particles inside the supercages of zeolites.
- 2) The electronic structure of the cluster depends on the zeolite chemical framework.
- 3) The particle density in the sample can be controlled with an initial loading amount, so any interaction between particles can be safely neglected.
- 4) Adsorption of different gases, *e.g.* H₂, O₂, H₂O, CO, and NO, is achievable.
- 5) A highly symmetric icosahedral structure of the Pt₁₃ clusters leads to high spin states.
- 6) The structures of the Pt₁₃ clusters, both hydrogen adsorbed and bare clusters, are identical but magnetic properties are different.

Support polarity and structure are as well important for the cluster formation and catalytic behavior. Since the interaction between Pt atoms and zeolite lattice is unavoidable, it is important to understand the role of zeolite in the synthesis of Pt samples. For example, the Pt₁₃ cluster was synthesized in KL (Si/Al = 3.0) [9], NaY (Si/Al = 2.31) [8] and NaUSY (Si/Al = 3.01) in this study, but the NaX zeolite with lower Si/Al = 1.23 ratio did not yield the Pt₁₃ cluster in spite of having the same structure (faujasite type) like Y and USY zeolite. The cluster preparation steps might be helpful to find out the effect of the zeolite on the cluster formation.

In the first step, the Pt(NH₃)₄²⁺ precursor complex exchanges with Na⁺ cations in the faujasite zeolites by an ion-exchange mechanism. The following oxygen calcination decomposes amino groups and forms mainly Pt²⁺ cations [2]. The Pt²⁺ and Pt⁰ oxidation states are well known in catalytic work [10-13], while its maximum common oxidation state is Pt⁴⁺. Starting from Pt²⁺ in NaY and NaX zeolites, various anionic Pt carbonyl clusters (Chini complexes) can be synthesized [14]. However, Pt⁺ and Pt³⁺ species are less known and are called non-classical oxidation states of Pt. So far, Pt⁺ has been stabilized in NaY after oxygen calcination, followed by gentle hydrogen reduction [15], and Pt³⁺ was stabilized on Al₂O₃ after calcination and evacuation at 623 K [16]. These studies are the only works where the characterization of Pt⁺ and Pt³⁺ in powder samples

using the EPR spectroscopy has been reported. Another method to study Pt^+ and Pt^{3+} is FTIR spectroscopy; new non-classical carbonyls of these Pt species in H-ZSM-5 zeolite were observed [17]. The Pt^{3+} state was well characterized both theoretically and experimentally in single crystals of MgO and Al_2O_3 [18, 19], but only a few studies have been done on Pt oxidation states in powder samples [15-17].

The cluster formation is completed by reducing $\text{Pt}^{\delta+}$ species with hydrogen. Therefore, the products of the calcination are important for the cluster synthesis. After calcination, cations stabilized in NaY are not the same as in NaX and so the Pt_{13} cluster is formed only in NaY, even though it has the same structure as NaX.

The well-defined Pt_{13} clusters (Fig. 1.1) supported in NaY zeolite can interact with gases diffusing through the pores of the zeolite. Their chemical interactions give information about the reactivity and catalytic performance of small Pt nanoparticles which have a size smaller than 1 nm. Surface properties of these small nanoparticles become crucial in heterogeneous catalysis. For example, studying CO adsorption and reaction on well-defined Pt cluster surfaces can help to improve the performance and to reduce the Pt catalyst poisoning by CO in methanol oxidation fuel cells [4].

CO is one of the most frequently used probe molecules to characterize metal particles in catalysis. It can provide information on the size and composition of clusters, and on the oxidation and coordination states of cations [20-23]. For example, the Pt particles with coordination number, $\text{CN} > 5$, supported on SiO_2 are stable under CO atmosphere, but the smaller Pt particles, $\text{CN} < 5$, in LTL zeolite reconstruct into small Pt carbonyl aggregates upon CO adsorption, as shown by EXAFS spectroscopy [24]. Shifts in the frequency of the C-O stretching mode are often used to investigate the electronic properties and geometrical structures of the Pt particles by FTIR spectroscopy [24-26]. In general, two ν (CO) absorption regions around 2000 and 1850 cm^{-1} are assigned to linear and bridge bonding of CO on Pt, respectively. Depending on the values and intensities of the absorption frequencies, Pt-CO is characterized by FTIR.

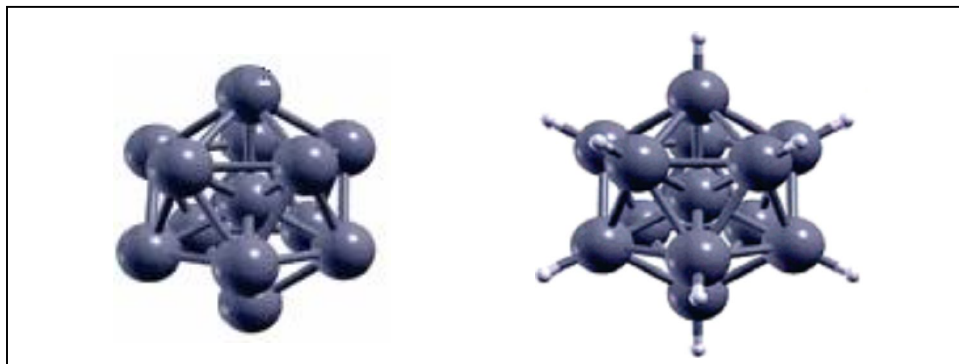


Figure 1.1: Structures of Pt_{13} (left) and $\text{Pt}_{13}\text{H}_{12}$ (right) clusters. Hydrogen atoms bound at the top of surface Pt atoms (right) [8].

EPR is a useful method to characterize paramagnetic samples from one atom species to bulk samples without destroying their structures [27, 28]. Using EPR, information about the sample size, structure, charge and local environment can be obtained. The EPR multiplet obtained from reduced Pt samples after calcination in NaY zeolite obviously shows the formation of Pt_{13} clusters [8]. However, the fraction of Pt atoms that contribute to the paramagnetic 13-atom clusters was found to be less than 1% of all Pt atoms. The remaining Pt could not be detected by EPR, but EXAFS shows that Pt atoms form 13-atom icosahedral clusters and not any different Pt structures. This may be due to the fact that they have EPR silent high-spin states or that they are diamagnetic. Hydrogen adsorption modifies the electronic structure of the cluster, so magnetization is strongly related with the number of chemisorbed hydrogen atoms. However, it is difficult to handle the amount of adsorbed hydrogen in a zeolite. Basically, SQUID results show that Pt_{13}H_m has less magnetization than bare Pt_{13} clusters because each hydrogen atom binds one of the unpaired electrons of the bare cluster; on the other hand it has still a much higher magnetization than other Pt nanoparticles, *e.g.* those obtained in PVP [6] and of course much more than bulk Pt metal [29]. The magnetization would oscillate if it was possible to control the number of adsorbed hydrogen atom after all unpaired electrons of

a Pt₁₃ cluster are paired [30]. X-ray Magnetic Circular Dichroism (XMCD) is an element specific technique and gives information about spin and orbital contributions to magnetization separately. Therefore, magnetization properties of bare Pt₁₃ and hydrogen adsorbed Pt₁₃ clusters can be studied deeply by the XMCD technique. The detected small fraction (< 0.01) of paramagnetic Pt clusters in Pt/NaY samples by EPR could be understood in more detail by XMCD and SQUID experiments.

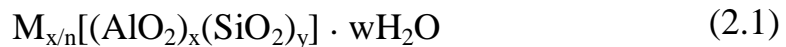
The main aim of this thesis is to investigate paramagnetic Pt species as a single ion, few-atom entities and 13-atom clusters. In the first part of the study, the synthesis of non-classical oxidation states of Pt in zeolites after calcination depending on the zeolite and experimental parameters is discussed (Chapter 4). The isolated paramagnetic Pt cations with oxidation numbers of (1+) and (3+) in NaX, (1+) in NaY, and the paramagnetic Pt dimers in NaA are synthesized and characterized with X-band EPR, XAS and FTIR spectroscopy. Secondly, paramagnetic Pt₁₃ clusters are prepared in the supercages of NaY zeolite and the CO adsorption effect on the structure of Pt₁₃ clusters are observed by taking advantage of the complementary information provided by EPR, XAS and FTIR techniques (Chapter 5). Finally, magnetization of these extraordinary Pt₁₃ samples are discussed using the XMCD technique and SQUID results (Chapter 6).

2 Basics

2.1 Zeolites

Zeolites known as “molecular sieves” are the crystalline microporous solids that exhibit regular pore structures with a pore diameter less than 2.0 nm. They have been known for almost 250 years as a new group of minerals consisting of aluminosilicates in nature that have open structures through which small molecules can diffuse. However, natural zeolites are not optimum substances for catalytic applications because they contain undesired impurities and occur in nonuniform chemical composition. The advent of synthetic zeolites was achieved with methods developed around 1950 by R. M. Barrer and R. M. Milton to provide high performance in large scale catalytic applications. Especially, the commercially important zeolites A, X, and Y were synthesized by Union Carbide Corporation at much lower temperature and pressure than used earlier [31]. For example, the Linde Type A zeolite was the first synthetic adsorbent zeolite to remove oxygen impurity from argon in 1953 [31] and the Faujasite zeolites X and Y were used as catalysts in Fluid Catalytic Cracking (FCC) by the Mobil company for heavy petroleum distillation in 1962. Moreover, in the 1980s and 1990s the synthesis of microporous aluminophosphates made it possible to obtain new structures and compositions different from those of aluminosilicate zeolites [32]. Up to now, ca. 179 different zeolite frameworks have been discovered to serve the chemical industries as adsorbents, selective catalysts, and ion exchangers [33].

Aluminosilicate zeolites are built from three-dimensional networks of SiO₄ and AlO₄ tetrahedra connected together by shared oxygen ions. Although, a SiO₄ tetrahedron is charge balanced, each AlO₄ tetrahedron in the framework has a negative charge because Al is a trivalent atom. The negative charge is balanced by cations, normally from the group of IA or IIA elements, in particular, Na, K, Mg, Ca, and Ba [34]. The framework contains open channels occupied by these mobile cations which are easily exchanged by other cations. Dehydration occurs reversibly at temperatures mostly below ~ 673 K, leaving an intact crystalline host structure. The general chemical formula of an aluminosilicate zeolite framework is best expressed by a crystallographic unit cell as:



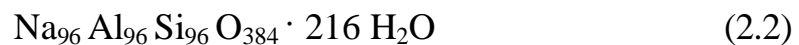
where n is the valence of cation (M), w is the number of water molecules and the ratio y/x changes depends on the zeolite. The total number of tetrahedra in the unit cell is represented by (x + y). Zeolites are usually classified into three classes depending on the Si/Al ratio:

- Low Si/Al ratio (< 5)
- Medium Si/Al ratio (5 to 10)
- High Si/Al ratio (> 10)

2.1.1 NaA, NaX and NaY

Two zeolite structures that are most widely used as catalysts *e.g.* Linde type A (LTA) and faujasite (X and Y) zeolites, will be discussed in detail.

Zeolite A can be obtained from a reaction mixture of 5.03 Na₂O: 1.0 Al₂O₃: 1.35 SiO₂: 229.6 H₂O after heating at 359 K for 2 hours [35]. The unit cell formula is:



with 192 tetrahedra. The unity Si/Al ratio is in agreement with Löwenstein's rule (1954) which claims that a Al tetrahedron must be linked to four Si tetrahedra ($n_{Si}/n_{Al} \geq 1$) [36].

The framework can be described by two types of polyhedra; one is a cubic structure composed of eight tetrahedra, D4R units ($\text{Al}_4\text{Si}_4\text{O}_{16}$), in the centers of the edges of a cube. The other is the truncated octahedron of 24 tetrahedra or β -cages centered at the corners of the cube with a free diameter of 6.6 Å (Fig. 2.1). The center of the unit cell is a cavity (supercage or α -cage) enclosed by β -cages with a diameter of 11.4 Å but the diameter of the 8-ring window of the supercage is only 4.2 Å. The possible cation sites in the A zeolite are shown in Fig. 2.1. Site I in the center of the 6-ring inside the supercage, and site II in the 8 membered window joining two supercages are the cation occupied sites. However, site III opposite to the 4-ring has been found to be of a lower occupancy. In the hydrated NaA zeolite, some water molecules coordinate with the cations inside the supercage and β cage, and some of them form a pentagonal dodecahedron in the supercage [34].

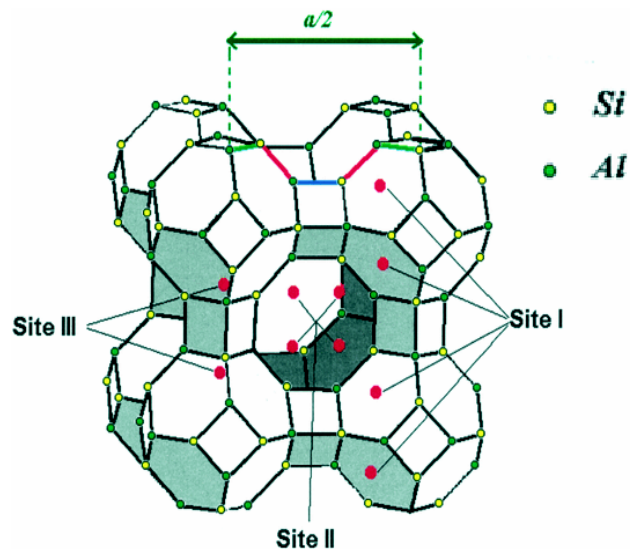
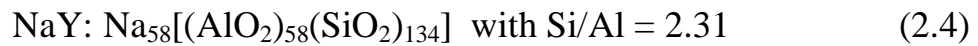
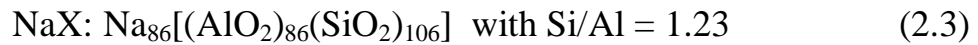


Figure 2.1: Structure of LTA zeolite with possible cationic sites [37].

The faujasite zeolites can be prepared from mixtures of sodium aluminate, sodium hydroxide and water with different Si/Al ratios. Zeolite X with a lower Si/Al ratio ($n_{\text{Si}}/n_{\text{Al}}$

= 1-1.5) was obtained with a composition of 4.2 Na₂O: 1.0 Al₂O₃: 3.0 SiO₂: 180.6 H₂O at room temperature after 16 hours of aging and followed by heating at 373 K for 3 to 8 hours, without stirring [38]. Zeolite Y with its higher Si/Al ratio ($n_{\text{Si}}/n_{\text{Al}} = 1.5-3$) was prepared from 3.4 Na₂O: 1.0 Al₂O₃: 9.5 SiO₂: 136 H₂O at 293 K for 24 hours of aging and heating at 368 K for 24 hours, without stirring [39].

In contrast to LTA, the faujasite aluminosilicate zeolites (X and Y) are characterized by presence of a double 6-ring, D6R, as the secondary structural unit. The X and Y zeolites have the same structures with cubic unit cells containing 192 (Si, Al)O₄ tetrahedra (Fig. 2.2). The double 6-ring or hexagonal prism containing 12(Si, Al)O₄ tetrahedra links truncated octahedra cages (sodalite). The supercage of faujasite is interconnected to four neighbouring supercages through 12-ring windows with a diameter of 7.4 Å, but the inner cage has a diameter of 13Å. Cations are distributed among different types of sites in faujasite depending on the Si/Al ratio (Fig. 2.2). Site I, I' and II are occupied at high Si/Al ratio but some cations are also found in the site III' of NaX. Sites I are found in the hexagonal prism between the sodalite cages and sites I' are located in the sodalite cages facing site I. Site II is the most occupied site found in front of the 6-rings inside the supercage. Sites III and III' are close to the 4-rings in the supercage and in the 12 ring window, respectively with less cation occupation. The unit cell formula of the NaX and NaY used in this work are:



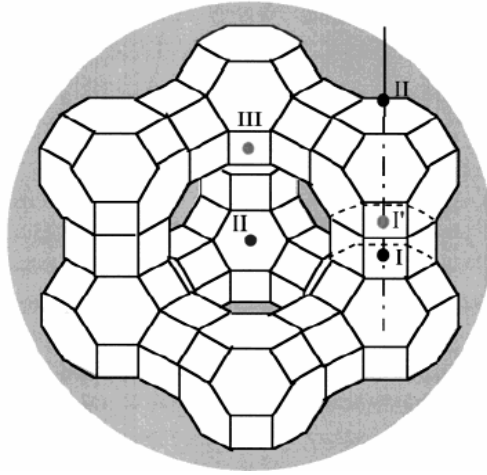


Figure 2.2: Structure of a faujasite zeolite [40].

2.1.2 Metal introduction into zeolites

Two most important techniques used to introduce metals into zeolites are wet impregnation and ion exchange. The impregnation method is more favorable for zeolites with a high Si/Al ratio. It is carried out by addition of metal solution to the zeolite suspension, and by evaporating the water until dryness. Metal cations penetrate into the zeolite together with its anion in the impregnation method. Therefore, for a zeolite with low Si/Al ratio, a high concentration of metal solution is required to overcome the anion-repelling effect of the negative charges around the zeolite pore mouth.

The ion exchange method is the simplest and the most commonly used one for low Si/Al ratio zeolites. Major application areas of the ion exchange method are in the production of laundry detergents, water purification and in catalysts preparation. Since a great variety of zeolites are available with different uniform-porous structures, ion sieving becomes possible. However, the low capacity of the exchange mechanism and lower stability due to high pH values exist.

For ion exchange reactions; a certain amount of support zeolite and metal precursor are dissolved in a solution and then the metal cation exchanged zeolite is filtrated. In this study, only the ion exchange technique was used to introduce the $\text{Pt}(\text{NH}_3)_4^{2+}$ complex into NaA, NaX, and NaY zeolites.

The behavior of ion exchange mechanism depends on the size, charge and chemical environment of the cation. In addition, experimental parameters such as temperature, pH, and concentration of the solution and the structural and chemical characteristics of the zeolite affect the ion exchange mechanism. A higher exchange capacity is expected with zeolites of a low Si/Al ratio but the zeolite structure has a unique property that leads to the cation selectivity and sieving. The NaA zeolite allows the small cations to penetrate the 8-ring into the supercages, however it does not let complex ions such as $\text{Pt}(\text{NH}_3)_4^{2+}$ to go through the cage. In contrast, zeolites X and Y have a bigger supercage diameter, therefore exchange with many cations, including large complex cations and organic complexes can take place. Nevertheless an incomplete exchange can be observed because the sodalite cage's window diameter (2.2 Å) limits the entry of relatively big cations. At room temperature, the exchange rate of Na^+ with $\text{Pt}(\text{NH}_3)_4^{2+}$ cations were found to be 68% in NaY and 71% in NaX [41].

2.1.3 Acidic and basic sites in zeolites

The catalytic behaviour of zeolites is related to their acidic and basic sites. Therefore, the number of these sites and their strengths are as important as structural properties of zeolites. Acidic parts, such as acidic OH groups (Brønsted acid centers), Lewis acid sites and cations as well as basic oxygen atoms (Lewis base sites), basic hydroxyls (Brønsted base sites) and metal clusters play an important role in the electron exchange. Previously it was shown that a decrease in the Al content facilitates the deprotonation and enhances the acidity strength [42]. Lewis acid sites are assigned to threefold-coordinated Al or Si and AlO^+ that are formed upon dehydroxylation and dealumination of zeolites. On the other hand, the most important basic sites are framework oxygen atoms. The fractional negative charge they bear determines the strength of basicity. Therefore, a high Al

contribution and more electropositive cation presence in the framework increase the basicity of oxygen. Table 2.1 lists the average negative charge on the oxygen atoms in the different zeolites and shows its dependence on Si/Al ratio and the cations [43].

Table 2.1: Calculated average charge q_o on oxygen

Zeolite	q_o
CsX	-0.461
NaX	-0.413
KY	-0.383
NaY	-0.352
KL	-0.356

2.2 EPR Spectroscopy

2.2.1 Introduction

The Pauli Exclusion Principle states that no more than two electrons may occupy a given orbital and their spin components must have opposite signs. The orbitals filled by two electrons are ineffective in terms of spin magnetism, because their spin magnetic moments cancel each other. In order to use the electron paramagnetic resonance (EPR), the sample must have at least one orbital containing a single electron, which is a semioccupied atomic or molecular orbital (SOMO).

The idea of EPR is very similar to the more familiar nuclear magnetic resonance (NMR) technique. The magnetic moment that interacts with electromagnetic radiation arises from electron and nucleus in the EPR and NMR, respectively. The first EPR peak was observed by Zavoisky in 1945 from a $\text{CuCl}_2 \cdot 2\text{H}_2\text{O}$ sample [44]. The resonance condition was detected at 4.76 mT for a frequency of 133 MHz with an electron Zeeman factor, g ,

of approximately 2. Nowadays, higher frequencies and higher magnetic field EPR equipments are available as continuous wave and non continuous (pulse) wave.

The technique that measures resonant absorption of electromagnetic radiation between electron dipoles is called either electron paramagnetic resonance (EPR) or electron spin resonance (ESR). The electron magnetic dipole arises mainly from its spin angular momentum with a small contribution from orbital motion. ESR is a measurement of only electron spin angular momentum, whereas EPR takes into account contributions from orbital motion plus spin angular momentum.

2.2.2 Magnetic interactions

The magnetic moment and angular momentum are related to each other by the equation:

$$\mu_z = iA = \pm \frac{qv\pi r^2}{2\pi r} = \pm \frac{q}{2m} mvr = \frac{q}{2m} I_z \quad (2.5)$$

where i is the effective circulating electric current (charge flow per unit volume ($qv/2\pi r$), q is the charge of a particle of mass m , v is the rotating velocity), A is the area of the circle πr^2 and I_z is the orbital angular momentum of the particle about the axis z . By using Eq. 2.5, the free electron spin magnetic moment μ_{ez} is given by:

$$\hat{\mu}_{ez} = -g_e \beta_e \hat{S}_z \quad (2.6)$$

where we have chosen the axis z along the external magnetic field B , and g_e is the free electron Zeeman (correction) factor:

$$g_e = 2.0023193043617(15) \quad (2.7)$$

one of the most accurately known physical constants. β_e is the Bohr magneton and equals to $9.27400949 \times 10^{-24} \text{ JT}^{-1}$, and \hat{S}_z is the electron spin operator.

The interaction between the magnetic moment and B , is defined by the energy $U(B)$:

$$U = -\boldsymbol{\mu}^T \cdot \mathbf{B} = -\mathbf{B}^T \cdot \boldsymbol{\mu} = -|\boldsymbol{\mu}\mathbf{B}| \cos(\boldsymbol{\mu}, \mathbf{B}) \quad (2.8)$$

where $(\boldsymbol{\mu}, \mathbf{B})$ represents the angle between $\boldsymbol{\mu}$ and \mathbf{B} [45]. In the presence of an external magnetic field, a single unpaired electron has two energy states called Zeeman energy levels because only two possible M_s values (secondary quantum number for the z component of the electron spin angular momentum) are possible. The lower and higher energy states occur when the magnetic moment lines up with the magnetic field and when the magnetic moment is opposite to the magnetic field, respectively (Fig. 2.3). This interaction known as the Zeeman interaction (ZI) is shown by the Hamiltonian:

$$\hat{H}_{ZI} = g_e \beta_e B \hat{S}_z \quad (2.9)$$

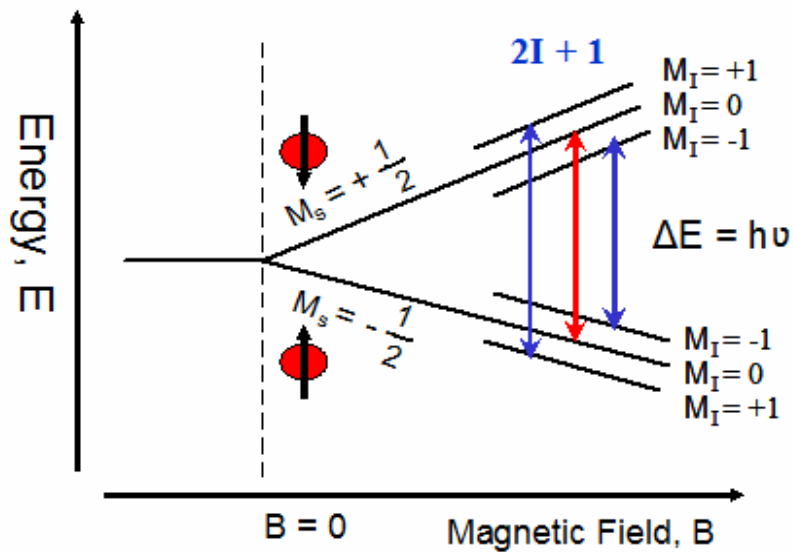


Figure 2.3: Principle of EPR spectroscopy; scanning the magnetic field to get resonance conditions of a system with a nuclear spin number $I = 1$.

So two energy levels occur with $U_\alpha = +1/2 g_e \beta_e B$ and $U_\beta = -1/2 g_e \beta_e B$. At the resonance condition the magnetic component of the microwave energy that is perpendicular to the magnetic field is absorbed to excite the unpaired electron from the lower state to the upper state:

$$\Delta E = h\nu = g_e \beta_e B \quad (2.10)$$

where ν is the microwave frequency.

So far electron orbital motion is not accounted for by the energy calculations. However, the total magnetic moment is composed of the spin and orbital angular momenta. The resultant electron orbital motion produces a magnetic field B_{local} that adds vectorially to the B . The existence of B_{local} perturbs the pure spin ground state; moreover, their coupling causes the spin-orbit interaction. Altogether, these effects produce a deviation of the g factor from g_e and add an anisotropy to the g factor with three principal values g_{xx} , g_{yy} and g_{zz} along three orthogonal axes. Therefore, the new Hamiltonian must be added to the electronic Zeeman terms:

$$\hat{H} = \beta_e B (\hat{L} + g_e \hat{S}) + \lambda \hat{L} \cdot \hat{S} = \beta_e B g \hat{S} \quad (2.11)$$

where λ is the spin-orbit coupling constant, \hat{L} is the total electronic orbital angular momentum operator and g is the effective g -value. The g values of the spectrum with the amount of anisotropy include the electronic and structural information about the atoms or molecules.

Another important coupling arises from hyperfine interactions. Dipole-dipole interaction originates from magnetic moment of the electron and nuclei that have a nuclear spin, I , larger than zero:

$$\hat{H}_{HF} = \hat{S}_z \hat{A} \hat{I}_z \quad (2.12)$$

A is the hyperfine coupling tensor with orthogonal principal values A_{xx} , A_{yy} , and A_{zz} , and \hat{I}_z is the nuclear spin operator. The nucleus with a non-zero nuclear spin number (I) produces a local magnetic field on the unpaired electron and causes an energy splitting

for each value of M_s with $2I + 1$ (Fig. 2.3). The additional energy splitting is observed if the effective nucleus number is more than one, calculated by the equation $2nI + 1$ (n is the number of effective nuclei with a nuclear spin number different than zero). Especially, different isotopes of the same atom with specific nuclear spin numbers are used for the structure determination.

In addition to the hyperfine structure, many systems have superhyperfine structure which is observed when the unpaired electron is affected also by a ligand nucleus ($I \neq 0$) covalently bonded to the central atom.

The magnitude of the hyperfine coupling depends on the distance between the electron (μ_{ez}) and the nuclear (μ_{nz}) dipole moments, the angle between magnetic field and the line joining the two dipoles (θ), as well as the magnitude of the magnetic field. Then the energy of dipole-dipole interaction is given by the following expression [46]:

$$U_{dipolar} = -\frac{\mu_0}{4\pi} \frac{3\cos^2\theta - 1}{r^3} \mu_{nz}\mu_{ez} = -B_{local}\mu_{ez} \quad (2.13)$$

Since, the s electron density at the nucleus is non-zero unlike the p , d , f ,... orbitals that have nodes at the nucleus, the hyperfine interaction for valance s electrons have very large values. The spherical symmetry of s orbitals also provides equal regions for θ with an equal probability, so the hyperfine interaction in the s orbital is isotropic. The isotropic hyperfine coupling constant (A_{iso}) is obtained from the multiplying factor $\hat{S}_z\hat{I}_z$ in the Hamiltonian function in Eq. 2.14 [46]:

$$\hat{H}_{iso} = \frac{2\mu_0}{3} g g_n \beta_e \beta_n |\psi(0)|^2 \hat{S}_z \hat{I}_z \quad (2.14)$$

$$A_{iso} = \frac{2\mu_0}{3} g g_n \beta_e \beta_n |\psi(0)|^2 \quad (2.15)$$

where $|\psi|^2$ is the probability of finding the electron in a unit volume at the nucleus and β_n is the nuclear magneton.

The eigenvalues of \hat{S}_z and \hat{I}_z are M_S and $M_I = \pm \frac{1}{2}$. Therefore, the term of $\hat{S}_z \hat{I}_z$ is found to be $\pm \frac{1}{4}$.

The tabulated parameters $\langle r^{-3} \rangle$ calculated for the valance p, d, f electrons and $\psi^2(0)$ for s electrons of the most abundant nuclei for all elements from helium to bismuth are listed in Ref. [47]. The fraction of unpaired spin density in a molecule for individual atoms can be calculated by division of experimental hyperfine parameters of atoms into their tabulated values.

2.3 X-Ray Absorption Spectroscopy

X-ray absorption spectroscopy (XAS) is a synchrotron-based characterization technique that can be divided into X-ray absorption near edge structure (XANES) and extended X-ray absorption fine structure spectroscopy (EXAFS). In recent decades, XAS has been used increasingly for the study of catalysts, since it can probe features of electronic structure which are related to catalytic activity. In particular, XAS can determine the degree of partially unoccupied d -electron states which plays a main role in the catalytic activities of the transition metals.

The absorption coefficient, μ , obtained from Eq. 2.16, decreases with increasing energy of the incident photon until an absorption edge position:

$$I(E) = I_0(E)\exp(-\mu(E).d) \quad (2.16)$$

where E is the energy of the X-ray beam, d is the thickness of the sample, $I_0(E)$ and $I(E)$ are the incident and transmitted X-ray intensities, respectively.

The X-ray absorption coefficient increases abruptly at the absorption edge. This big jump occurs when the energy of the X-ray photons is equal to that required to excite electrons from a core level to the first empty electronic state. After the absorption edge the absorption coefficient decreases again with increasing energy, until the next absorption

edge is reached. Edges are called by the letters K, L, M, etc. to reflect the particular electronic shell from which the electrons are excited by the X-ray photons.

The L shell electrons produce three different absorption edges; the L_I edge is due to the excitation from $2s$ ($l = 0$) states, and the L_{II} and L_{III} edges are due to the excitation from $2p$ ($l = 1$) states. The L_{II} and L_{III} edges are much more interesting for the electronic studies of metal catalysts. The orbital and spin angular momentum vectors are opposed to one another for the $2p$ states giving rise to L_{II} edges ($l = 1, s = -1/2$, and $j = l + s = 1/2$), and parallel for the L_{III} edges ($l = 1, s = 1/2$, and $j = l + s = 3/2$). The energies of the L edges decrease in the order $L_{III} > L_{II} > L_I$ [48].

Non transition metals such as copper and gold have completely filled d states; therefore the excitation occurs in these samples from p states to continuum states which fit to an arctangent function at the L_{III} and L_{II} edges [49]. But transition metals such as nickel and platinum, with incomplete d states, have more complex L_{III} and L_{II} edges consisting of so called “white lines” overlaid on the arctangent function. The white lines indicate the excitation of $2p$ electrons to unfilled d states in the valance band. As expected, there is a progressive increase in the integrated area of the white line, corresponding to an increase in the number of unoccupied d states (Fig. 2.4).

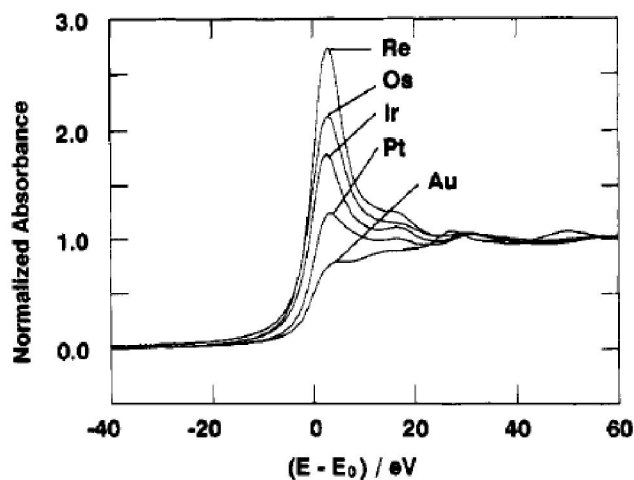


Figure 2.4: Normalized XANES spectra comparing the L_{III} absorption edges of the $5d$ metals Re through Au [50].

If the central atom that absorbs X-ray photons is not isolated, but found in a molecule, the absorption coefficient above the absorption edge displays a fine structure termed as extended X-ray absorption fine structure (EXAFS). The excited electron (photoelectron) which has a significant kinetic energy is scattered by neighbor atoms. In the EXAFS region, the photoelectron wave and new waves originating from each scattering steps are superimposed. Therefore, the interference of the initial and scattered waves, leading to alternating constructive and destructive interfaces, causes oscillations in the absorption coefficient - X-ray energy spectrum. The analysis of the EXAFS oscillations can provide information about the type and the number of neighboring atoms and their distances from the absorbing atom.

An important feature of X-ray absorption is that it provides element-specific information. However, if two or more types of the same atom are present, XAS displays a linear combination of all individuals. This aspect limits the usage of XAS in systems with atoms in variable sites, *e.g.* in zeolites.

2.4 Types of magnetic behavior

Every material shows magnetic behavior with different origins which can be studied with temperature and applied magnetic field. Two important magnetic measurements determine the magnetism of samples;

$M(H)$: magnetization as a function of applied magnetic field at constant temperature,

$M(T)$: magnetization as a function of temperature at the constant magnetic field

where H is the applied magnetic field, and T is the temperature.

2.4.1 Paramagnetism

Paramagnetic samples have a permanent magnetic moment due to the presence of one or more unpaired electrons which are attracted by an applied magnetic field. A plot of $M(H)$ at a fixed temperature has three important features for a paramagnetic sample.

- 1) The curve is linear, the magnetization increases linearly with the magnetic field.
- 2) The line passes at zero.
- 3) The magnetization is reversible, the same curve is obtained when increasing and decreasing the magnetic field.

The magnetic susceptibility χ , which is given by $\chi = M/H$, is obtained when the $M(H)$ curve is linear. Paramagnetic samples have a positive susceptibility due to a parallel alignment of magnetic moments when the magnetic field is applied. But, of course alignment is affected by temperature. The magnitude and temperature dependency of the susceptibility determine the origin of the paramagnetism.

2.4.1.1 Curie-type paramagnetism

For a Curie-type paramagnet, there is a competition between the applied magnetic field and the temperature. While the magnetic field tries to align the magnetic moments in a parallel direction, the temperature disrupts this alignment. This relation could be figured out in the plot of $1/\chi_m$ versus T where χ_m is the molar susceptibility. The slope of the curve is equal to $1/C_m$, and the molar Curie constant (C_m) is given by:

$$C_m = \frac{\mu_{eff} N_A}{3k_B} \quad (2.17)$$

where μ_{eff} is the effective magnetic moment, N_A is the Avogadro's number and k_B is the Boltzmann's constant, $1.38 \times 10^{-23} \text{ JK}^{-1}$.

2.4.1.2 Curie-Weiss paramagnetism

If an interaction between the magnetic moments of different atoms (exchange interaction) exists, it can align either the magnetic moments parallel to the applied field or not. Then, temperature dependent susceptibility $\chi(T)$ changes from C/T and is given by:

$$\chi_{CW} = C/(T-\Theta) \quad (2.18)$$

where χ_{CW} is the Curie-Weiss susceptibility and Θ is called the Curie-Weiss temperature. The strength of the interaction between the magnetic moments determines the Curie-Weiss temperature, and Θ is bigger than zero ($\Theta > 0$) when the interaction helps to align adjacent moments in the same direction, and less than zero ($\Theta < 0$) when the interaction helps to align adjacent moments opposite to each other. Therefore, there is a net ferromagnetic interaction between moments when $\Theta > 0$, and there is a net antiferromagnetic interaction when $\Theta < 0$. The plot of $1/\chi$ versus T for Curie-Weiss behavior is different than that for Curie behavior, the line intercepts at a temperature unequal to zero ($\Theta > 0$, $\Theta < 0$). In the ferromagnetic interactions, the transition to paramagnetism occurs at $T = \Theta$, known as the Curie temperature (T_c). On the other hand, for an antiferromagnet, this transition is seen at $T = |\Theta|$, which is called Néel transition (T_n).

2.4.1.3 Pauli paramagnetism

Pauli paramagnetism is rather small and temperature independent, quite different than Curie behavior. When the metal is placed in a magnetic field, electrons with a spin parallel to the magnetic field have a lower energy than those with a spin opposed to the magnetic field. Those electrons on the top of conduction bands reorient themselves in the magnetic field and make a difference between spin up and spin down electron numbers which causes paramagnetism. But the difference is too small; therefore the magnetic susceptibility has a positive small value.

2.4.2 Diamagnetism

Diamagnetism is present in every matter whether it has paired or unpaired electrons. The change in orbital motion of electrons by applied magnetic field gives rise to a diamagnetic susceptibility. Diamagnetism is a very small magnetization which opposes the magnetic field, therefore it has negative susceptibility. Also, it is temperature independent.

2.4.3 Ferromagnetism and antiferromagnetism

A ferromagnet has a spontaneous magnetization even without an applied magnetic field. Usually, the ferromagnetic samples are composed of many magnetic domains with uniform magnetization. Below the Curie temperature (T_c), the magnetic moments of domains are all lined up in the same direction, thus they behave like one very large magnetic moment in a long range order. It is the strongest type of magnetism having a distinctive $M(H)$ curve. The $M(H)$ curve is not linear, and the behavior is irreversible which is called magnetic hysteresis. The magnetization reaches a maximum value known as the saturation magnetization (M_s) with external magnetic field. But, reducing the magnetic field to zero, magnetization does not follow the same curve and it reaches a value called remanent magnetization (M_{rem}). The M_{rem} values of the ferromagnetic samples are important for applications like magnetic recording and magnetic transformer cores.

The magnetic moments in an antiferromagnet line up in opposite directions to each other. Therefore, neighboring magnetic moments cancel each other, resulting in relatively small magnetization but in a long range order.

2.4.4 Superparamagnetism

A ferromagnetic material below a certain critical size (radius < 1.5 nm) constitutes a single domain particle which stays in a uniform magnetization for any applied magnetic field [51]. At low temperatures, all spins of single domains are coupled in a fixed direction creating as a large magnetic moment, but high temperatures (blocking temperature, T_b) overcome the anisotropy energy and these coupled moments behave like individual spins in paramagnetic samples [52]. Because of the large magnetic moments of domains, saturation is observed even in a lower external field. Furthermore, the angle between the spin and the external magnetic field is not quantized but can take any value. In contrast to paramagnetic materials, their saturation behavior is given by the Langevin function instead of the Brillouin function [52].

2.5 FTIR Study of CO Adsorption on Pt

The most frequently used FTIR probe molecule is CO which has a high dipole moment connected with the CO stretching vibration [53]. Although, the CO adsorption on alkali and rare earth metal surfaces is normally dissociative [54], it is predominantly molecular on *d*-metal surfaces and the strength of the M-CO bond is relatively weak. Characterization of supported or unsupported transition metals has often been studied by the adsorption of CO followed by infrared spectroscopy [55-58]. The IR spectrum obtained after CO adsorption on platinum samples generally gives two $\nu(\text{CO})$ absorption regions: high frequencies of the stretching vibrations above wavenumbers of 2000 cm^{-1} are assigned to linearly adsorbed CO on a single Pt atom, while wavenumbers around 1850 cm^{-1} and 1800 cm^{-1} characterize the adsorption of CO bridged on two and three Pt atoms, respectively. The intensity of the CO bridging bands is often very weak compared to that of linear bands which shows that CO linear bonding on Pt is more favored.

The CO bonding on transition metal surfaces is explained by the Blyholder model which considers molecular orbitals [59, 60]. The chemical bond between CO and Pt consists of the bonding 5σ and the antibonding $2\pi^*$ orbitals of CO versus Pt orbitals. A partial electron transfer from the 5σ CO lone pair orbital to the empty $d\sigma$ Pt orbitals strengthens the Pt-CO bond. At the same time, electron backdonation from the filled Pt $d\pi$ orbitals to the CO $2\pi^*$ orbitals leads to a weakening of the C-O bond, *i.e* a lowering of the $\nu(\text{CO})$ vibration. Therefore, the C-O stretching frequency depends on the properties of the bonded Pt atom properties:

- 1- The backdonation decreases with higher oxidation states of Pt, therefore CO linearly adsorbed on $\text{Pt}^{\delta+}$, shows higher wavenumbers ($>2100\text{ cm}^{-1}$) than for Pt^0 ($<2100\text{ cm}^{-1}$) [17, 23, 61].

- 2- In the Pt, *d* electrons are shared with coordinated Pt atoms, therefore the back donation decreases ($\nu(\text{CO})$ increases) with the increase in the Pt particle size [62, 63].
- 3- High CO coverage increases the $\nu(\text{CO})$ wavenumbers, because the number of electrons coming from Pt decreases for per bonded CO.
- 4- The interaction of the Pt with an electrophilic or nucleophilic compound changes the electron density in the Pt. For example, adsorption of an electrophilic compound such as H_2S , SO_4^{2-} or O_2 decreases the electron density of Pt, that reduces the backdonation and increases the $\nu(\text{CO})$ wavenumbers [64-66]. On the contrary, NH_3 adsorption as a nucleophilic compound, decreases the $\nu(\text{CO})$ wavenumbers [67].

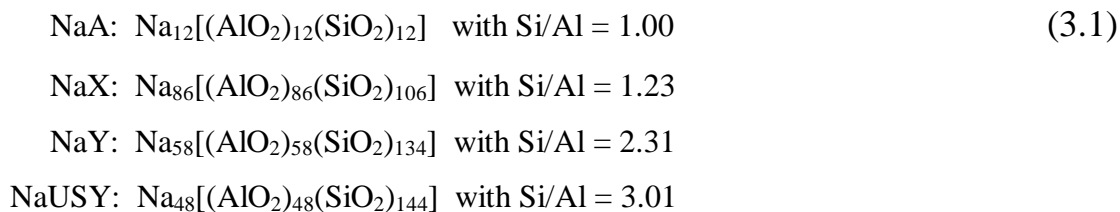
3 Experimental Details

3.1 Sample Preparation

There are three steps applied to prepare samples, which are subsequently ion-exchange, oxygen calcination and hydrogen reduction. Calcination of Pt exchanged zeolites yields Pt cations and dimers. Pt₁₃ clusters synthesized on hydrogen reduction are too air sensitive therefore they are prepared in a glovebox or in situ reaction.

3.1.1 Pt cations and Pt dimer

NaA and NaY zeolites were obtained from CU Chemie Uetikon AG in Switzerland and NaX zeolite was provided by Aldrich. The unit cell compositions are:



These zeolites were calcined in air at 773 K for 14 hours after heating them at a rate of 1 K min⁻¹ to burn off organic impurities. Pt-zeolites were prepared by aqueous ion exchange at 343 K for 48 hours with 3 mM [Pt(NH₃)₄]Cl₂ (Aldrich) solution and 1 g of zeolite in 200 mL of distilled water. Pt in NaUSY was prepared by ion exchange at 343 K for 96 hours because of its higher Si/Al = 3.01 value than others. Under these conditions,

Pt exchanges nearly quantitatively into the zeolite, which was verified by chemical analysis. The zeolites were prepared with Pt loadings of *ca.* 6 wt% in NaY, 1 wt% in NaA and 0.5, 6, 12 wt% in NaX, which corresponds to *ca.* 4.2 Pt ions per unit cell in NaY, 0.7 in NaA, and 0.3, 4.1, and 8.2 in NaX, respectively. The exchanged zeolite was filtered, washed with distilled water to remove Cl^- ions and dried in an oven at 343 K for two days.

Exchanged $\text{Pt}(\text{NH}_3)_4^{2+}$ /zeolites were calcined using different maximum temperatures and heating rates. Calcination was carried out either using a slow ramping rate (0.5 K min^{-1}) or a high ramping rate (1.25 K min^{-1}) in flowing O_2 ($100 \text{ mL min}^{-1} \text{ g}^{-1}$) from room temperature to 573 K, and then holding 573 K for 5 hours (0.5 K min^{-1}) or 1 hour (1.25 K min^{-1}). After cooling to room temperature in oxygen flow, N_2 was applied to purge the residual O_2 in the reactor. Samples were transferred into EPR tubes in a glovebox under N_2 and then evacuated at room temperature for 20 min.

3.1.2 Pt_{13} clusters

Pt/NaY samples were prepared by ion exchange with 3 mM $[\text{Pt}(\text{NH}_3)_4]\text{Cl}_2$ solution to 1 g of NaY zeolite in 200 mL of water for 92 hours at 343 K. The loading of Pt in NaY is 6 wt %, as verified by elemental analysis. Exchanged $\text{Pt}(\text{NH}_3)_4^{2+}/\text{NaY}$ was calcined using a low ramping rate (0.5 K min^{-1}) in flowing O_2 ($20 \text{ mL min}^{-1} \text{ g}^{-1}$) from room temperature to 573 K, and then holding that temperature for 5 hours. After cooling to room temperature in an oxygen flow, N_2 was applied to purge the residual O_2 in the reactor. The reduction was carried out in flowing hydrogen ($25 \text{ mL min}^{-1} \text{ g}^{-1}$) with a heating rate of 6 K min^{-1} to 473 K for 1 hour. The sample cooled to room temperature under hydrogen flow, was transferred into EPR tubes in a glovebox under N_2 and then evacuated. Deuterium exchanged samples were obtained after filling the EPR tube containing the $\text{Pt}_{13}\text{H}_m/\text{NaY}$ sample with 500 mbar D_2 for two days at room temperature. Evacuation of Pt_{13}H_m samples at 408 K for 5 hours using a turbomolecular pump yields the hydrogen desorbed Pt_{13} clusters.

3.1.3 Adsorption of H₂ and CO

The hydrogen adsorption onto activated Pt/NaX was carried out in a closed system. A fixed amount of hydrogen gas was added in three aliquots, and the total number of added H atoms was kept lower than the number of Pt atoms in the sample. Hydrogen adsorption was performed for 10 min at room temperature for Pt³⁺, and for 30 min at 353 K for Pt⁺. Then, samples were evacuated for 10 min.

CO was supplied by Westfalen AG. The carbonylation of the activated sample was performed in 50 mbar CO at 80 K for 10 min in situ in the infrared cell and in the EPR tube at 80 K and 298 K.

The Pt₁₃D_m/NaY (ca. 4 x 10⁻⁵ mol Pt) in an EPR tube is exposed to an excess amount of CO (natural isotopic abundance) or enriched CO (99 atom % ¹³C) gases at an initial 50 mbar pressure (ca. 10⁻⁴ mol) for 10 min at room temperature. The residual CO gas is evacuated over a few minutes from the EPR tube before the measurements. The next excess CO doses of higher pressures (100 mbar, 125 mbar, 500 mbar) are added by the same procedure. In the infrared cell, the Pt₁₃ cluster was exposed to 500 mbar CO for 10 min and then evacuated for 3 min.

3.2 EPR Measurements and Simulations

Continuous wave (cw) X-band EPR spectra were recorded on a Bruker EMX spectrometer with a microwave frequency of about 9.466 GHz at 20 K. To avoid saturation 0.25 mW microwave power was used for 12% loading of Pt in NaX and 1 mW was used for all other experiments. During temperature dependent experiments, all parameters were kept constant and the temperature between 4 and 300 K was adjusted by an Oxford temperature controller. EPR spectral simulations were performed using WINEPR SimFonia, version 1.25. The nuclear spin number of ¹⁹⁵Pt is $I = \frac{1}{2}$ with 33.8% natural abundance, the other isotopes have $I = 0$. For spectral simulations of resolved ¹⁹⁵Pt nuclear hyperfine splitting we sum over the two possible nuclear spin numbers with

the corresponding statistical probabilities, and for the dimer we also account for the possible Pt–Pt nuclear spin combinations.

The spin concentration of a sample was calibrated against a standard sample (Ultramarine blue diluted by KCl) *via* double integration of the derivative signal.

3.3 XAS Measurements

The EXAFS and XANES experiments of calcined Pt/zeolites and Pt₁₃/NaY-CO were done at the XAS beamline at the Ångströmquelle Karlsruhe (ANKA) in collaboration with Matthias Bauer, and at beamline X1 of Hasylab, Hamburg, Germany in collaboration with Sankaran Anantharaman from the group of Prof. Dr. Helmut Bertagnolli, Stuttgart University, respectively. A Si(111) double crystal monochromator was used for all measurements at the Pt L_{III} edge (11.564 keV). The spectra were recorded in transmission mode with ionisation chambers filled with mixtures of nitrogen and argon to achieve optimal absorption. Energy calibration was performed with a platinum metal foil.

The calcined Pt-zeolite samples were embedded in a degassed cellulose matrix and pressed into pellets. A liquid helium cryostat was used to achieve a sampling temperature of 15 K in order to reduce thermal vibrations. Data evaluation started with background absorption removal from the experimental absorption spectrum by subtracting a Victoreen-type polynomial. Due to several inflection points in the absorption edge, the threshold energy E_0 was determined by taking the energy at half of the edge step [68, 69]. To determine the smooth part of the spectrum, corrected for pre-edge absorption, a piecewise polynomial was used. It was adjusted in such a way that the low-R components of the resulting Fourier transform were minimal. After division of the background-subtracted spectrum by its smooth part, the photon energy was converted to photoelectron wave numbers k . The resulting $\chi(k)$ -function was weighted with k^3 and Fourier transformed using a Henning window function. Data analysis was performed in k -space

on Fourier filtered data to remove noise and contributions of multiple scattering. The filtered range was chosen consistently for all analyzed spectra: $\Delta R = 2.4 \text{ \AA}$, $\Delta k = 11 \text{ \AA}^{-1}$. The results of the fitting procedure are given in Table 4.1. They are obtained by adjustment of the common theoretical EXAFS expression:

$$\chi(k) = \sum_j \frac{N_j}{kr_j^2} S_0^2(k) F_j(k) e^{-2k^2\sigma_j^2} e^{-2r_j/\lambda} \sin[2kr_j + \delta_j(k)] \quad (3.2)$$

according to the curved wave formalism of the *EXCURV98* program with XALPHA phase and amplitude functions (N_j : number of neighbour atoms, r_j : distance of atoms j from the X-ray absorbing atom, S_0^2 : amplitude reduction factor, F_j : backscattering amplitude, σ^2 : Debye-Waller like factor, δ_j : overall phase shift) [70]. The mean free path of the scattered electrons was calculated from the imaginary part of the potential (VPI set to -4.00 eV). The amplitude reduction factor was determined to be 0.8 in previous work [7]. Therefore, $S_0^2 = 0.8$ was used for all samples, but the error that can be introduced by the transfer of the reference S_0^2 -value to unknown samples is reflected in the rather large uncertainties of the coordination numbers and Debye-Waller like factors σ . When fitting experimental data with theoretical models an inner potential correction E_f was introduced that accounts for an overall phase shift between the experimental and calculated spectra. In the fitting procedure, care was taken that the number of fitted parameters (N_{pars}) did not exceed the degrees of freedom (N_{ind}) which are calculated according to $N_{\text{ind}} = (2\Delta k \Delta R / \pi)$ [71]. The quality of fit is given in terms of the R-factor according to [72]:

$$R = \sum_i \frac{k^3 |\chi^{\text{exp}}(k_i) - \chi^{\text{theo}}(k_i)|}{k^3 |\chi^{\text{exp}}(k_i)|} \cdot 100\% \quad (3.3)$$

The $\text{Pt}_{13}\text{H}_m/\text{NaY}$ sample was prepared differently by in situ reaction. The oxygen calcined Pt/NaY samples were pressed into pellets (13 mm diameter) and placed in a stainless-steel *in-situ* cell that was connected to a gas flow system. The heating and the

temperature of the cell were regulated using an Eurotherm controller. XAS scans were performed at room temperature following the heating of the sample in a 25 mL min^{-1} flow of H_2 at 473 K for 1 hour, after argon gas flow at 50 mL min^{-1} for 10 min, and after CO (1 bar) gas flow at 25 mL min^{-1} for 20 min. The program AUTOBK implemented in the IFEFFIT [73, 74] program package was used for background correction, normalisation and background subtraction. The extracted EXAFS function was transformed to k -space by choosing suitable threshold energy from half the absorption edge step. The potential and phase shifts in this program were calculated employing Hedin-Lundqvist for the exchange potential and von Barth for the ground state potential.

3.4 FTIR Experiments

The FTIR spectra were recorded on a Magna-IR 560 spectrometer at a spectral resolution of 2 cm^{-1} , accumulating 256 scans. Self supporting pellets ($10\text{-}20 \text{ mg cm}^{-2}$) were prepared from the activated sample powder and treated directly in IR cells. Prior to the adsorption measurements, the samples were heated up to 383 K and evacuated at this temperature overnight.

Self-supporting pellets ($10\text{-}20 \text{ mg cm}^{-2}$) were prepared from the reduced Pt sample powder in air atmosphere. Additional reduction was applied after evacuation at 573 K for 2 hours with 1.5 K min^{-1} heating rate to avoid oxidation and water vapor in the IR cell at 473 K for 1 hour under 100 mbar hydrogen atmosphere. The residual hydrogen was evacuated at room temperature for 1 hour. Subsequently, samples were exposed to CO as explained in part 3.1.3.

4 Pt Species in the Pores of NaX, NaY and NaA Zeolites

4.1 Calcined Pt Species

Electron exchange between Pt and zeolite framework during oxygen calcination of $\text{Pt}(\text{NH}_3)_4^{2+}$ causes formation of Pt cations at different oxidation states, in addition to the well known Pt^{2+} . In this study we show that non-classical oxidation states Pt^+ and Pt^{3+} can be stabilized in faujasite zeolites (X and Y). Aluminum contribution in a zeolite increases the negativity of the framework, therefore higher oxidation states can be stabilized in the zeolite with lower Si/Al ratio zeolites. Calcination at higher temperatures with a fast heating rate causes Pt ion reduction via amino ligand decomposition, a process that is called autoreduction. The autoreduction allowed control of the number of Pt^+ and Pt^{3+} by changing the heating rate. Moreover, by using different zeolites for $\text{Pt}(\text{NH}_3)_4^{2+}$ calcination we could obtain different structures such as Pt dimers. These diverse Pt species formed after oxygen calcination, were studied by EPR for paramagnetic samples. The XANES and EXAFS provided information about the oxidation states and structural information, and the CO adsorption was used as a probe molecule to show the different platinum species by using infrared spectroscopy.

4.2 Results and Discussion

4.2.1 XANES and EXAFS study of Pt in NaX, NaY and NaA

X-ray absorption spectroscopy combining X-ray absorption near edge structure (XANES) and extended X-ray absorption fine structure (EXAFS) was used to extensively characterize Pt samples in NaX, NaY and NaA zeolites after oxygen calcination at 573 K. Fig. 4.1 illustrates the Pt L_{III}-edge XANES spectra of the samples 6% Pt/NaX (1.25 K min⁻¹), 12% Pt/NaX (0.5 K min⁻¹), 6% Pt/NaY (0.5 K min⁻¹), 6% Pt/NaA (0.5 K min⁻¹) calcined in oxygen, and of PtO₂ and Pt foil measured at 15K.

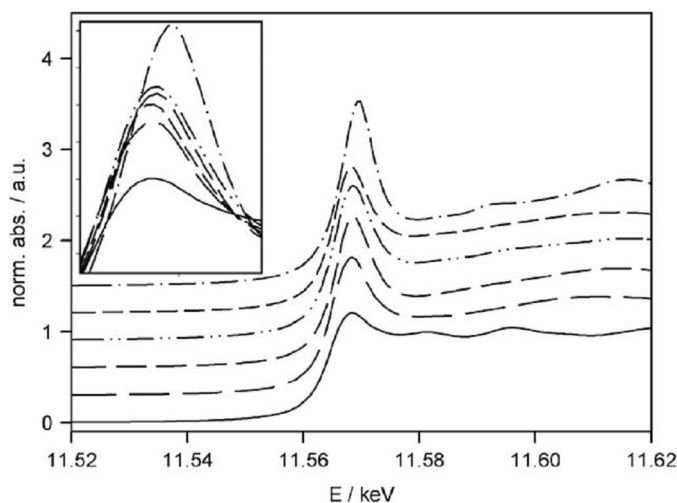


Figure 4.1: Pt L_{III}-edge XANES spectra of zeolite samples after O₂ calcination compared with PtO₂ and Pt foil. From top to bottom: PtO₂ (dotted dashed line), 6% Pt/NaY (short dashed line), 1% Pt/NaA (double dotted dashed line), 12% Pt/NaX, 0.5 K min⁻¹ (medium dashed line), 6% Pt/NaX, 1.25 K min⁻¹ (long dashed line), Pt foil (solid line). The unshifted white lines are shown in the inset. (Measurements and analyses were performed by M. Bauer)

The features in the L_{III} -edge region are result from the transition of $2p_{3/2}$ electrons to empty d orbitals [48]. There is an increase in the intensity of the white line, corresponding to an increase in the number of unoccupied d states. Therefore, the oxidation state of each Pt sample can be compared by the white line intensity. In contrast to the Pt foil, all other spectra exhibit a pronounced white line in Fig. 4.1, with a small shift in the case of PtO_2 in comparison to the Pt/zeolite samples. From the white line intensity of the Pt/zeolite samples it can already be concluded that Pt is in an oxidized state after oxygen calcination [75]. Only the two samples 6% Pt/NaX (1.25 K min^{-1}) and 12% Pt/NaX (0.5 K min^{-1}) can be directly compared to each other due to the common zeolite NaX. The white line intensity of the first sample is lower than that of the second one, which implies that the mean oxidation state of Pt in the first samples (1.25 K min^{-1}) is reduced in comparison to the second one (0.5 K min^{-1}). Nevertheless, further interpretation and comparison of the XANES spectra is not possible without simulations, which are not subject of this work, since the white line is also affected by other parameters such as support and particle size.

Experimental EXAFS functions and Fourier transforms of the filtered spectra of the samples are shown in Fig. 4.2, and the results obtained by fitting these spectra with theoretical models are given in Table 4.1.

The nearest neighbor shell of all calcined samples is comprised of oxygen. The mean Pt-O coordination number in all zeolite samples is about four, and there is no Pt-Pt coordination, which implies that the majority of platinum centers are isolated from each other and only surrounded by oxygen. The Pt-O distance of 2.02-2.04 Å is in good agreement with values reported in literature for Pt ions in zeolites [2].

Including a second oxygen shell is found to increase the quality of fit significantly. Such a shell was not reported in literature so far, but both the coordination number of this shell (which is not expected to be the same in nanoparticles) in the different samples, as well as their Pt-O distances are not in agreement with PtO and PtO_2 [76]. Since platinum oxide structures can be excluded, the platinum ions are coordinated by oxygen of the zeolite

matrix, which constitute the adjusted shells. Molecular oxygen can be excluded from coordinating to Pt since the evacuated samples were prepared under argon atmosphere for the EXAFS measurements. Possibly, also hydroxide ions are involved in charge compensation. Nevertheless, besides the common distance of about 3\AA , obvious differences between the samples exist in the second shell. The samples 6% Pt/NaX, 12% Pt/NaX and 1% Pt/NaA contain approximately two atoms in the second Pt-O shell, while in Pt/NaY only one O-atom is found.

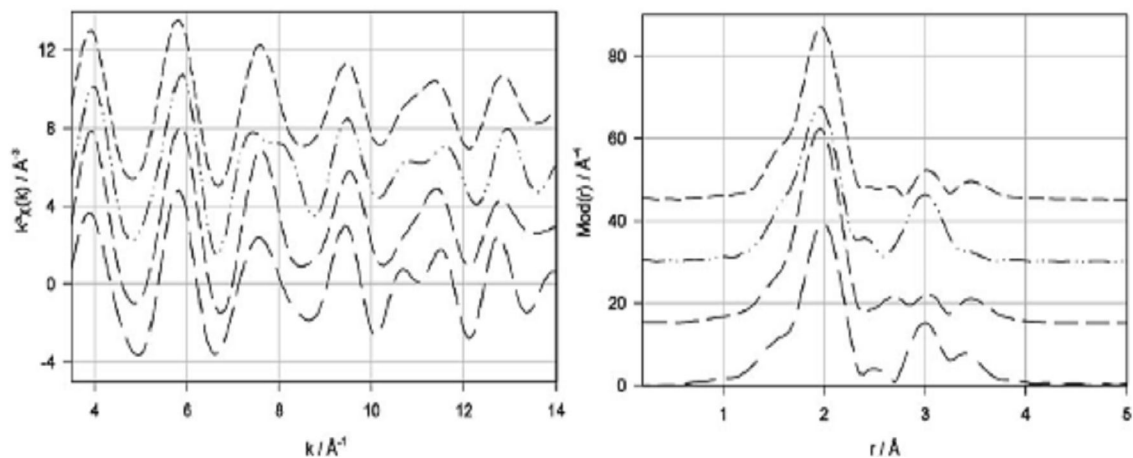


Figure 4.2: Experimental $k^3\chi(k)$ functions (left) and the Fourier transforms of the filtered data (right) of Pt/zeolite samples calcined with oxygen. From top to bottom: 6% Pt/NaY (short dash line), 1% Pt/NaA (double dotted dashed line), 12% Pt/NaX (0.5 K min^{-1} , medium dashed line), and 6% Pt/NaX (1.25 K min^{-1} , long dashed line). (Measurements and analyses were performed by M. Bauer)

Table 4.1: Fit results of all EXAFS data of calcined Pt in zeolites. (Analyses were performed by M. Bauer)

Sample	Abs-Bs ^a	N^b (Bs)	$R^c/\text{\AA}$	$\sigma^d/\text{\AA}$	$N_{\text{ind}}/N_{\text{pars}}^e$	$R\text{-factor}^f$	E_f/eV
6% Pt/NaX (1.25 K min ⁻¹)	Pt-O	3.8 ± 0.4	2.04 ± 0.02	0.074 ± 0.007	16.8/10	18.2	-3.30
	Pt-O	2.1 ± 0.2	3.07 ± 0.03	0.032 ± 0.003			
	Pt-Al/Si	0.7 ± 0.1	3.20 ± 0.03	0.045 ± 0.005			
12% Pt/NaX (0.5 K min ⁻¹)	Pt-O	4.6 ± 0.5	2.02 ± 0.02	0.077 ± 0.008	16.8/10	11.8	-2.97
	Pt-O	2.3 ± 0.2	3.02 ± 0.03	0.105 ± 0.010			
	Pt-Al/Si	0.6 ± 0.1	3.56 ± 0.04	0.045 ± 0.005			
6% Pt/NaY (0.5 K min ⁻¹)	Pt-O	3.9 ± 0.4	2.03 ± 0.02	0.074 ± 0.007	16.8/10	14.8	-4.13
	Pt-O	0.9 ± 0.1	3.03 ± 0.03	0.039 ± 0.004			
	Pt-Al/Si	0.6 ± 0.1	3.52 ± 0.04	0.059 ± 0.006			
1% Pt/NaA (0.5 K min ⁻¹)	Pt-O	3.9 ± 0.4	2.02 ± 0.02	0.081 ± 0.008	16.8/10	18.7	-3.93
	Pt-O	1.8 ± 0.2	3.02 ± 0.03	0.039 ± 0.004			
	Pt-Al/Si	1.0 ± 0.2	3.32 ± 0.03	0.105 ± 0.010			
PtO ^[76] (XRD)	Pt-O	4.0	2.145				
	Pt-Pt	2.0	2.670				
	Pt-Pt	4.0	3.040				
	Pt-O	8.0	3.428				
PtO ₂ ^[76]	Pt-O	5.6 ± 0.2	1.989 ± 0.004	0.002 ± 0.001			
	Pt-Pt	3.7 ± 0.2	3.153 ± 0.002	0.006 ± 0.001			
	Pt-Pt	7.6 ± 0.4	3.556 ± 0.006	0.014 ± 0.008			
	Pt-O	4.5 ± 0.6	3.695 ± 0.006	0.005 ± 0.002			

^a Abs = X-ray absorbing atom, B_s = backscatterer. ^b Coordination number. ^c Interatomic distance Abs-Bs. ^d Debye-Waller like factor. ^e N_{ind} = number of independent parameter (maximal number of variables), N_{pars} = Number of fitted parameter, $N_{\text{ind}} > N_{\text{pars}}$ needs to be maintained in a fit. ^f Quality of fit.

However, also between the two Pt/NaX samples a big difference exists in the Debye-Waller like factor of this shell. With 6% Pt a very small value of σ is obtained, while with 12% a rather large σ is present. Therefore, with higher platinum loading, a much larger disorder in the second oxygen shell is present which can be interpreted by partial population of a second coordination site of the zeolite. This interpretation might also serve as explanation of the slight differences in the white line, since a larger disorder or different surrounding can also affect the electronic structure. In accordance with Ref. [2], a Pt-Al/Si shell could be fitted to all spectra, which further improved the *R*-factor, However from inspection of the Fourier transformed spectra it is observed that again significant differences between the samples exist in this shell. While in the samples 6% Pt/NaX and 1% Pt /NaA the second Pt-O and the Pt-Al/Si shell are superimposed in one signal in the Fourier transformation, in 12% Pt/NaX and 6% Pt/NaY the two signals are well separated. This behavior is reflected in the Pt-Al/Si distances in Table 4.1, where for the first two samples values of 3.20 and 3.32 Å are found, but the last two show elongated distances of about 3.5 Å. This elongation in the case of the NaX samples can be explained by the occupation of different zeolite sites of higher platinum loading.

Finally, attempts to fit a Pt-Pt distance failed for all samples, since neither the exchange of the Pt-Al/Si shell against a Pt-Pt shell, nor the addition of a Pt-Pt shell to the so far considered models improved the fit index at all. Therefore, the platinum centers in the zeolites are isolated and separated from each other. Nevertheless, due to the low sensitivity of EXAFS spectroscopy for contributions of minority species, a small fraction of Pt-Pt pairs cannot be excluded.

In former studies, calcined Pt species were found in the supercages of NaY zeolites up to 633 K, at higher temperature the Pt atom migrates into the sodalite cages [2]. In this study of Pt in NaX and NaY zeolites calcined at 573 K, only four Pt atoms occupy a unit cell, and all of them are located in its 8 supercages. The EXAFS data show bonding of oxidized Pt atoms to approximately four oxygens at ~ 2.0 Å, and the detected support atoms (Al or Si) suggest that Pt occupies the common cationic sites in NaY [2].

4.2.2 X-band EPR of Pt⁺ and Pt³⁺ in NaX

The X-band EPR spectrum of 6 wt% Pt/NaX after oxygen calcination from room temperature to 573 K with 1.25 K min⁻¹ ramping rate, recorded at 20 K, and the corresponding simulation are displayed in Fig. 4.3.

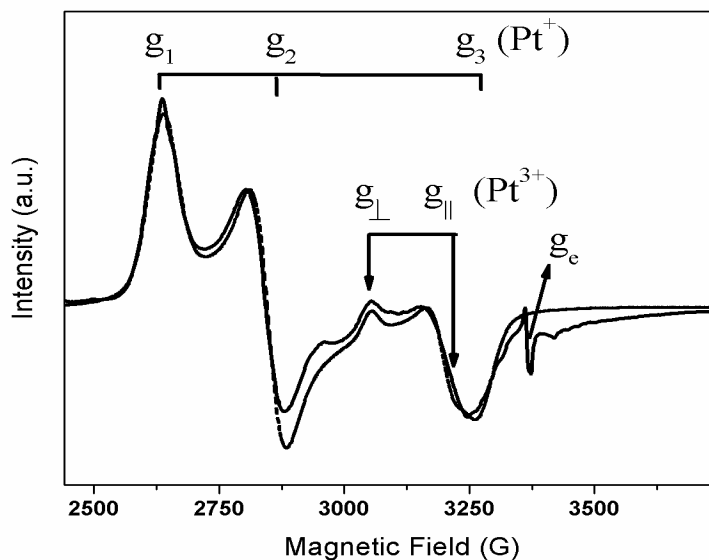


Figure 4.3: EPR spectrum of the 6% Pt/NaX after calcination with a rate of 1.25 K min⁻¹ (solid line) recorded at 20 K and the corresponding simulation (dash-dotted line) based on the parameters listed in Table 4.2 for Pt⁺ and Pt³⁺ ions.

It is well known that after calcination at high temperatures (above 573 K), Pt(NH₃)₄²⁺ complexes transform mostly into Pt²⁺ ions [2]. However, Pt²⁺ is diamagnetic and EPR inactive. The spectra reveal paramagnetic species, and from EXAFS spectroscopy we found that these species are isolated Pt atoms. In Fig. 4.3, there are two different Pt species with different *g* symmetries, one has orthorhombic symmetry and was assigned as Pt⁺ with *g*₁, *g*₂, *g*₃, the other one has axial symmetry which was assigned as Pt³⁺ with *g*_⊥ and *g*_∥. The basis of this assignment is the complementary behavior of the EPR intensities on H₂ reduction as detailed in section 4.2.4. The *g* values are summarized in Table 4.2.

For both species they are much larger than g_e , which means that the unpaired electrons belong to transition metal centers with a more than half-filled d shell [77]. The small additional signal with $g \approx g_e \approx 2.00$ is not related to Pt, it is assigned to the zeolite defects or iron impurities in zeolite [8, 78].

Table 4.2: EPR parameters from simulation of Pt species

Species	g						$ A(^{195}\text{Pt}) $ (MHz)					
	g_1	g_2	g_3	g_{\perp}	g_{\parallel}	g_{iso}	A_1	A_2	A_3	A_{\perp}	A_{\parallel}	A_{iso}
Pt ⁺ /NaX (1.25 K min ⁻¹)	2.56	2.37	2.07			2.33	a					
Pt ⁺ /NaX (0.5 K min ⁻¹)	2.56	2.32	1.91			2.26	394.5	377	321			364.1
Pt ⁺ /NaY (A)	2.59	2.24	2.20			2.34	304.8	< 30 ^a	< 30 ^a			121
(B)	2.70	2.18	2.15			2.34	378.3	< 30 ^a	< 30 ^a			146
Pt ⁺ /NaY (Ref. [15])	2.53	2.32	2.06			2.30	230	242.4	209.5			227.3
Pt ³⁺ /NaX (1.25 K min ⁻¹)				2.21	2.12	2.18	b					
Pt ³⁺ /NaX (0.5 K min ⁻¹)	2.22	2.13	1.99			2.11	<62	<167	<44			91.2
Pt ³⁺ /Al ₂ O ₃ (Ref. [16])				2.22	2.04	2.16				466	466	
Pt ³⁺ /TeO ₂ (Ref. [79])	2.59	2.09	1.93			2.20	571	206.3	137.6			305.0
Pt ₂ ^{x+} /NaA	2.61	2.34	1.94			2.30	219.3	222.9	250			230.7

a) Hyperfine components are too small to be resolved.

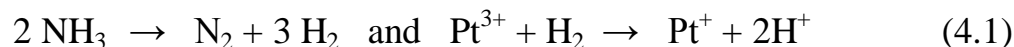
b) Hyperfine components are too small to be resolved, or too anisotropic to be detectable.

Incomplete reduction of Pt after calcination of the exchanged zeolite provides paramagnetic Pt cations. In Al₂O₃, the observation of Pt³⁺ ions was explained by electron transfer from Pt to Lewis acid centres of Al₂O₃ [16]. Moreover, Pt³⁺ could not be stabilized on SiO₂ support that is not acidic, as reported by the same group. This explanation is also consistent with our observation. The higher Al content makes NaX more polar than NaY [80], and furthermore Brønsted acid sites are formed on platinum

autoreduction during calcination. Therefore, the degree of Pt oxidation increases with decreasing Si/Al ratio. The formation of Pt³⁺ and Pt⁺ is possible in NaX (Si/Al = 1.23), but in the case of a larger Si/Al ratio as in NaY (Si/Al = 2.31) only Pt⁺ was stabilized, and finally in Na-USY (Si/Al = 3) no paramagnetic Pt ions were observed. The USY with high Si content cannot produce these non-classical oxidation states through the calcination because the major product of Pt²⁺ does not involve a specific interaction with a basic Si site of the zeolite and does not produce paramagnetic Pt species. Pt/NaY will be discussed in section 4.2.6.

4.2.3 Autoreduction control

Autoreduction is another way to obtain paramagnetic Pt cations during oxygen calcination from other Pt states. Autoreduction may formally be ascribed to hydrogen produced *via* decomposition of amino groups at high temperature, which then reduces Pt cations into lower oxidation states:



It can be controlled by changing the heating rate while applying a high flow of oxygen and the duration of holding the maximum temperature. By applying different calcination procedures, it is possible to synthesize various Pt³⁺/Pt⁺ ratios (Fig. 4.4).

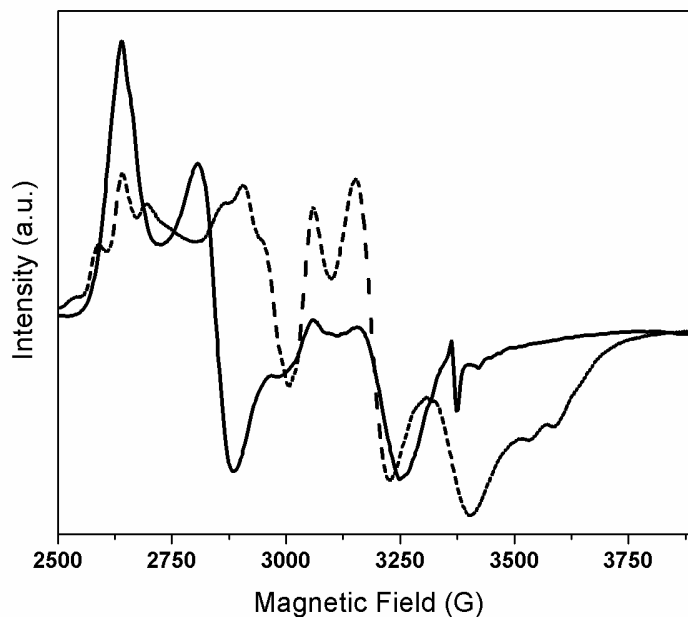


Figure 4.4: Comparison of the EPR spectra of the products of two different calcination rates: 1.25 K min^{-1} (solid line), and 0.5 K min^{-1} (dashed line).

Decreasing the heating rate from 1.25 K min^{-1} to 0.5 K min^{-1} decreases the effect of autoreduction so that the amount of Pt^{3+} increases and the $\text{Pt}^{3+}/\text{Pt}^+$ ratio changes from almost zero to one. In addition, the unpaired electrons of both cations are influenced in a different way by their environment. On slow calcination, the Pt^{3+} ion obtains an orthorhombic symmetry, and Pt^+ is now observed with well resolved ^{195}Pt hyperfine splitting with new g_2 and g_3 values. Simulation yields the spin Hamiltonian parameters with g and A tensors (Fig. 4.5, and Table 4.2).

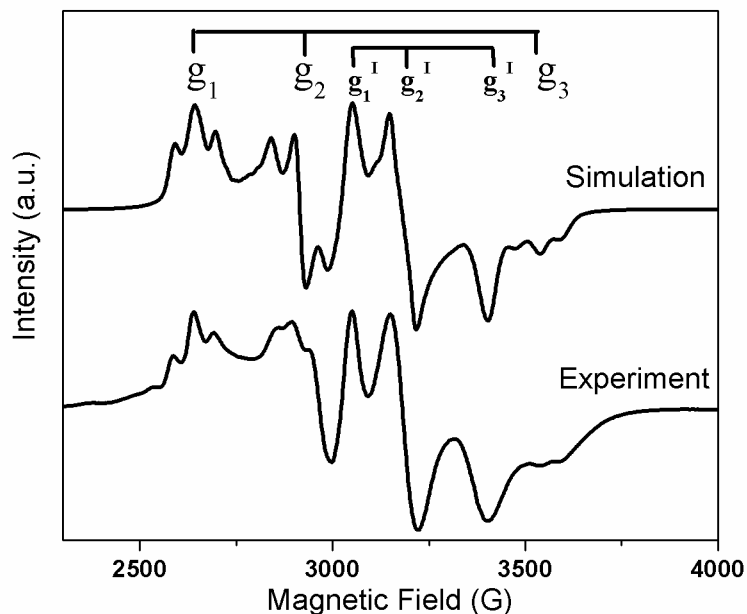


Figure 4.5: Simulation and EPR spectrum of 6%Pt/NaX after O₂ calcination at a rate of 0.5 K min⁻¹ recorded at 20 K, based on the parameters listed in Table 4.2 for Pt⁺ (g_i) and Pt³⁺ (g_i).

The other hyperfine splitting constants of ¹⁹⁵Pt are not well resolved, neither for Pt⁺ (1.25 K min⁻¹) nor for Pt³⁺ (0.5 K min⁻¹). The autoreduction effect is not totally eliminated in spite of using a very low calcination heating rate such as 0.15 K min⁻¹, but the amount of Pt³⁺ is now larger than in the case of a rate of 0.5 K min⁻¹ (Fig. 4.6). Comparison shows that the g values observed here for Pt⁺ ($g_{iso} = 2.33$, 1.25 K min⁻¹ and $g_{iso} = 2.26$, 0.5 K min⁻¹) and Pt³⁺ ($g_{iso} = 2.18$, 1.25 K min⁻¹ and $g_{iso} = 2.11$, 0.5 K min⁻¹) are similar to those reported in literature (Table 4.2). So far, there have been only a few publications of automatically dispersed Pt in zeolites. For example, Pt⁺ was described after oxygen calcination followed by hydrogen reduction in NaY zeolite with comparable g values ($g_{iso} = 2.30$) [15]. However, for the Pt³⁺ case, most of the EPR studies were performed in

single crystals *e.g.* in MgO ($g_{av} = 2.22$) [18], in TeO₂ ($g_{av} = 2.20$) [79], and in the garnet YAlG ($g_{av} = 2.25$) [81], and reports about stabilization of Pt³⁺ in powders are very rare *e.g.* Pt³⁺ in an Al₂O₃ powder gives also similar g values ($g_{iso} = 2.16$) [16].

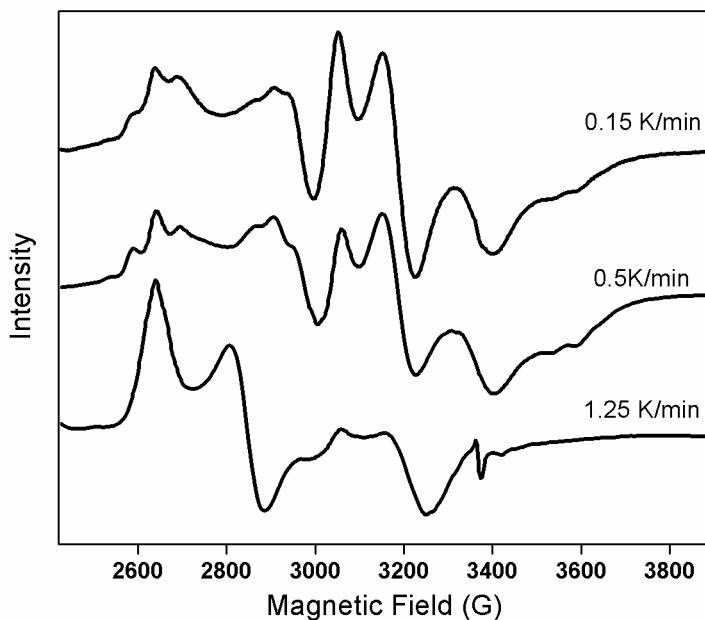


Figure 4.6: Comparison of EPR spectra recorded at 20 K of the products obtained with three different calcination rates: 1.25 K min⁻¹, 0.5 K min⁻¹, and 0.15 K min⁻¹.

Fig. 4.7 shows the EPR spectra of 0.5, 6, and 12 wt% Pt loading in NaX zeolite. The intensities of the Pt signals increase with loading. The fraction of EPR active paramagnetic Pt ions was determined by double integration (Table 4.3). Approximately 7% of the total Pt contributes to the EPR spectrum for 12 and 0.5% loading in NaX, and 4 for 6 wt% Pt. We assume that the remaining EPR silent fraction is mostly the intermediate oxidation state, *i.e.* the diamagnetic Pt²⁺.

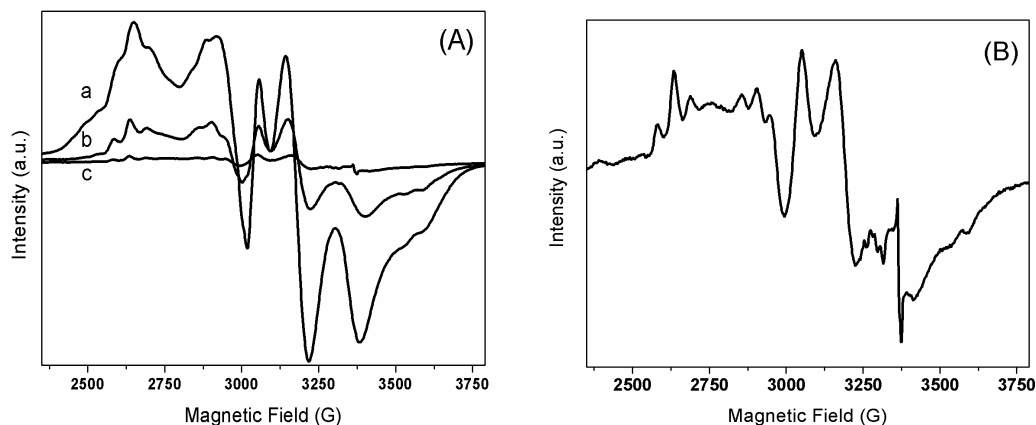


Figure 4.7: X-band EPR spectra of NaX loaded with (A) 12% (a), 6% (b), 0.5% (c) Pt and recorded at 20 K after O₂ calcination with a rate of 0.5 K min⁻¹, and (B) enhanced spectrum obtained with 0.5% Pt/NaX (spectrum (c) from panel (A)).

Table 4.3 Fraction of total EPR active Pt species

Species	wt% Pt	EPR active Pt/%
Pt/NaX	0.5	7
Pt/NaX	6	4
Pt/NaX	12	7
Pt/NaY	6	2
Pt/NaA	1	18

The double integral of the EPR spectrum is proportional to the magnetization. Generally, in a paramagnetic sample, the magnetization is inversely related with temperature (Curie law) and its behaviour can be deduced by measuring the sample at various temperatures. The EPR spectra of Pt/NaX measured at different temperatures are shown in Fig. 4.8. The corresponding magnetization based on double integration is multiplied with temperature and plotted as a function of temperature in Fig. 4.9a. A horizontal line is expected for

Curie-type paramagnetism. The plot of inverse magnetization with temperature is also shown in Fig. 4.9b. The calcined Pt/NaX shows Curie behaviour at low temperatures especially between 15 and 40 K, but at higher temperatures the EPR signal intensity decreases dramatically and deviates from Curie behaviour.

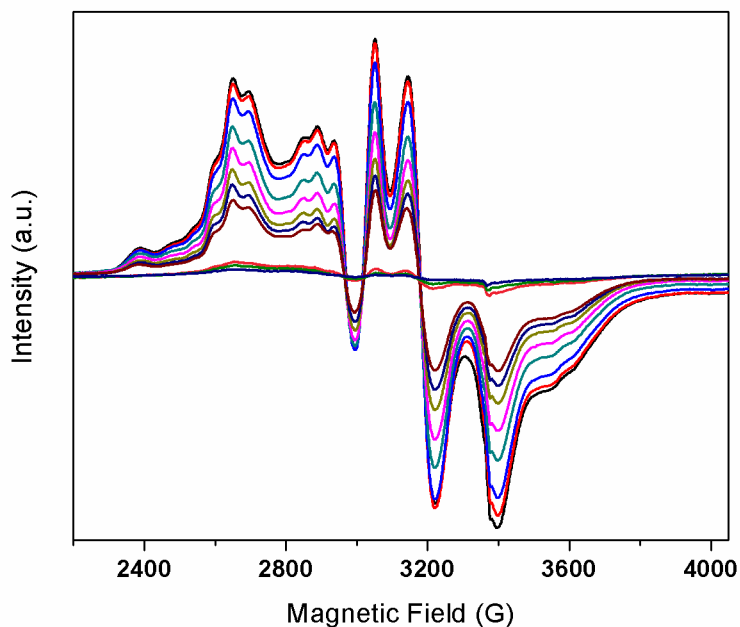


Figure 4.8: X-band EPR spectra of NaX loaded with 6% Pt after O₂ calcination with a rate of 0.5 K min⁻¹, and recorded at 4, 10, 15, 20, 25, 30, 35, 40, 50, 60, and 75 K from top to bottom.

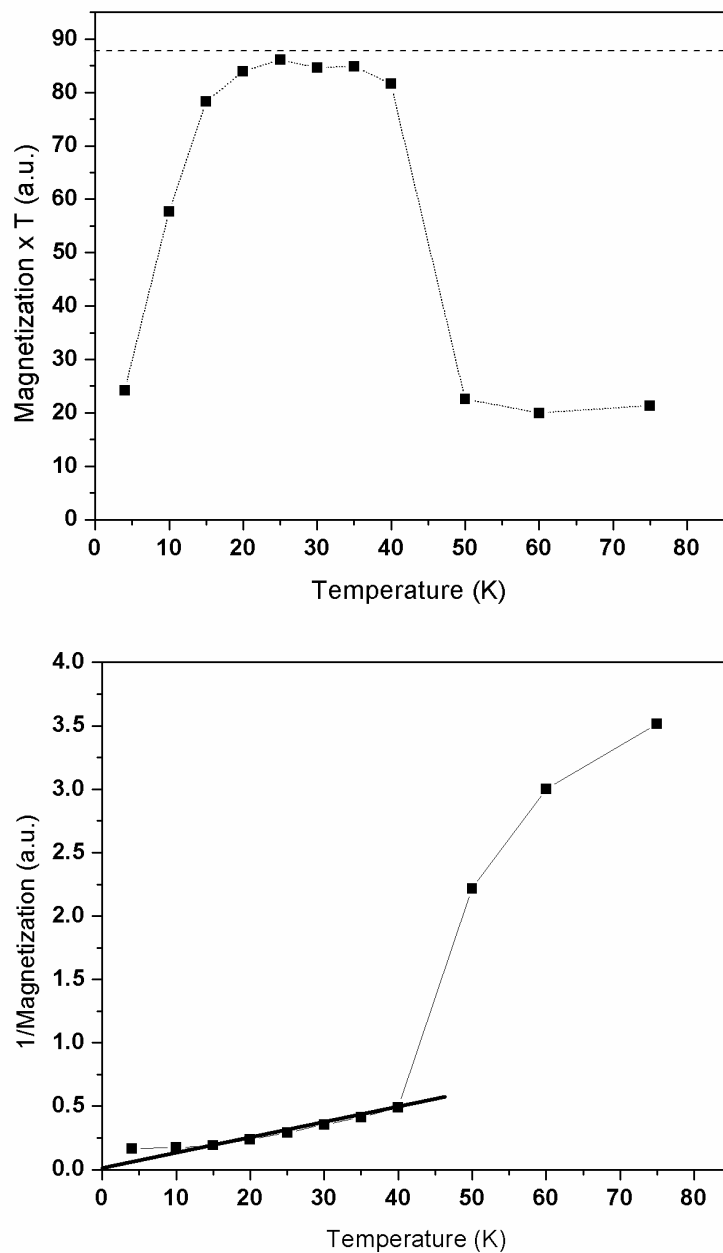


Figure 4.9: (a) Product of magnetization times temperature versus temperature; (b) the reciprocal of magnetization versus temperature plots obtained with doubly integrated EPR spectra of 6% Pt/NaX after O₂ calcination with a rate of 0.5 K min⁻¹ recorded at different temperatures. The broken horizontal line indicates Curie behaviour (a).

4.2.4 Adsorption of hydrogen

Hydrogen adsorption of the calcined Pt/NaX sample was performed with NaX at room temperature in a closed EPR tube with three hydrogen adsorption steps in order to determine the reactivity of Pt^+ and Pt^{3+} and to support further the assignment. Fig. 4.10 shows that the signals which were assigned to Pt^{3+} decrease on addition of hydrogen and the low-field part of signals which were assigned to Pt^+ increase continuously. On addition of hydrogen to Pt/NaX (1.25 K min^{-1}) Pt^{3+} disappears immediately, however, the Pt^+ signal intensity does not change because Pt^{3+} is very low in this case and cannot significantly enhance the Pt^+ . Above 353 K, it is possible to reduce also Pt^+ in NaX, and so the EPR spectrum becomes broader and disappears at higher temperature under formation of clusters. For example, reduction at 473 K under hydrogen flow leads to the formation of Pt_{13}H_m clusters [8].

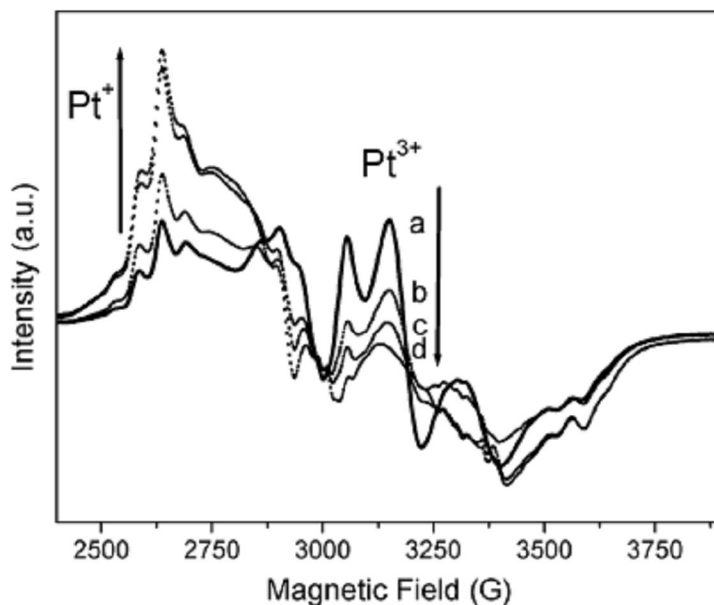


Figure 4.10: X-band EPR spectrum of 6% Pt/NaX recorded at 20 K after O_2 calcination with a rate of 0.5 K min^{-1} (a, solid line), and after H_2 addition to the same sample (a) (b-d, dashed lines).

Hydrogen reduction also gives information about the location of Pt cations inside the zeolite. The kinetic diameter of the H₂ molecule (2.9 Å) is larger than that of the 6-ring window diameter (2.2 Å), so H₂ cannot penetrate into sodalite cages. Since Pt³⁺ easily reduces at room temperature and Pt⁺ reduces further above 353 K it is concluded that all Pt³⁺ and Pt⁺ cations are located inside the supercages.

4.2.5 CO adsorption on Pt⁺ and Pt³⁺/ NaX

CO is the most frequently used IR probe molecule in catalysis, and many studies were conducted using CO with different Pt species. The most often used Pt samples were Pt clusters and Pt(NH₃)₄²⁺. However, studies with Pt cations are limited because CO is also a reducing molecule and it can easily reduce highly oxidized Pt at room temperature. Therefore, in order to characterize all Pt cationic sites, CO adsorption was performed at 80 K. Carbonyl bands at higher frequencies, above 2100 cm⁻¹, are usually assigned to Pt^{δ+}-CO species [13, 17, 61].

Fig. 4.11 shows FTIR spectra of CO adsorption on oxidized 6% Pt in NaX at low temperature, and then following evacuation periods at room temperature. It gives two strong bands at 2216 and 2188 cm⁻¹ and one further signal at 2200 cm⁻¹. The bands at 2216 and 2188 cm⁻¹ are assigned to the ν_s and ν_{as} bands of Pt³⁺(CO)₂ and the 2200 cm⁻¹ band is assigned to ν_{CO} of Pt³⁺-CO. In oxidized samples, there is also a significant amount of Pt²⁺ cations. After CO adsorption at 80 K they lead to a band at 2106 cm⁻¹ that is assigned to ν_{CO} of Pt²⁺-CO. Pt⁺(CO)₂ has symmetric and antisymmetric bands at 2120 and 2091 cm⁻¹, respectively. Bands below 2100 cm⁻¹ are usually assigned to Pt⁰-CO species which are formed during the autoreduction at high temperatures.

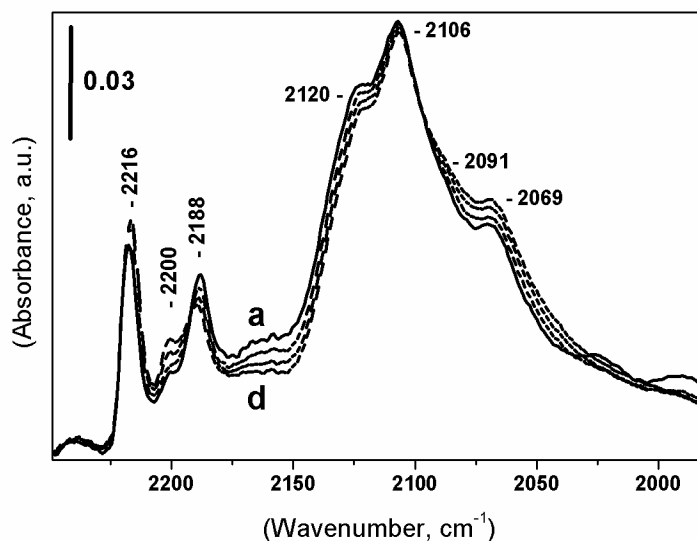


Figure 4.11: FTIR spectra of CO adsorbed at 80 K on O₂ calcined 6% Pt/NaX followed by evacuation at RT for 30 min (a), 40 min (b), 50 min (c), 60 min (d).

Similar carbonyls of platinum were described in H-ZSM-5 zeolite after heating the sample in oxygen at 723 K followed by CO adsorption at low temperature (Table 4.4) [17].

Table 4.4: Carbonyl complexes observed in this study and some literature data

Species	Mode	Carbonyl bands/cm ⁻¹	Sample
Pt ³⁺ (CO) ₂	v _s and v _{as}	2216 and 2188	Pt/NaX ^{a)}
Pt ³⁺ CO	v _{CO}	2200	"
Pt ²⁺ CO	v _{CO}	2106	"
Pt ⁺ (CO) ₂	v _s and v _{as}	2120 and 2091	"
Pt ⁰ CO	v _{CO}	2069	"
Pt ³⁺ (CO) ₂	v _s and v _{as}	2211 and 2175	Pt/H-ZSM-5 ^{b)}
Pt ³⁺ CO	v _{CO}	2195	"
Pt ²⁺ (CO) ₂	v _s and v _{as}	2165 and 2150	"
Pt ²⁺ CO	v _{CO}	2113	"
Pt ⁺ (CO) ₂	v _s and v _{as}	2120 and 2091	"
Pt ⁰ CO	v _{CO}	< 2100	"

a) this work, b) Ref.^[17]

CO adsorption causes reduction of Pt cations at room temperature and enhances the sharp bands at 2075 and 1820 cm^{-1} that belong to the linear and bridged Pt^0 -carbonyl species. However, adsorption at 80 K did not produce any bridge bonding with CO.

Since both the ν_s and ν_{as} bands of $\text{Pt}^{\delta+}(\text{CO})_2$ are IR active these species must have a bent geometry. Interestingly, $\text{Pt}^{2+}(\text{CO})_2$ does not seem to be observed in NaX, in contrast to H-ZSM-5.

EPR results of Pt-CO species also demonstrate the difference of products obtained at low temperature and room temperature CO adsorption in Fig. 4.12. At liquid nitrogen temperature, CO adsorption over Pt^+ and Pt^{3+} /NaX decreases the amount of Pt^{3+} and increases Pt^+ but does not lead to a new paramagnetic species (Fig. 4.12, left).

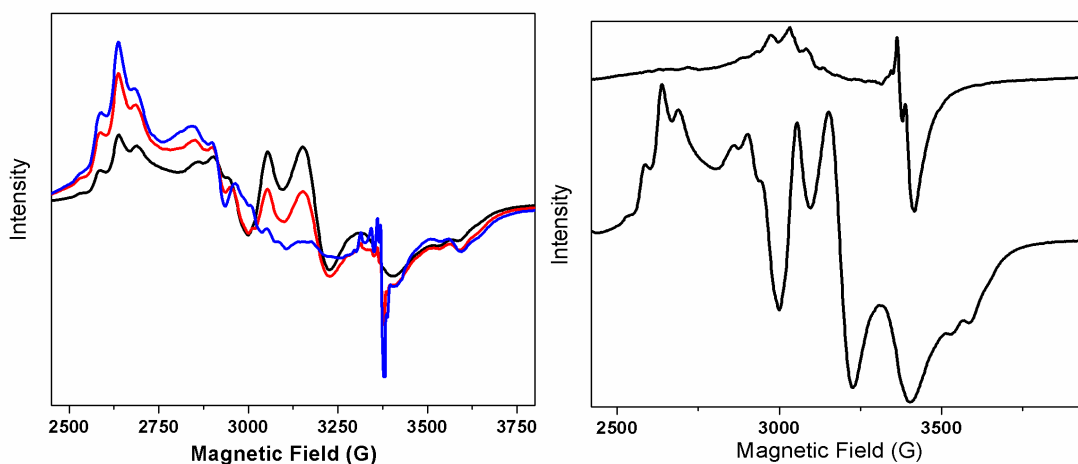


Figure 4.12: Comparison of EPR spectra of the products recorded at 20 K, left: before CO adsorption (black line) and after CO adsorption at liquid nitrogen temperature (red and blue lines), right: before CO adsorption (lower) and after CO adsorption at room temperature (upper).

However, adsorption at room temperature gives a new kind of paramagnetic Pt carbonyl species, which is possibly akin to a Chini complex an anionic platinum carbonyl with the

general formula $[\text{Pt}_3(\text{CO})_6]_n^{2-}$ (Fig. 4.12, right). Such complexes have been produced after the reaction of $\text{Pt}(\text{NH}_3)_4^{2+}$ and Pt^{2+} in NaY and NaX with CO at 298-373K [13, 14].

It is an essential advantage of FTIR adsorptions of CO that paramagnetic as well as diamagnetic species are detected, but while EPR is non-invasive and can be quantified, CO adsorption may lead to further reduction of the sample, and quantification of IR bands is problematic since, depending on the valence of the cation, CO is differently polarized, which changes the CO dipole moment and affects the extinction coefficient.

The present results show that all four oxidation states of platinum from Pt^0 up to Pt^{3+} coexist in NaX. While Pt^{2+} is dominant the other states are not negligible, but the distribution depends, of course, on the preparation. This variable coexistence demonstrates that it must be relatively facile to switch between oxidation states in this material, which is often an essential condition for catalytic activity.

4.2.6 X-band EPR characterization of Pt^+ in NaY

The NaY (Si/Al = 2.31) used in this study differs from NaX (Si/Al = 1.23) only in the Si/Al ratio whereas they have the same structure. Since Si/Al ratio determines the polarity of a zeolite, NaY is less polar than NaX. Therefore, as stated in Section 4.2.2, stabilization of Pt^{3+} is more difficult in NaY. Autoreduction is now the only way to synthesize paramagnetic Pt^+ species.

Activated Pt in NaY has also paramagnetic Pt species. In Fig. 4.13, a wide scan range of an X-band EPR spectrum is seen with the typical iron peak ($g = 4.3$) from small amounts of iron impurities in zeolites in addition to the zeolite or iron signal at $g = 2.0$ [8, 78]. The main signals were obtained with two different calcination procedures, and both of them gave almost the same signals, Pt^+ . The only difference is intensity, calcination with 0.5 K min^{-1} up to 573 K leads to higher intensity. The contribution of EPR active Pt^+ ions is about 2% of the total Pt, as calculated again from double integration of the EPR spectrum (Table 4.3).

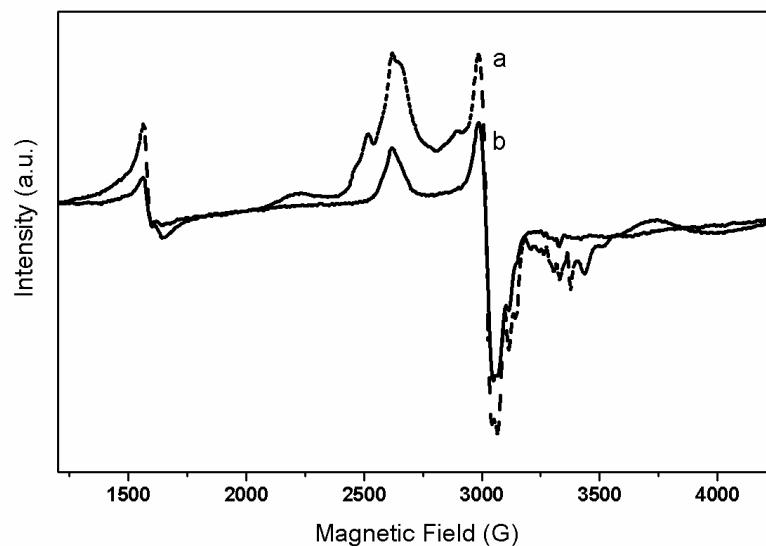


Figure 4.13: X-band EPR spectrum of 6% Pt/NaY recorded at 20 K after O₂ calcination with a rate of (a) 0.5 K min⁻¹ up to 573 K (dash-dotted line), and (b) up to 673 K (solid line).

Fig. 4.14 displays the EPR spectrum of Pt⁺ in NaY zeolite with corresponding simulation. Two different Pt⁺ species were assigned, both with orthorhombic symmetry and their g and A tensors were found by simulation (Table 4.2). Both groups of orthorhombic g values have the same isotropic g value, 2.34, which is very close to the Pt⁺/NaY result after H₂ reduction, $g_{av} = 2.30$ [15], and to the Pt⁺/NaX result after calcination, $g_{av} = 2.33$. In FTIR spectroscopy, the CO adsorption on activated Pt/NaY did not show any Pt³⁺-CO bands above 2200 cm⁻¹, which shows that there is no Pt³⁺ found in the Pt/NaY after calcination.

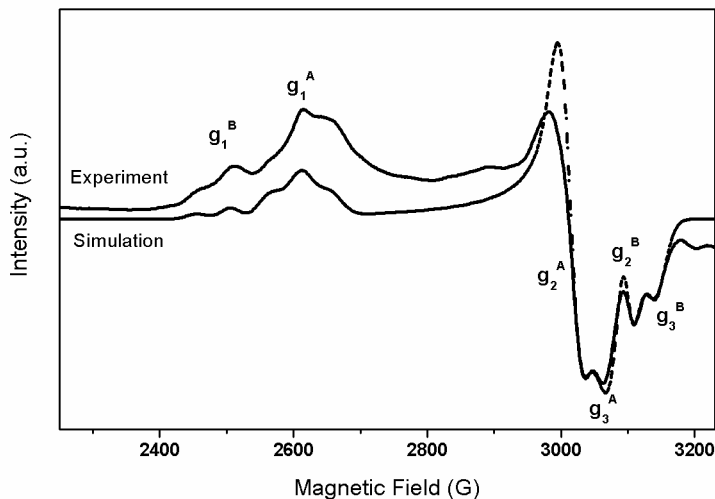


Figure 4.14: Experimental EPR spectrum of 6% Pt/NaY after O₂ calcination at a rate of 0.5 K min⁻¹ recorded at 20 K and simulation based on two different Pt⁺ species A and B with parameters as given in Table 4.2.

4.2.7 X-band EPR characterization of Pt₂^{x+} in NaA

The NaA (Linde type A) zeolite is different from NaX and NaY (faujasites) zeolites in terms of structure, Si/Al ratio and number of counter ions. The β cages of faujasites have a truncated octahedral structure, linked with hexagonal double 6-ring prisms. However, in the NaA zeolite, cubic arrays of β cages are linked by double 4-ring units. The 12-ring diameter of NaX and NaY is 7.4 Å, but the spherical cavities (supercages) have 13 Å diameter, while the 8-ring window of NaA has a diameter of 4.2 Å and spherical cavities with a diameter of 11.4 Å. NaA zeolite has a Si/Al ratio of unity, so it has more exchangeable Na cations than the other two zeolites have. However, the size of the Pt(NH₃)₄²⁺ complex is bigger than the pore entrance of the supercage of zeolite A. The ion exchange capacity is therefore more limited than in other zeolites, but during calcination, further Pt ions might migrate into the pores of the zeolite. Because of all these differences, calcination in NaA produces new EPR active Pt species different than Pt⁺ and Pt³⁺. After oxygen calcination with 0.5 K min⁻¹ up to 633 K, the Pt atoms form a paramagnetic Pt

dimer (Fig. 4.15). Assuming one unpaired electron per dimer, we determine by the double integration method that a maximum of 18% of the total Pt atoms in the sample contribute to the EPR active dimer signal (Table 4.3). Because of this low abundance of the dimer, the Pt-Pt coordination cannot be distinguished from other coordinations with the EXAFS technique.

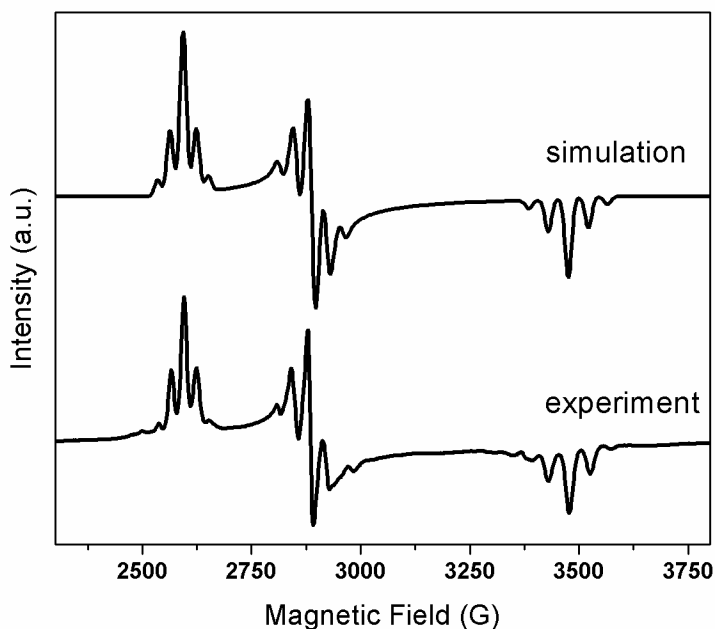


Figure 4.15: Simulated and experimental EPR spectrum of 1% Pt/NaA after O₂ calcination with a rate of 0.5 K min⁻¹ recorded at 20 K based on the Pt₂^{x+} parameters in Table 4.2.

The same product in different intensity was also formed upon different calcination conditions such as 1.25 K min⁻¹ heating rate and using between 548 K and 673 K. Fig. 4.15 shows the experimental orthorhombic EPR spectrum of 1% Pt/NaA measured at 20 K after calcination along with the corresponding simulated spectrum with $g_1 = 2.61$, $g_2 = 2.34$, $g_3 = 1.94$. The multiplets are due to hyperfine coupling. The Pt dimer is composed either of two, one or zero $I = \frac{1}{2}$ nuclei (¹⁹⁵Pt), the remaining nuclei being of spin zero, which is taken into account in the simulation. The g and A tensors are listed in Table 4.2.

The NaA zeolite has smaller pore window diameters compared to that of faujasites, so it is a good example to show sieving properties of zeolites. The $\text{Pt}(\text{NH}_3)_4^{2+}$ and $\text{Pd}(\text{NH}_3)_4^{2+}$ precursor complexes have bigger diameters than the NaA supercage window diameter so they cannot penetrate into the zeolite without decomposition of their amino groups. The thermal amino group decomposition rate of $\text{Pt}(\text{NH}_3)_4^{2+}$ and $\text{Pd}(\text{NH}_3)_4^{2+}$ complexes may be determined qualitatively by EPR. At 623 K, the $\text{Pt}(\text{NH}_3)_4^{2+}$ complex can enter the NaA zeolite and form dimers, but the $\text{Pd}(\text{NH}_3)_4^{2+}$ complex cannot form any paramagnetic species inside the zeolite at that temperature. However, some partially decomposed $\text{Pd}(\text{NH}_3)_n^{2+}$ samples, *e.g.* $n < 4$, can interact with the Pt dimer inside the zeolite. Fig. 4.16 displays these three different samples in NaA zeolite. The multiplet of the Pt dimer shows less anisotropy due to Pd interaction with a new signal at 3070 G.

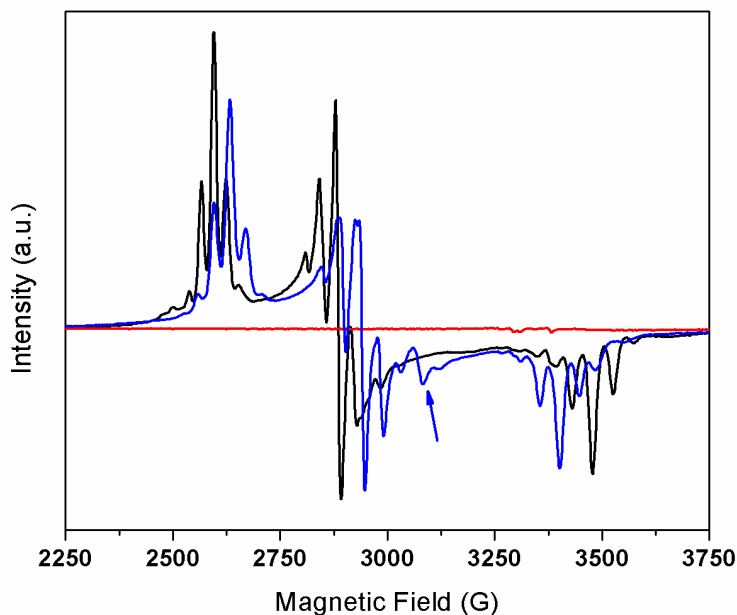


Figure 4.16: Experimental EPR spectrum of 1% Pt/NaA (black), PtPd/NaA (blue), and Pd/NaA (red) after O_2 calcination with a rate of 0.5 K min^{-1} up to 623 K recorded at 20 K. The arrow shows the signal at 3070 G.

At 673 K, the Pd cations form a paramagnetic Pd_x sample inside the zeolite. Fig. 4.17 displays the three different samples prepared at 673 K under oxygen flow. The paramagnetic Pd sample has a multiplet with hyperfine coupling originating from another Pd atom, because otherwise the isolated paramagnetic Pd atom is expected to give a sharp signal with an intensity distribution ratio of 1:1:1:21:1:1:1. The PtPd/NaA sample shows again less anisotropy than that of Pt_2 and additional new signals are observed compared to the Pt_2 .

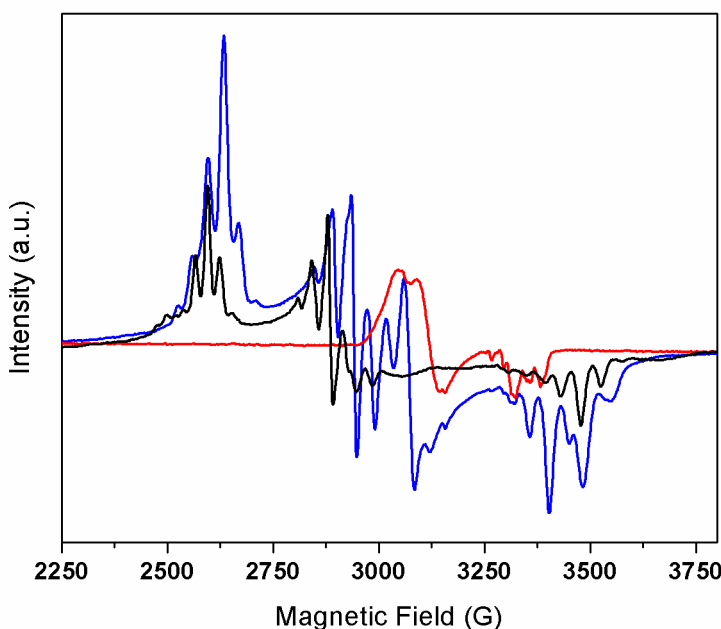


Figure 4.17: Experimental EPR spectrum of 1% Pt/NaA (black), PtPd/NaA (blue), and Pd/NaA (red) after O_2 calcination at 673 K.

In order to understand whether a Pt-Pd alloy forms or not, a method of addition-subtraction was applied (Fig. 4.18). At 623 K, the effect of Pd is observed over the Pt dimer anisotropy but a paramagnetic Pd sample is not detected. The addition of PtPd/NaA (623 K) to Pd/NaA (673 K) gives a similar pattern with PtPd/NaA (673 K) in Fig. 4.17. On the other hand, the addition of Pt/NaA (673 K) to Pd/NaA (673 K) is dissimilar with PtPd/NaA (673 K) results. These results show that a paramagnetic Pd_x

sample is formed in PtPd/NaA mixture next to Pt₂ that is influenced strongly by the existence of Pd. Therefore, a Pt-Pd alloy formation can be considered from the EPR results.

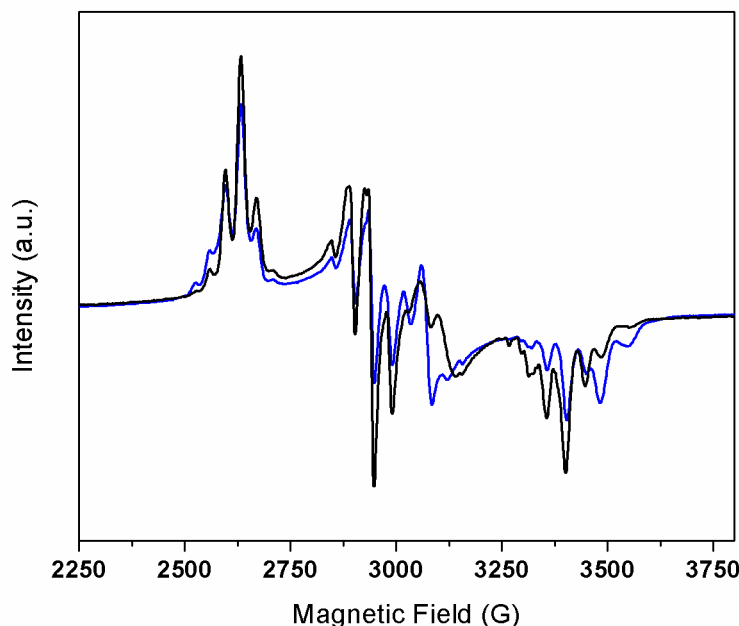


Figure 4.18: Comparison of PtPd/NaA (673 K), blue, with the sum of PtPd/NaA (623 K) and Pd/NaA (673 K), black.

4.2.8 General symmetry conditions

The faujasites and the zeolite NaA are of cubic symmetry. The ion sites in the faujasite supercages are denoted SII, which is located in a 6-ring window and has three-fold symmetry, and SIII which lies between two adjacent 4-ring windows (see Fig. 4.19). In addition to these there are further cation sites near S(II) and S(III). S(II)' is displaced further towards the sodalite cages, and S(II)* is slightly more shifted towards the centre of the supercages. S(III)* lies just above the base of the tetragonal pyramid defined by two O(1), two O(4) and one O(3). It should be noted that the crystallographic determinations represent average sites and do not take into account the local disorder due to partial substitution of Si by Al. According to the Si/Al ratio, the 6-ring of a zeolite may contain 0,

1, 2, or 3 and the 4-ring 0, 1, or 2 Al atoms. Statistically, 2 Al atoms per 6-ring is the most abundant population in NaY, whereas 3 Al atoms is the most abundant in NaX [82]. The positively charged Pt ions prefer a close proximity to the negatively charged Al atom, therefore the Pt–O(Al) distance is shorter than the Pt–O(Si) distance. Cu⁺ ions in NaY were studied by density functional calculations [83]. The coordination of the Cu⁺ with first shell framework oxygen in NaY was found to be 3 and 2, and the distance is approximately 2.03 Å for the sites II and III, respectively [83], while Cu²⁺ in NaY is fourfold coordinated [84]. Pt in high oxidation states needs a larger number of Al atoms in close proximity for charge compensation. This goes along with a higher coordination with oxygen than Cu⁺ has. Depending on the Al content and the oxidation state of Pt, the Pt-oxygen coordination in NaX is expected to be higher than in NaY. The EXAFS results show this to be the case in the second coordination shell, where the coordination numbers of Pt are 2.2 for NaX and 0.9 for NaY. Furthermore, the higher oxidation state (Pt³⁺ obtained at 0.5 K min⁻¹) has a higher total oxygen coordination number (6.9) than the lower oxidation state (Pt⁺ at 1.25 K min⁻¹). It should be noted that XAS gives the average values of all Pt ions, and most of them are in an EPR-silent, diamagnetic state, but it is nevertheless instructive to see that the abundance of Pt⁺ and Pt³⁺ correlates with a change in the average coordination of Pt. This is an example of the complementarity of EXAFS with EPR and FTIR for a complete characterization of the samples. Since also hydroxide ions may be involved, some ambiguity remains, and a unique assignment of the ion sites is not possible from the EXAFS data.

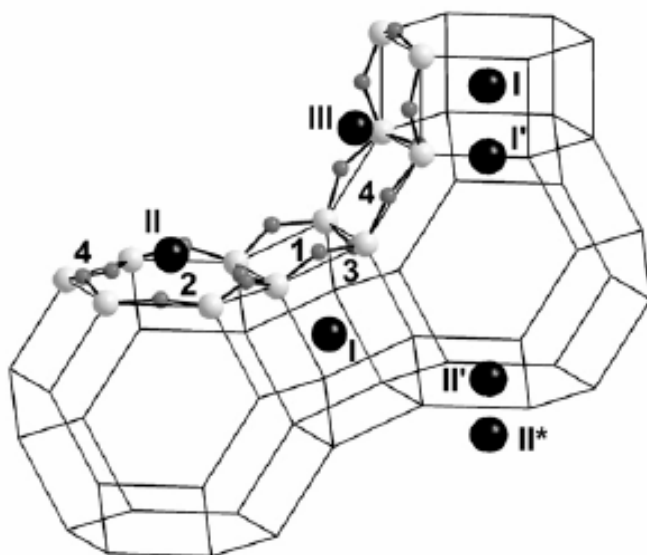


Figure 4.19: Structure fragment of faujasite Y zeolite, Al/Si atoms (light gray) sitting at the vertices connected by an oxygen atom (dark gray, with four different crystallographic frameworks) and the cation positions (black).

The free ions are of spherical symmetry, and any deviation that arises in the hyperfine and g tensors is thus due to the interaction of the ions with the lattice and reflects the local symmetry. At the SII site, when every second Si atom of the 6-ring window is substituted by Al (this is the maximum substitution that obeys the Löwenstein rule, and it is reached for the NaA and nearly for the NaX zeolites) the charge of Pt^{3+} is balanced by the 3 symmetrically placed Al atoms, and the local symmetry is axial within experimental error. However, the positive charge of Pt^{3+} may also be compensated with fewer Al atoms when OH^- groups formed during the decomposition of amino groups or Cl^- from the ion exchange reaction are present, but this breaks the axial symmetry. An orthorhombic environment is also available at the SIII site where only one Al atom is available in the immediate proximity to compensate the Pt charge. This site is thus consistent with an assignment of the orthorhombic g symmetry to Pt^+ . The same is true with Pt^+ at SII in cases where the 6-ring contains only two or a single Al atom, which is possible at low probability in NaX but is much more likely in NaY. Finding the exact position of Pt ions is not

possible with EPR and EXAFS. Since the symmetry depends on the Al content and the Pt oxidation state, the Pt positions are not predetermined and shift to the place of lowest potential energy.

The number and relative intensities of the hyperfine lines show that single Pt atoms and Pt dimers are involved and exclude the observation of clusters. A hyperfine structure was obtained for the Pt⁺ in NaX and NaY and for Pt₂ in NaA. However, only an unsplit line was observed for Pt³⁺. The reason of this may be either very small and unresolved hyperfine interactions, or alternatively large hyperfine anisotropies which make the lines of the spin-1/2 ¹⁹⁵Pt nucleus so broad that only the lines of the spin-0 isotopes are observed. Including a small hyperfine splitting was nevertheless found to increase the quality of fit. At higher measurement temperatures the hyperfine splittings of Pt⁺ also disappeared and the lines broadened beyond detection. The *d*⁹ and low spin *d*⁷ configurations correspond to one unpaired electron, which in ML₆ complexes leads to the so-called Jahn-Teller effect. A tetragonally distorted octahedron splits the 6 equivalent ligands into two sets of 4 and 2 ligands. The four oxygens in the first shell and two oxygens in the second shell around Pt that were detected by EXAFS (Table 4.1) could provide such an environment, although we were reminded that EXAFS does not provide the symmetry.

Ideally, if a static paramagnetic species has axial symmetry in EPR, the associated site geometry must contain an n-fold rotation axis with n>2, in all other cases the EPR parameters should be orthorhombic [85]. This also holds for the symmetry of Pt centres in zeolites with different Si/Al ratios. Pt ions at site SIII in faujasite (Fig. 4.19) are expected to have orthorhombic EPR symmetry, with $g_1 \neq g_2 \neq g_3$, whereas at SII there can be a threefold rotational axis if every second Si atom of the six-fold ring is replaced by Al, which should provide $g_1 \neq g_2 \sim g_3$. A lower Al content reduces the local symmetry. One should however keep in mind that *g*-components can show accidental degeneracy within experimental error.

4.2.9 EPR parameters

The g -Tensors of both Pt^+ species in NaX are clearly monoclinic, with $g_1 > g_2 > g_3$. This symmetry is compatible with the ion occupying site SIII. For this site the Löwenstein rule allows only one Al atom in the first coordination shell, which is compatible with the assigned single positive charge. $\text{Pt}^{3+}/\text{NaX}$ (1.25 K min^{-1}) is axial, which in symmetry and available Al atoms for charge compensation is compatible with the SII site. $g_{\parallel} < g_{\perp}$ is normally taken to relate to an elongated octahedron which has the unpaired d^7 electron in a d_{z^2} orbital [77]. At a lower calcination rate of 0.5 K min^{-1} the ions adopt monoclinic symmetry, compatible with SIII if additional anions are available for charge compensation. Pt^+/NaY provides two near-axial species, but in contrast to $\text{Pt}^{3+}/\text{NaX}$ we have now $g_{\parallel} > g_{\perp}$, as expected for an elongated octahedron with the unpaired d^9 electron in a $d_{x^2-y^2}$ orbital [77]. The values of the g components in Table 4.2 are all smaller than those reported for Pt^+ in an Ar matrix [86], and for Pt^{3+} in the $[\text{NBu}_4]^+[\text{Pt}^{3+}(\text{C}_6\text{Cl}_5)_4]^-$ complex ($g_{\parallel} = 3.29$, $g_{\perp} = 2.26$, and $g_{\parallel} = 1.62$, $g_{\perp} = 3.09$, respectively) [87], indicating not unexpectedly that the crystal field is stronger in the zeolite than in the Ar matrix [77]. The assignment of these sites seems compatible with the results of the EXAFS data, but EXAFS does not discriminate so well between the sites here. Similar g -values were reported for low spin d^7 $[\text{Pt}(\text{CN})_4\text{Cl}_2]^{3+}$ molecular complexes in alkali halides, with $g_{\parallel} = 1.988$ and $g_{\perp} = 2.253$ in NaCl, and with $g_{\parallel} = 1.991$ and $g_{\perp} = 2.704$ in KCl [88].

The g tensor of the Pt dimer cation is also rhombic, indicating that the axial symmetry which the free species would have is broken. This may mean that the dimer is located side-on coordinated at a cage wall. Other Pt dimers have been observed in single crystal silicon, also with rhombic symmetry. The g components appear to be quite sensitive to the preparation procedure, with their average value ranging between 1.78 and 2.17 [89]. The g_{av} value of 2.30 from the present work is higher than that in silicon but still below $g_{\text{av}} = 2.40$ as reported for the $[(\text{PtCl}_4)_2]^{3-}$ dimer in an irradiated K_2PtCl_4 single crystal [90]. Also here, the g anisotropy is significantly larger in silicon and in the tetrachloroplatinate crystal.

For individual paramagnetic ions and also for the Pt dimer the symmetry and orientation of the hyperfine tensor is expected to be the same as that of the g tensor. There are two contributions to it, the isotropic (Fermi-contact) term which is related to the s orbital spin density at the nucleus, and the anisotropic term which arises from the dipolar interaction of the unpaired electron in orbitals of p and for Pt in particular of d symmetry. Within some approximation (*e.g.* when spin polarization is neglected) it is useful to relate the observed parameters to limiting atomic values representing 100% spin population in a given orbital. They are often obtained only from calculations. For ^{195}Pt the tabulated value for A_{iso}° is +34410 MHz and $\alpha \times 1474$ MHz for A_{aniso}° , where α is an angular factor that depends on the orbital [47]. It should be noted that the sign is not obtained from EPR experiments, and this introduces some uncertainty in the analysis.

The isotropic hyperfine interaction $(A_1 + A_2 + A_3)/3$ is about 364 MHz for $^{195}\text{Pt}^+$ and 91 MHz for $^{195}\text{Pt}^{3+}$ in NaX. In comparison with the limiting atomic values we obtain the fractional $6s$ contributions of Pt^+ and Pt^{3+} as 1% and 0.2%, respectively, which is similar to the 1.4% found for Pt^+ in Ar [86] and 0.6% in NaY [15]. In contrast, Pt^{3+} in the $[\text{NBu}_4]^+[\text{Pt}^{3+}(\text{C}_6\text{Cl}_5)_4]^-$ complex has a very high A_{iso} value of 7320 MHz, which suggests a $6s$ spin density as high as 21%. The anisotropic hyperfine interaction $((A_1 + A_2)/2 - A_3)/3$ amounts to 21.6 MHz and 23.5 MHz for Pt^+ and Pt^{3+} , respectively, and the corrected A_{aniso} value is $2/7 \times 1474 = 421$ MHz for the $5d$ orbital [47]. Thus, assuming that all hyperfine components are positive the estimated $5d$ contribution is about 5%, which is similar to the value reported for Pt^+/NaY (2%) but lower than the contribution of d -orbitals of Pt^+ in Ar (54%). Such low $6s$ and $5d$ contributions raise the question where else the unpaired electron may possibly reside. It is difficult to imagine significant delocalization onto the zeolite lattice or inorganic ligands. A more plausible explanation may be obtained if one assumes that the A_3 component is of an opposite sign compared to A_1 and A_2 , which yields 56% $5d$ character of the unpaired electron in Pt^+/NaX but still only 17% for $\text{Pt}^{3+}/\text{NaX}$. The hyperfine parameters found for Pt^+/NaY have very small perpendicular components, while those of Pt^+/NaX are of comparable magnitude as those reported for the $[\text{Pt}(\text{CN})_4\text{Cl}_2]^{3+}$ molecular complexes in alkali halides [88].

A relationship was established between the values of the isotropic hyperfine constant and the spin density χ at the nucleus [87]. Considering $5d$ orbitals, a value of $\chi = -89$ a.u. is found for the high spin density of Pt^+ in the $[\text{NBu}_4]^+[\text{Pt}^{3+}(\text{C}_6\text{Cl}_5)_4]^-$ complex. Moreover, the unrestricted Hartree-Fock method gives the spin density at the nucleus of $5d$ free ions is between -17 and -18 a.u [91]. A positive χ value means that an occupancy of an $(n+1)$ s orbital lying outside the partially filled nd shell contributes an opposite term to χ and to the nd core polarization [90, 92]. The χ values of Pt/NaX are -0.0465 (Pt^+) and $+0.84$ (Pt^{3+}), so low spin density in d orbitals indicates that the ground state has $6s$ character which was also shown for Pt^{3+} in YAlG [81], BaTiO_3 [93] and for Pt^+ in $[\text{PtCl}_3]^{2-}$ single crystals [90].

For comparison, the hyperfine parameters reported for Pt^+ in an Ar matrix $A_{\parallel} \leq 46$ MHz, $A_{\perp} = 722$ MHz [86], and for Pt^{3+} in the $[\text{NBu}_4]^+[\text{Pt}^{3+}(\text{C}_6\text{Cl}_5)_4]^-$ complex $A_{\parallel} = 7795$ MHz, $A_{\perp} = 6375$ MHz [87], which corresponds to s and d spin populations of 1.4% and 53% for Pt^+/Ar 20% and 112% for the Pt^{3+} complex, respectively. The failure of the two spin populations to add up to 100% demonstrates impressively the approximate nature of this analysis that neglects the effects of spin polarization and is based on the orbital dimensions ($\langle r^{-3} \rangle$ values) of the undistorted and uncharged atom.

The charge of Pt_2^{x+} cannot be determined from the EPR experiment. Since the species is formed on oxidation, and because of the low Si/Al ratio of NaA which requires extensive compensation of lattice charges, it is conceivable that x equals 3 or even 5 (i.e 1.5 or 2.5 charges per atom). A Pt_2 species was also obtained as $[(\text{PtCl}_4)_2]^{3-}$ following irradiation of a K_2PtCl_4 single crystal [90]. Here, the charge of the Pt dimer is +5, which is compatible with our assumption about that of Pt_2/NaA . The s spin population amounts to 0.7% on each of the Pt atoms, and the d population to 2.3% if we assume the same charge for all hyperfine principal values, but 37.3% if the parallel component has the opposite sign, which looks much more reasonable.

5 Reconstruction of Pt₁₃ Clusters into Pt₂(CO)_m on CO Addition in NaY Zeolite

5.1 Reactivity of Pt₁₃ toward CO

Small Pt₁₃ clusters in NaY are very reactive with CO. They reconstruct into smaller platinum carbonyl aggregates at room temperature since the formed platinum carbonyl bonds compensate for the lost cohesive energy. In order to understand the CO adsorption effect on the structure of small Pt particles, a combination of EPR, XAS and FTIR techniques were used before and after the CO adsorption. In contrast to the existing studies on reduced Pt cluster-CO interaction, the structure of the paramagnetic Pt sample before CO adsorption is entirely known. Therefore, the relation between Pt particle size and CO fragmentation effect can be studied unambiguously. Final paramagnetic Pt carbonyl structures were easily characterized by EPR and results were compared with EXAFS Pt coordination data. Moreover, Pt-CO bonding was studied by EXAFS and FTIR spectroscopy.

5.2 Results

5.2.1 XANES and EXAFS study before and after CO adsorption

XANES spectra of the Pt metal foil, calcined Pt/NaY, reduced Pt/NaY, after subsequent Ar purging and CO adsorption on reduced Pt/NaY are given in Fig. 5.1. Both the shape and the intensity of the white line of the XANES are found to be completely different, although the absorption edge positions of the different Pt samples are similar to those of the reference metal foil. Compared to the metal foil, the calcined sample exhibits a relatively intense white line which is found to decrease in intensity upon reduction and further upon Ar purging, but it is still larger than for the metal foil. Upon CO adsorption, there is again a strong increase in the white line intensity.

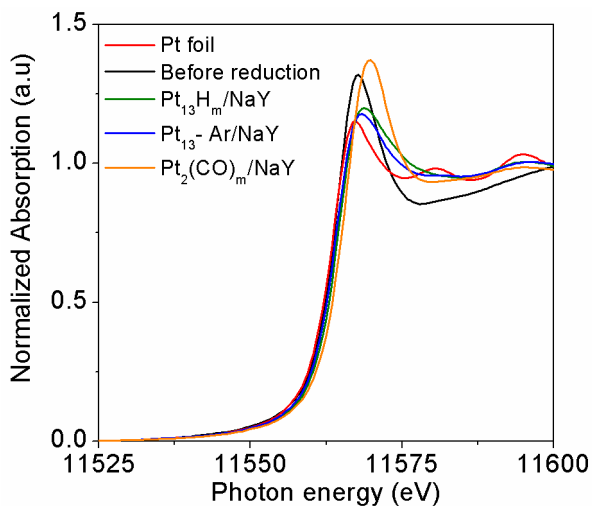


Figure 5.1: XANES spectra of Pt/NaY samples measured at the Pt L_{III} -edge (11564 eV) at different stages of *in-situ* treatment. (Measurements and analyses were performed by S. Anantharaman)

The experimental and fitted EXAFS functions in k -space and the corresponding Fourier transforms in real space of the platinum clusters after *in-situ* reduction are presented in Fig. 5.2. The local structure around Pt in $\text{Pt}_{13}\text{H}_m/\text{NaY}$ obtained from the fit, the parameters used in the fitting procedure, the resulting fit parameters and the estimated errors in their determination are given in Table 5.1. In the experimental phase corrected Fourier transformed EXAFS function, one intense peak at around 2.7 Å is observed along with a smaller side lobe at roughly 1.8 Å. It was verified by fitting that this is not a structure feature from lighter back scattering elements which might be present at this distance but due to the non-linear nature of the backscattering amplitude relevant in heavy elements. This feature is also reproduced when the theoretical EXAFS function was calculated using only Pt and oxygen shells at higher distances. In the EXAFS spectrum, only a single intense peak at roughly 2.7 Å is present and further peaks with comparable intensities, which are normally present in larger platinum clusters or bulk platinum metal, are absent. Due to this fact, the addition of higher shells of Pt in the fitting did not give significant improvement of the fit. The peak near 2.7 Å could be fitted with Pt at 2.77 Å as well as O at 2.72 Å with average coordination numbers of 5.8 and 3.8, respectively. Considerable improvement in the quality of the fit justified the inclusion of this oxygen shell in the model along with the platinum shell. The first shell Pt–Pt average coordination number of 5.8 provides evidence that very small, probably 13-atom clusters are formed in NaY. However, despite the small cluster size of ca. 0.8 nm, the observed Pt–Pt distance is comparable with its bulk value, ~ 2.77 Å, due to a relaxation effect by the adsorbed hydrogen atoms. The presence of the longer Pt–O distance compared to that observed in PtO_2 , ~ 2.0 Å [76], and the absence of an oxygen shell at this distance exclude the possible oxidation of the platinum clusters and reiterate the necessity to use *in situ* reduction to characterize such samples.

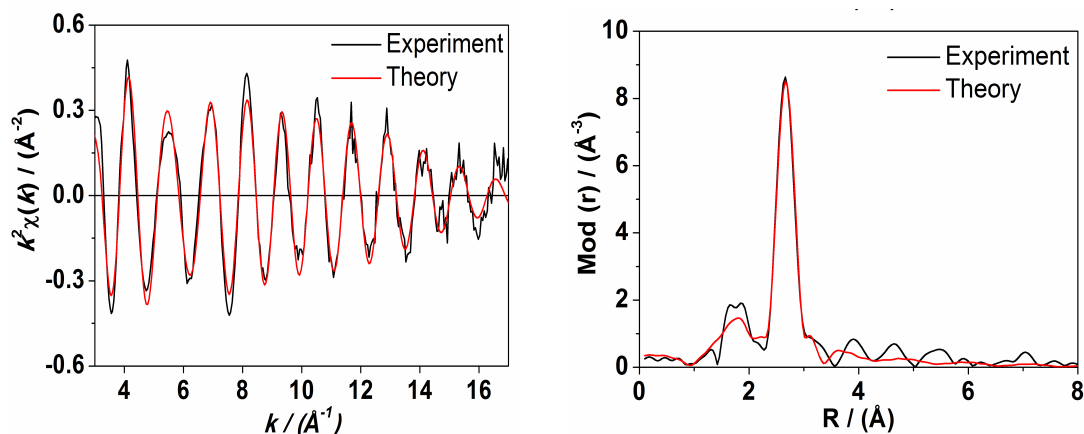


Figure 5.2: Experimental EXAFS function (left), its Fourier transform (right) and theoretical fit (red) to the experimental data of $\text{Pt}_{13}\text{H}_m/\text{NaY}$. (Measurements and analyses were performed by S. Anantharaman)

The k^2 weighted experimental EXAFS function $k^2\chi(k)$, and its Fourier transform for $\text{Pt}_2(\text{CO})_m/\text{NaY}$ (Fig. 5.3), and their comparison with $\text{Pt}_{13}\text{H}_m/\text{NaY}$ are shown in Fig. 5.4. Significant changes in the spectrum upon CO exposure at room temperature can be observed. Change in the backscattering amplitude, which is the envelope in the EXAFS function, is observed at both low and high k values. After CO adsorption, oscillations in the range $7 - 14 \text{ \AA}^{-1}$, relevant for heavy elements are subdued, whereas strong oscillations appear in the range $3 - 7 \text{ \AA}^{-1}$. A considerable decrease in the intensity of the Fourier transform peak at roughly 2.7 \AA and appearance of peaks near 2.0 \AA are noticed after CO adsorption.

Table 5.1: Fit results of all EXAFS data. (Analyses were performed by S. Anantharaman)

Sample	Abs-Bs ^a	CN(Bs) ^b	R(Bs) ^c [Å]	σ^d [Å]	E_F^e [eV]	k -range [Å ⁻¹]	R-factor
Pt ₁₃ H _m	Pt-Pt	5.8 ± 0.6	2.77 ± 0.03	0.084 ± 0.01	-10.02	2.92 - 17.03	24.48
	Pt-O	3.8 ± 0.4	2.72 ± 0.03	0.050 ± 0.01			
Pt ₂ (CO) _m	Pt-C	0.8 ± 0.1	1.95 ± 0.02	0.055 ± 0.01	-13.44	2.90 - 17.01	34.73
	Pt-C	1.7 ± 0.2	2.14 ± 0.02	0.092 ± 0.09			
	Pt-Pt	0.9 ± 0.1	2.69 ± 0.03	0.059 ± 0.01			
	Pt-O	4.6 ± 0.7	2.72 ± 0.03	0.081 ± 0.01			

^a absorber (Abs) – backscatterers (Bs), ^b coordination number CN , ^c interatomic distance, ^d Debye-Waller factor σ with its calculated deviation, ^e Fermi energy E_F

In order to quantify the observed changes, experimental spectra were fitted with relevant structure models consisting of Pt–C, Pt–O and Pt–Pt contributions. Based upon the goodness of fit, the most probable structure and eventually the local structure parameters like average coordination number, average interatomic distances, Debye-Waller-like factors for the different shells were obtained. For the CO adsorbed platinum cluster, the model consists of one Pt–Pt shell, two Pt–C shells, and one Pt–O shell (zeolite oxygen) contributions. The use of further oxygen shells from CO at more than 3 Å was statistically not justified due to the increase in the number of iteration parameters. The Pt–Pt distance in Pt₂(CO)_m/NaY has contracted to 2.69 Å from 2.77 Å in Pt₁₃H_m/NaY, together with a decrease in the Pt–Pt average coordination number from 5.8 to 0.9. Two Pt–C contributions, one at 1.95 Å and the next at 2.14 Å are obtained with average coordination numbers of 0.8 and 1.7, respectively.

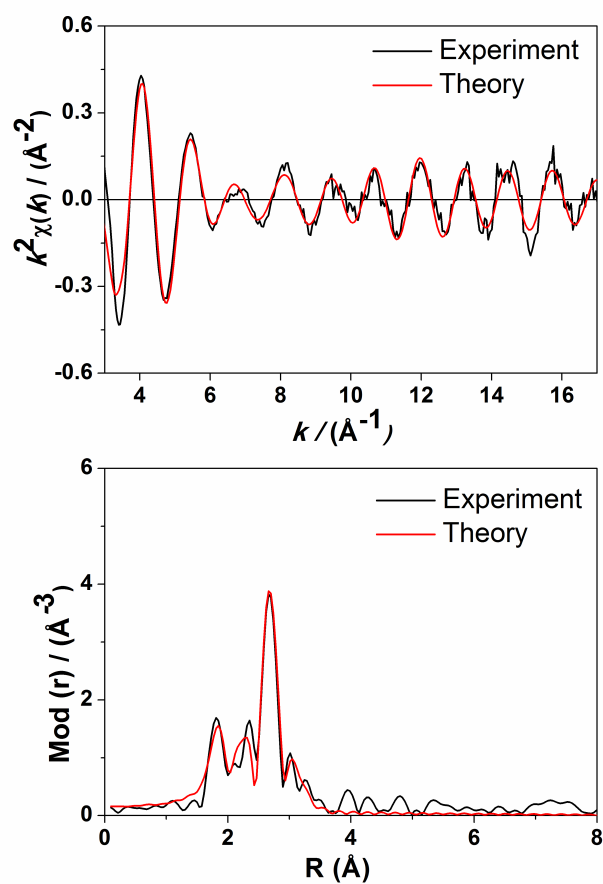


Figure 5.3: Experimental EXAFS function (top), its Fourier transform (bottom) and fit (red) to the experimental data of $\text{Pt}_2(\text{CO})_m/\text{NaY}$. (Measurements and analyses were performed by S. Anantharaman)

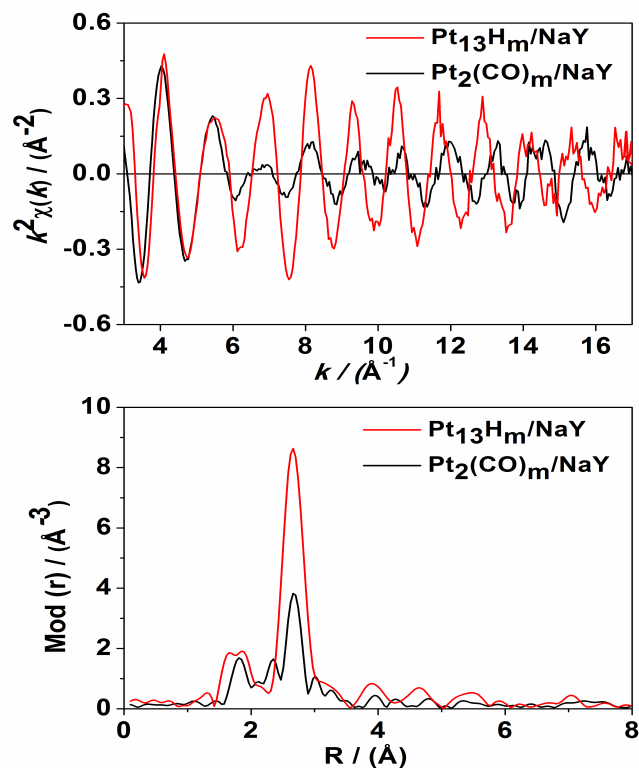


Figure 5.4 Experimental EXAFS function (top) and its Fourier transform (bottom) of $\text{Pt}_{13}\text{H}_m/\text{NaY}$ and $\text{Pt}_2(\text{CO})_m/\text{NaY}$. (Measurements and analyses were performed by S. Anantharaman)

5.2.2 X-band EPR measurements

Fig. 5.5 (a) shows an X-band EPR spectrum of reduced Pt in NaY that was measured at 20 K. The deuterium exchanged sample was used for EPR characterization because it gives a stronger and more symmetrical spectrum while the main feature of the spectra remains the same. The observed highly symmetrical multiplet has a g_{iso} value of 2.35 with a splitting which derives from 12 equivalent Pt nuclei.

Adsorption of CO at room temperature on the reduced Pt cluster leads to a complete change of the EPR spectrum. The spectrum of the Pt cluster at $g_{\text{iso}} = 2.35$ disappears and

a new spectrum appears at $g_{\text{iso}} = 1.98$. The signal intensity of the newly formed carbonyl sample increases without any structural variations in the spectrum till 125 mbar CO, but on further CO addition it has an almost constant intensity (Fig. 5.5 (b-e)).

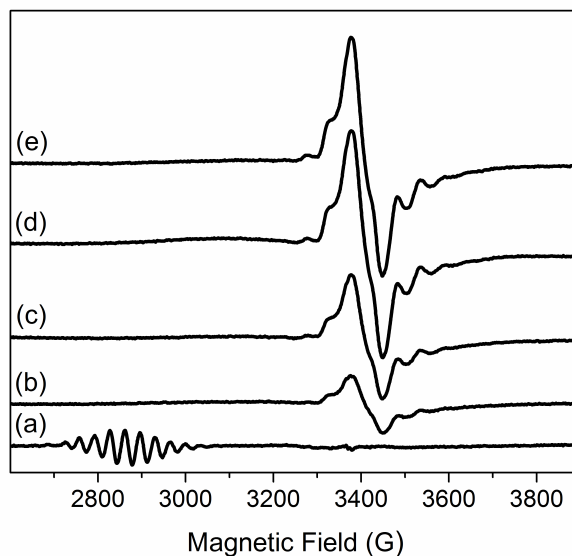


Figure 5.5: X- band EPR of Pt_{13}D_m recorded at 20 K before (a) and after adsorption of different doses of CO and evacuation at room temperature; 50 mbar (b), 100 mbar (c), 125 mbar (d), 500 mbar (e).

The double integral of the EPR spectra is proportional to the number of unpaired electrons, and after CO adsorption the resultant species has about 15 times more signal intensity than that of the reduced Pt cluster. Exposure of CO on the pure NaY (treated under the same condition of calcination and reduction) and on the $\text{Pt}^{2+}/\text{NaY}$ did not give any EPR signal. The EPR spectrum of the isotopically enriched sample of the ^{194}Pt cluster/NaY facilitates the assignment of the platinum carbonyl structure. Fig. 5.6 compares the spectra of the Pt cluster upon CO exposure composed of natural abundance Pt (33.3% ^{195}Pt , 66.6% ^{194}Pt) and enriched ^{194}Pt (97.5%). In contrast to the enriched ^{194}Pt sample ($I = 0$) (Fig. 5.6a), two small satellites on both sides of the main peak originate from hyperfine splitting of ^{195}Pt nuclei ($I = 1/2$) which contains Pt in natural abundance

(Fig. 5.6b). The enrichment is incomplete, so this small amount of Pt with $I = \frac{1}{2}$ causes the remaining weak hyperfine features seen in Fig. 5.6a.

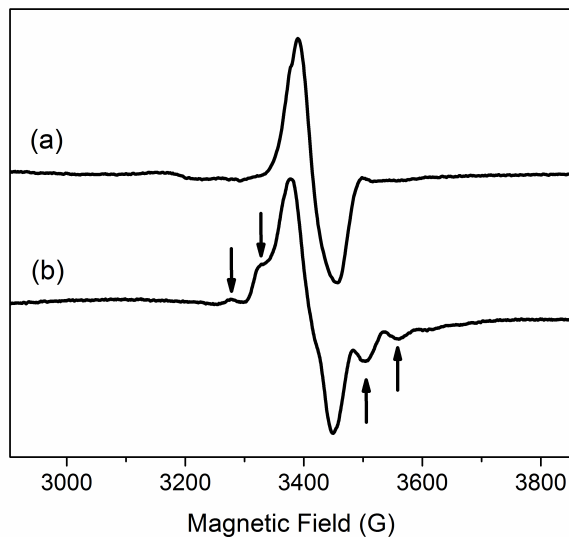


Figure 5.6: EPR spectra of $^{194}\text{Pt}_2(\text{CO})_m$ (a) and natural abundance $\text{Pt}_2(\text{CO})_m$ (b) recorded at 20 K after saturation adsorption of CO at room temperature.

5.2.3 C-O stretching via FTIR

The FTIR spectra obtained after CO adsorption at room temperature under saturation conditions ($P_{\text{CO}} = 500$ mbar) on the reduced sample and then upon subsequent evacuation at the same temperature for different time durations are displayed in Fig. 5.7. In order to avoid an exposure to air, and more importantly, to obtain measurement conditions similar to those used in the EPR measurements, the reduced Pt/NaY sample was subjected to additional treatments in the FTIR sample cell. The air effect can be thought of as a combination of oxygen and water vapor, which were studied previously by EPR [94]. The EPR signal of the Pt_{13} cluster disappears upon interaction with oxygen or water vapor after long time air exposure. On the other hand, after evacuation of the sample tube at 573 K for two hours and upon reduction with static hydrogen pressure at 473 K, the Pt multiplet signal reappears.

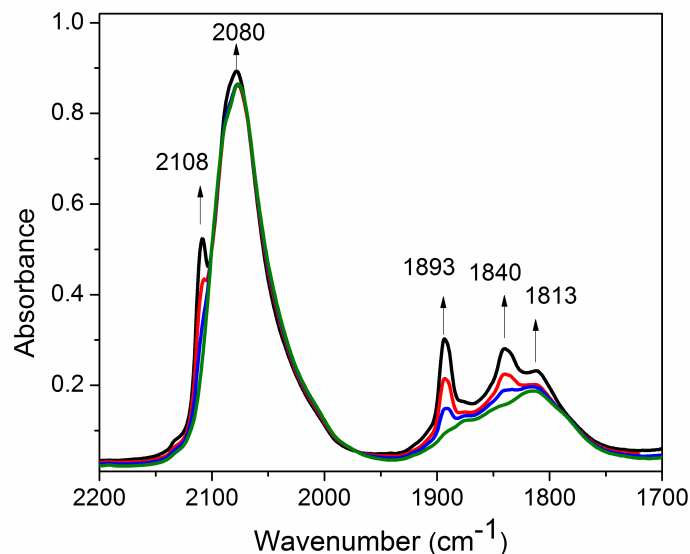


Figure 5.7: FTIR spectra recorded after CO adsorption (500 mbar) at 298 K on $\text{Pt}_{13}\text{H}_m/\text{NaY}$ followed by evacuation at the same temperature for 3 min (black), 25 min (red), 45 min (blue), 90 min (green).

In the FTIR spectra, it is clear that the absorption around 2000 cm^{-1} are due to linearly coordinated CO and bands around 1850 cm^{-1} are caused by bridged CO coordinated to neighboring Pt atoms. The FTIR spectrum displays a peak at 2080 cm^{-1} with a shoulder at 2108 cm^{-1} which are assigned to bands of linear Pt–CO (Fig. 5.7). In the absorption region around the bridged Pt–CO band, two clearly distinguishable peaks at 1893 and 1840 cm^{-1} with a shoulder at 1813 cm^{-1} are observed. Fig. 5.7 shows the behavior of the absorption bands with different evacuation times at room temperature. CO evacuation leads to a decrease in the intensity of the peak at 2108 , 1893 , and 1840 cm^{-1} , without shifting them to lower wavenumbers, and after 90 min these bands vanish. However, the strong band at 2080 cm^{-1} and the shoulder at 1812 cm^{-1} are not affected significantly. Two bridge bands at 1893 and 1840 cm^{-1} exhibit similar behavior upon evacuation.

Fig. 5.8 depicts variations of the FTIR spectra during the temperature programmed desorption. The bands at 2108, 1893 and 1840 cm^{-1} disappear at 373 K, but the main signal at 2080 cm^{-1} and the shoulder at 1812 cm^{-1} remain almost unchanged. At 473 K, the main signal at 2080 cm^{-1} shifts to 2070 cm^{-1} under formation of a new shoulder at 2000 cm^{-1} , and the shoulder at 1812 cm^{-1} shifts to 1795 cm^{-1} . At an even higher temperature of 523 K, the main band shifts to 2061 cm^{-1} with a noticeable lower intensity and an obvious shoulder at 2001 cm^{-1} , along with the complete disappearance of the bridge bands.

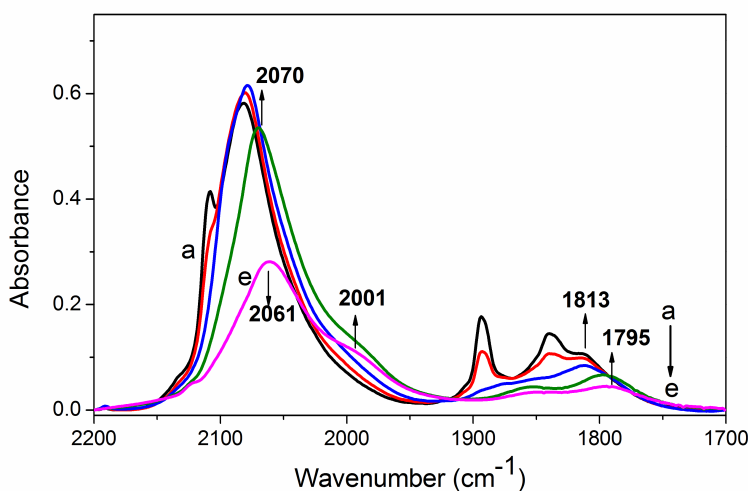


Figure 5.8: FTIR spectra recorded after CO adsorption (500 mbar) at 298 K on $\text{Pt}_{13}\text{H}_m/\text{NaY}$ followed by evacuation at 298 K (a), 348 K (b), 373 K (c), 473 K (d), 523 K (e).

Fig. 5.9 shows the FTIR spectra obtained after repeated room temperature 500 mbar CO adsorption – desorption cycles with the emphasis on the bands that occur at 2108, 2000, and 1813 cm^{-1} . Following three adsorption-desorption cycles the shoulder at 2108 cm^{-1} nearly disappears, but the one at 2000 cm^{-1} becomes more pronounced. In contrast to the behavior of other bands, the shoulder at 1813 cm^{-1} behaves like a new band and shows

increase in intensity after each cycle. As a result, the initial CO adsorbed-desorbed sample and the sample after three adsorption-desorption cycles, exhibit spectra that are different from each other.

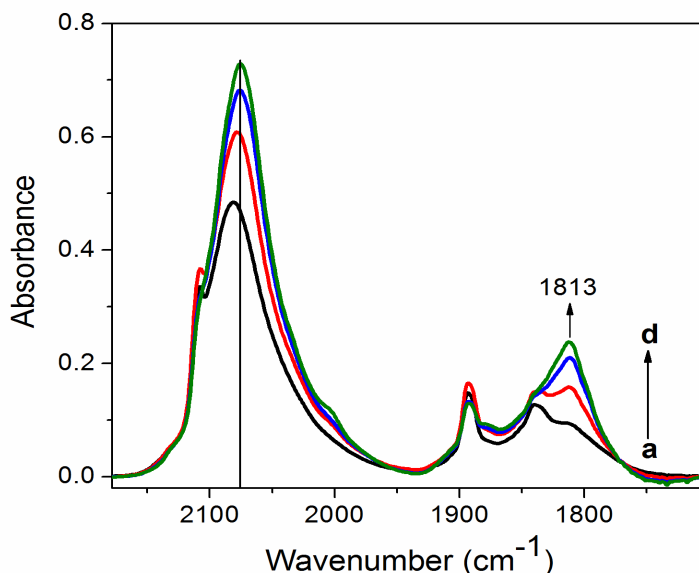


Figure 5. 9: FTIR spectra of CO adsorbed on Pt₁₃H_m/NaY at 500 mbar: (a) initial sample, and after (b) one- (c) two- (d) three-fold CO adsorption-desorption cycles.

5.3 Discussion

5.3.1 Electronic and coordination structure

The XANES shows the difference in the shape and height of the white line in the case of the sample prepared by oxygen calcination prior to *in situ* reduction, after hydrogen reduction and after subsequent argon purging and CO adsorption. The L_{III} -edge in platinum corresponds to the electronic transition from the $2p_{3/2}$ to the $5d$ level [95, 96]. Platinum has the electronic configuration $5d^96s^1$ in its ground state, and the unoccupied d level in the Pt atom is the $d_{5/2}$ state. Depending upon the d band vacancies in the final

state, the intensity of the white line varies. After calcination, the Pt has a higher oxidation state with more vacancies, which causes the intense white line. Increase in the white line intensity for hydrogen reduced small Pt clusters compared to the platinum metal foil has previously been attributed to changes in the d band vacancies [97]. However, in this case, both the effect of the cluster size and the effect of hydrogen adsorption, play a role. In order to decouple these two effects, one has to measure the XANES for bare clusters and hydrogen adsorbed clusters. In this respect, upon Ar purging (Fig. 5.1), reduction in the intensity and width of the white line is observed. This tendency can be attributed to the partial desorption of adsorbed hydrogen, though complete desorption of hydrogen could not be verified. It should be noted that the Pt–H bonds are strongly polar, with the negative end on the hydridic hydrogen, which partly depletes the d -state. Upon CO adsorption, the increase in the white line could be attributed to the increase in ionicity of the platinum center due to bond formation with CO. Thus, the platinum atoms have a lower electron density by π -backdonation from Pt to CO or a positive partial charge on Pt, or a combination of both [26]. Qualitatively, on moving from the metal foil to small clusters in the zeolite with adsorbed H₂ or CO, the changes in the white line are attributed to an increase in d -band vacancies.

EXAFS measurements and analysis of reduced Pt samples in NaY zeolite prepared *ex situ* using similar conditions has already been reported in an earlier work [7]. In this work, the Pt cluster preparation has been carried out under *in situ* conditions under a high flux of the reactant gases so that air oxidation of the clusters can be safely ruled out. Additionally, the effect of subsequent CO adsorption on the structure of platinum clusters has been investigated. Insights into the size of the clusters, their location in the zeolite matrix and the effect of CO adsorption were obtained from the analysis of the local structure around Pt. The average Pt–Pt shell coordination number of 5.8 obtained from the analysis is compatible with the presence of 13-atom clusters, also evidenced by EPR, which is discussed in the following section. The clusters of this size (ca. 0.8 nm) could very well fit into the supercages of the NaY zeolite with a free diameter of 1.3 nm. In addition, a second near neighbor shell contribution from the zeolite oxygen atoms is

present at 2.72 Å. Similar Pt–O distances have already been reported earlier for Pt in Y zeolites [98]. The relatively long Pt–O distance is attributed to the presence of interfacial hydrogen after reduction [24].

Analysis of Pt₁₃H_m after CO adsorption revealed a contraction of the Pt–Pt distance from 2.77 to 2.69 Å, accompanied by a decrease in the Pt–Pt coordination number from 5.8 to 0.9. This average Pt–Pt distance is very similar to that measured for [Pt₂Br₂(μ-CO)(PPh₃)] compounds with 2.65 Å [99]. The changes in the structure parameters indicate a reconstruction of the Pt₁₃ cluster into smaller aggregates, most likely Pt₂. Furthermore, the two different Pt–C contributions, one at 1.95 Å and the other at 2.14 Å with coordination numbers of 0.8 and 1.7, respectively, are obtained. The short Pt–C distances are similar to Pt–C distances observed in compounds like Pt₃(CO)₆ where CO molecules are linearly and bridge coordinated to Pt [100]. So, it can be said with some degree of certainty that in the present case, one linear and two bridged CO molecules coordinate the Pt atoms. The presence of two different Pt–C contributions is attributed to the Pt–CO linear and bridge bonded species as confirmed by the FTIR results.

A further EXAFS contribution is present at 2.72 Å due to zeolite oxygen with an increase in coordination number of Pt–O from 3.8 to 4.6, indicating that the Pt carbonyl clusters are in proximity to the zeolite framework. This observation is attributed to the stabilizing effect of the zeolite oxygen atoms on the resulting structure. In this case, neutral platinum carbonyl samples having only CO ligands are very unstable due to weak Pt–CO bonds, and so far only Pt(CO)₄ has been prepared in argon matrices below 10 K [101, 102]. However, oxygen atoms in KL zeolite acted as σ-donor ligands to stabilize the small platinum carbonyl clusters [25]. The basicity strength of the oxygen atom in NaY is similar to that in KL zeolite [103], so it is reasonable to obtain small stable platinum carbonyl species closer to the framework oxygen. Furthermore, we have limited information about the residual charge on the carbonyl cluster (see FTIR part).

5.3.2 X-band EPR characterization

Pt clusters were studied extensively as hydrogen adsorbed Pt_{13}H_m , deuterium exchanged Pt_{13}D_m , and as bare clusters Pt_{13} by X-band EPR in a previous study [8]. The well defined paramagnetic cluster containing 12 equivalent surface and a single core atom has a multiplet spectrum at $g_{\text{iso}} = 2.35$ with a splitting due to 12 equivalent Pt nuclei. Pt at the core of the cluster does not carry significant unpaired electron density since for symmetry reasons the relevant cluster molecular orbitals have a nodal plane through the center. The highly symmetrical EPR spectra suggest an icosahedral structure in the supercages of the NaY zeolite, although open shell structures are expected to undergo a Jahn-Teller distortion. CO adsorption dissipates the signal of the Pt_{13} cluster, and this was not reversible even on desorption of CO and subsequent hydrogen reduction. It indicates that the Pt_{13} clusters are completely destroyed after CO reaction (Fig. 5.5). The shape of the newly formed Pt–CO spectrum is retained on increasing intensity upon additional CO exposure, which means that only one type of paramagnetic Pt carbonyl species is formed. Moreover, only one pattern of g parameters reveals that the location of this complex within the zeolite seems to be the same.

The 15-fold higher yield calculated from the double integral of the platinum carbonyl spectrum compared with that of reduced Pt_{13} clusters shows that the number of unpaired electrons is increasing 15 times in the $\text{Pt}_2(\text{CO})_m/\text{NaY}$ sample. However, the amount of EPR active Pt is only 0.5%, which means that most of the Pt is still EPR silent. The rest can be diamagnetic platinum carbonyl or found in high spin states, which are not accessible to X-band EPR but can be studied by SQUID measurements.

The new spectrum at $g_{\text{iso}} = 1.982$ is composed of two satellites on both sides of the main signal, but the enriched ^{194}Pt –CO sample shows only the main signal. The predicted hyperfine multiplet arising from two Pt nuclei with spin- $1/2$ with 1:8:18:8:1 relative intensities is very compatible with the experimental Pt–CO EPR spectrum. The EPR spectrum of the saturated carbonyl species (Fig. 5.5(e)) and the corresponding simulation are displayed in Fig. 5.10.

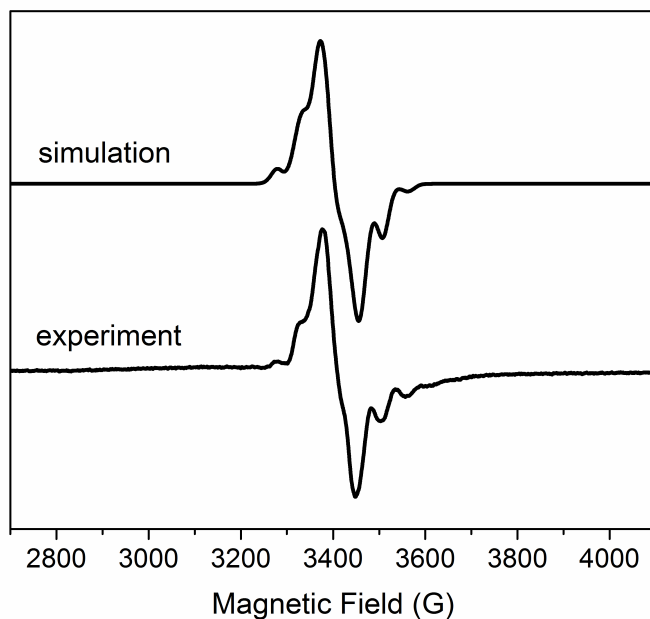


Figure 5.10: EPR spectra of $\text{Pt}_2(\text{CO})_m/\text{NaY}$ sample recorded at 20 K and corresponding simulation.

The assigned structure is a Pt dimer which is composed either of two, one or zero $I = \frac{1}{2}$ nuclei (^{195}Pt), the remaining nuclei being of spin zero, with natural abundance of isotopes. The g and A tensors are listed in Table 5.2. The g tensor of the Pt dimer is rhombic with a small anisotropy, $g_1 = 1.957$, $g_2 = 1.985$, and $g_3 = 2.005$, indicating that the axial symmetry is broken by side-on coordination at a cage wall or by the coordinated CO molecules. Pt dimers have been observed elsewhere in NaA zeolite, and others in single crystal silicon with an average g value of 2.30 and components ranging between 1.78 and 2.17, respectively [23, 56, 89, 104]. Furthermore, an identical EPR spectrum is obtained when ^{13}C (carbon: $I = \frac{1}{2}$, 99%) is used instead of natural abundance carbon ($I = \frac{1}{2}$, 1.1%; $I = 0$, 98.9%) without additional hyperfine lines or line broadening due to ^{13}C interaction. It indicates that the unpaired spin density is mainly located on Pt atoms and it is almost zero at the ^{13}C nucleus. The isotropic hyperfine interaction $(A_1 + A_2 + A_3)/3$ is

about 250 MHz, and for ^{195}Pt atoms the tabulated value for A_{iso} is +34410 MHz, so the fractional $6s$ contribution is 0.7% per Pt atom. The experimental anisotropic hyperfine interaction $(A_1 - (A_2 + A_3)/2)/3$ amounts to 21 MHz and the corrected tabulated A_{aniso} value is $2/7 \times 1474 = 421$ MHz for the $5d$ orbital [47]. If all hyperfine components are positive the estimated $5d$ contribution is about 5% per Pt atom. Such low $5d$ contributions can be explained if one or two of the hyperfine components are of opposite signs, for example, this yields 23% or 41% $5d$ character per Pt atom by assuming that A_3 is negative or A_2 and A_3 are both negative, respectively.

Table 5.2: EPR parameters from spectral simulation obtained with Pt samples

Samples	g					$A(^{195}\text{Pt})/\text{MHz}$				
	g_1	g_2	g_3	g_{\perp}	g_{\parallel}	A_1	A_2	A_3	A_{\perp}	A_{\parallel}
Pt_{13}D_m				2.356	2.359				234	211
$\text{Pt}_2(\text{CO})_m$	1.957	1.985	2.005			290	222	235		
$^{194}\text{Pt}_2(\text{CO})_m$	1.954	1.987	1.989							

5.3.3 Pt-CO bonding

FTIR spectroscopy has been used to characterize the reactivity of small supported Pt clusters with CO by observing the C–O stretching frequency, which depends on the Pt atom to which CO is bound. The C–O vibration is very sensitive to the number of Pt atoms linked to CO ligands [55], the coordination and oxidation state of the Pt atom to which CO is adsorbed [23, 62], the CO coverage [105], and the acid-base properties of the support [106]. Moreover, the intensity ratio of the bands of linear and bridge-bonded CO is influenced by the electron charge on the supported Pt cluster [106]. The FTIR experiments that were carried out by considering these factors show that the dimer

platinum carbonyl sample has one type of linear bonded and two different bridge bonded CO molecules.

Since the structures of bare and hydrogen covered Pt₁₃ clusters are the same and the adsorbed hydrogen atoms are easily exchanged with CO molecules, the IR spectra after CO adsorption are similar over both platinum samples. The absorption band at 2080 cm⁻¹ with a small bandwidth (half bandwidth of 44 cm⁻¹) at room temperature can be assigned to linearly bound Pt⁰-CO species; however, the shoulder at 2108 cm⁻¹ is different from the main band and behaves independently. Carbonyl bands at frequencies > 2100 cm⁻¹ have usually been assigned to Pt^{δ+}-CO species [13, 23]. The EPR-active fraction of the precursor Pt₁₃H_m cluster probably has an odd positive charge (+1 or +3) [8], and this may be retained upon admission of CO under fragmentation to Pt-CO aggregates to preserve the charge balance in zeolite. The major fraction is EPR inactive and probably a high-spin state of unknown charge, but EXAFS shows that these clusters are of the same size. Since CO is a reducing agent, the charge of Pt in the newly formed platinum carbonyl species must be close to zero or adopt at best a small positive value. Therefore, the absorption at 2108 cm⁻¹ can be assigned to Pt₂^{δ+}-CO, with slightly electron deficient Pt atoms. In concentrated sulfuric acid, the homoleptic, dinuclear, cationic platinum(I) carbonyl complex, was synthesized from PtO₂ by exchange with CO [107]. This shows that it is possible to stabilize also cationic platinum carbonyls in suitable media. By evacuation at room temperature or at high temperatures the corresponding band easily disappears, which shows that the Pt^{δ+}-CO bond is weak due to low Pt → π* back donation. After two adsorption-desorption cycles, this band almost did not reappear after the addition of the next 500 mbar CO aliquot (Fig. 5.9). This implies that either Pt^{δ+} reduces to Pt⁰ or that new Pt carbonyl species are present. The presence of both of these is likely because the Pt₂⁰-CO band intensity increases and new signals at 2001 and 1813 cm⁻¹ become more prominent.

According to EXAFS and in agreement with EPR the new unit formed on fragmentation is binuclear and contains a Pt-Pt bond. The question is how many CO ligands it contains.

The bands due to bridged CO at 1893 and 1840 cm^{-1} change in concert, which shows that they relate to the ν_s and ν_{as} modes of two coupled CO ligands of the same species. These bands are very similar to bridge bands belonging to subcarbonyl species of Chini complexes, *e.g.* $[\text{Pt}_3(\text{CO})_3(\mu_2\text{-CO})_3]$, or triangular cluster framework species at 1896 and 1841 cm^{-1} after reductive carbonylation of $\text{Pt}^{2+}/\text{NaY}$ upon the exposure to CO at room temperature [14]. This implies that a symmetric bridge bonded structure is formed. Additionally, one more type of bridged CO group is observed at 1813 cm^{-1} , especially after adsorption-desorption cycles. Partial desorption of CO leads to a change in the position of the platinum carbonyls and allows the cluster to be closer to the zeolite framework, which causes limitation of free space for CO bridge bonding. Fig. 5.9 shows a huge increase in intensity of the band at 1813 cm^{-1} , which is now more favorable, compared to that of other types of bridged CO bands. There are one linear and two bridge bonded CO ligands (sym, asym) per Pt atom at the initial coverage, in agreement with the EXAFS results which gives one carbon at a distance of 1.95 Å and two at 2.14 Å. After the desorption-adsorption cycles another bridged CO ligand (1813 cm^{-1}) is more pronounced. We therefore suggest that the dinuclear Pt carbonyl complex has the structure given in Fig. 5.11.

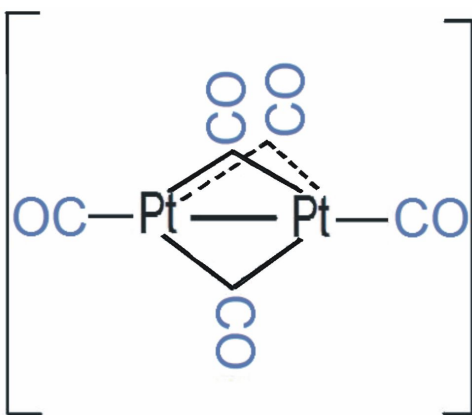


Figure 5.11: Schematic structure of $\text{Pt}_2(\text{CO})_m$ along with the possible types of CO bonding.

The cohesive energy per atom scales approximately with the average coordination number [52]. With 347 kJ mol^{-1} as calculated for 13-atom metal clusters ($CN = 5.8 \pm 0.6$, see Table 5.1) [8] it is considerably smaller than the 528 kJ mol^{-1} for the bulk metal ($CN = 12$) [108]. For Pt_{10} clusters the calculated average cohesive energy per Pt atom is 255 kJ mol^{-1} , and the heat of formation of neutral Pt-CO clusters by reaction of Pt_{10} with 10 CO molecules was calculated to be only $-30 \text{ kJ per mol CO}$, which is nearly thermoneutral [108]. Therefore, on CO addition small particles are highly reactive towards fragmentation, since the metal carbonyl bonds compensate for the lost cohesive energy. For example, when an $\text{Rh}/\text{Al}_2\text{O}_3$ catalyst was studied before and after CO adsorption it was found that CO adsorption disrupts the Rh–Rh bonds and decreases the Rh–Rh coordination number from 3.7 to 1.8 [109]. On the other hand, rhodium particles with an average $CN \sim 7$ did not reconstruct under CO atmosphere [110]. Here, EXAFS and FTIR studies have shown that the Pt metal particle size effect is similar to that of Rh with CO [24, 26]. However, the FTIR spectra of a CO exposed Pd cluster in NaY was assigned to $\text{Pd}_{13}(\text{CO})_x$ clusters. It was proposed that the Pd_{13} cluster is obtained in the supercages and that it is stable on CO adsorption, although the particle size is not very large [111]. The interpretation of such experimental data is often ambiguous because the EXAFS technique gives average fit values, and a frequency shift of CO is usually the result of more than one effect. In order to clarify the size effect, the powerful technique of EPR spectroscopy should not be underestimated.

6 Magnetism of Pt₁₃ Clusters

6.1 Introduction

Magnetically the Pt₁₃ cluster in NaY zeolite behaves as a superparamagnet although bulk Pt is not magnetic [7]. The growth of magnetism in small particles can be explained by the perturbation of coordination or formation of high spin states in a highly symmetric structure. The presence of high spin states found with up to eight unpaired electrons per icosahedral Pt₁₃ cluster provides a high magnetization to the cluster. Moreover, the chemical bonds and magnetic interactions with surrounding atoms or clusters modify the magnetic properties. The Pt₁₃ particles covered by hydrogen atoms have less magnetization because each adsorbed hydrogen atom binds one of the unpaired electrons [7]. A theoretical study of hydrogen adsorption over an icosahedral Pd₁₃ cluster showed that one H reduces the magnetic moment by one μ_B [112]. In particular, each hydrogen atom takes one electron till the magnetization should be expected to be zero, but additional hydrogen increases and decreases again the magnetization for each set of degenerate orbitals (Fig. 6.1). Therefore, it should be possible to oscillate the magnetization depending on the hydrogen coverage, a prediction that awaits experimental verification [30].

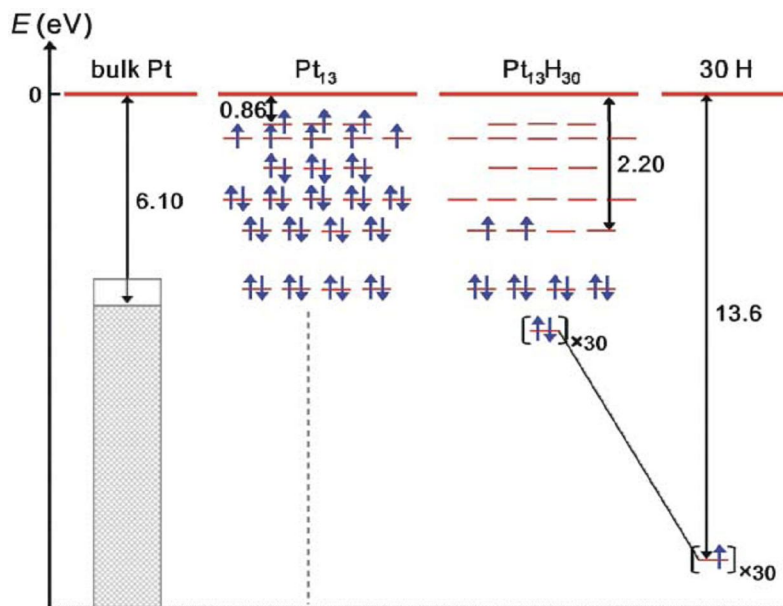


Figure 6.1: The representation of the d -band in bulk Pt metal and of the energy level structures and populations in Pt_{13} and $Pt_{13}H_{30}$ [30].

The icosahedral structure of Pt_{13} clusters consisting of 12 surface Pt atoms with one core Pt atom has been characterized by EXAFS and EPR techniques [8]. An asymmetry of the surface d electrons bands related by surface local symmetry causes a high surface atomic orbital moment [113]. In order to clarify the orbital contribution to magnetization, X-ray magnetic circular dichroism (XMCD) was used at the Pt $L_{2,3}$ edges on 13-atom Pt clusters with and without hydrogen adsorption.

XMCD is one of the most important discoveries in the field of magnetism. Erskine and Stern first suggested the XMCD phenomenon in 1975 [114] and the technique has been developed in the last two decades. It provides many possibilities that are not afforded by traditional magnetic techniques [115].

XMCD measures the difference in absorption of right- and left- circularly polarized X-rays (RCP and LCP, respectively) to deduce the magnetization of a sample, thus it is an element specific technique. In contrast to other techniques, XMCD provides information on the spin and orbital magnetization separately with its sensitivity in the detection of very small magnetic moments of $0.001 \mu_B$ per atom [116].

The physical origin of XMCD is most easily understood with the so-called two-step model. The first step describes the RCP and LCP angular momentum transformation to the excited photoelectron. If the photoelectron is excited from a spin-orbit level, such that the $p_{3/2}$ level (L_3 edge) or $p_{1/2}$ level (L_2 edge), the angular momentum of the photon is transferred in part to the spin through the spin-orbit coupling (Fig. 6.2). The RCP and LCP transfer an opposite angular momentum to the electron, so opposite spins are created in the two cases. In addition, the spin polarization will be opposite at the L_3 and L_2 edges, because the $p_{3/2}$ and $p_{1/2}$ levels have opposite spin-orbit coupling (l+s and l-s, respectively).

In the ferromagnetic sample, the number of empty spin-up and spin-down states are not the same, so the valance shell acts as a detector for the spin momentum. The magnetization direction can be used as the quantization axis of the detector, and a maximum dichroism effect is obtained with a parallel photon spin direction. The differences of the absorption (white line) intensities recorded with RCP and LCP (*i.e.*, the XMCD intensities) are shown as A (L_3 edge) and B (L_2 edge), respectively. A method of sum rule finds the spin moment quantitatively by using these measured intensities in the shape of $A-2B$ [117]. Similarly, if there is an imbalance of states with different magnetic quantum numbers, the valance shell acts as an orbital momentum detector. Again, the sum rule reveals the orbital moment by summing the dichroism intensities $A+B$ [118].

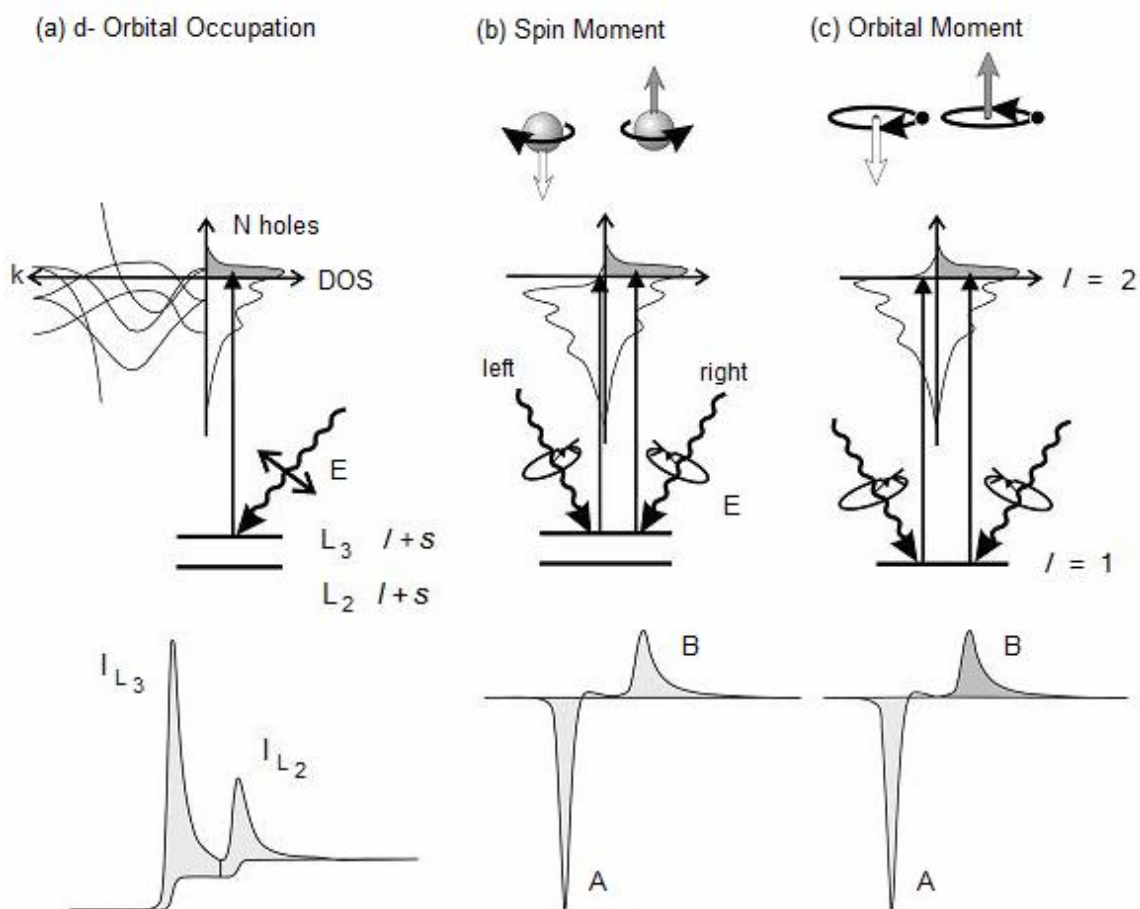


Figure 6.2: (a) Electronic transitions in L-edge X-ray absorption, (b) and (c) XMCD, illustrated in a one-electron model. The electron transitions occur from the spin-orbit split $2p$ core shell to empty conduction band states above the Fermi level. The white line intensities are shown by I_{L_3} and I_{L_2} , and the dichroic intensities are shown by A and B [113].

6.2 Experimental Part

The samples of $Pt_{13}H_m$ and Pt_{13} were prepared according to the procedure outlined in section 3.1.2. They were prepared as 5 mm diameter x 1 mm thick pellets in a glovebox

and protected in a glass capsule for transport. The capsule was opened in a glovebox filled with Ar gas and the pellet was inserted in a custom built sample holder, covered with a Kapton foil (0.2 mm thick), and sealed with a pressure ring. The sample holder with the sealed sample inside was screwed at the cold finger of the flow cryostat.

The experiment was performed at the ID 12 beamline at the ESRF in the spare time of experiment number HE 2541 in collaboration with the group of Prof. Juan Bartolomé from Zaragoza University. At the ID 12 beamline, the undulators APPLE-II and Helios II were employed, and a Si(111) double crystal monochromator provided the monochromatized beam. The polarization was over 90% in all cases. The detection technique used was fluorescence in backscattering geometry. The XMCD signal was obtained by a direct difference of the XAS spectra recorded with opposite helicities at each magnetic fixed field for both orientations of the field. The field was applied with an incident angle of 75° with respect to the normal to the plate.

The following experiments were performed for the two samples:

- 1) XAS of the L_2 and L_3 edges of Pt, measured at $T=7$ K and $H=6$ T.
- 2) XMCD of the L_2 and L_3 edges of Pt, measured at $T=7$ K and $H=6$ T.
- 3) Field dependence of the XMCD of the L_3 edge of Pt, measured at $T=7$ K and field $-6 < \mu_0 H < 6$ T.

6.3 Results and Discussion

I prepared the samples and participated in the experiments at the ESRF. Data analyses, figures, and tables in this chapter were done by the group of Prof. Juan Bartolomé.

6.3.1 X-Ray Absorption Spectroscopy

The normalized X-ray absorption (XAS) spectra of Pt_{13} and $Pt_{13}H_m$ samples are displayed in Fig. 6.3, left, at the L_2 and L_3 absorption edges. For sake of comparison, these absorptions were plotted together with those of metallic Pt and Au films in Fig. 6.3, right.

The 13-atom Pt clusters show similar spectra to that of the Pt metal at the same edges. Moreover, the EXAFS undulations of both Pt clusters coincide in energy which shows that the Pt-Pt distance is not affected by the hydrogenation. The absorption spectra of metallic Pt and both Pt clusters have been normalized to a same undulation 30 eV above the Fermi energy, to determine the difference in area of the XANES peaks. Then, it is possible to make a qualitative analysis for the number of holes (n_h) in the Pt 5d band. The XAS white line intensity decreases in the order; $\text{Pt}_{13}\text{H}_m > \text{Pt}_{13} > \text{Pt metal}$, which shows that hydrogenation creates new holes in the 5d band (Fig. 6.3, right).

The Au XAS white line has been used to obtain a quantitative determination of n_h . The differences in the white line area of Pt clusters, $r = I_{L2} + I_{L3}$, where I_{L2} and I_{L3} are the integrated white line intensities after subtraction of the contributions from transitions to the continuum, with respect to the Au white line area are shown in Fig. 6. 3, right, and in Table 6.1.

Table 6.1: Parameters determined from XAS and XMCD measurements. (Analyses were performed by the group of J. Bartolomé)

System	H_{appl} (T)	r (eV)	n_h	$p \times 10^2$ (eV)	$q \times 10^2$ (eV)	m_L/m_S	$m_L \times 10^3$ (μ_B/Pt)	$m_S \times 10^3$ (μ_B/Pt)	$m_T \times 10^3$ (μ_B/Pt)
Pt_{13}	6	8.30	1.85	-5.05(4)	-3.72(7)	0.32(2)	5.49(9)	17.1(6)	22.6(9)
Pt_{13}H_m	6	8.53	1.87	-6.22(6)	-4.37(9)	0.29(2)	6.39(7)	21.8(6)	28.2(9)
Pt foil [119]	7	7.44	1.73			0.38	2.1	5.5	7.6

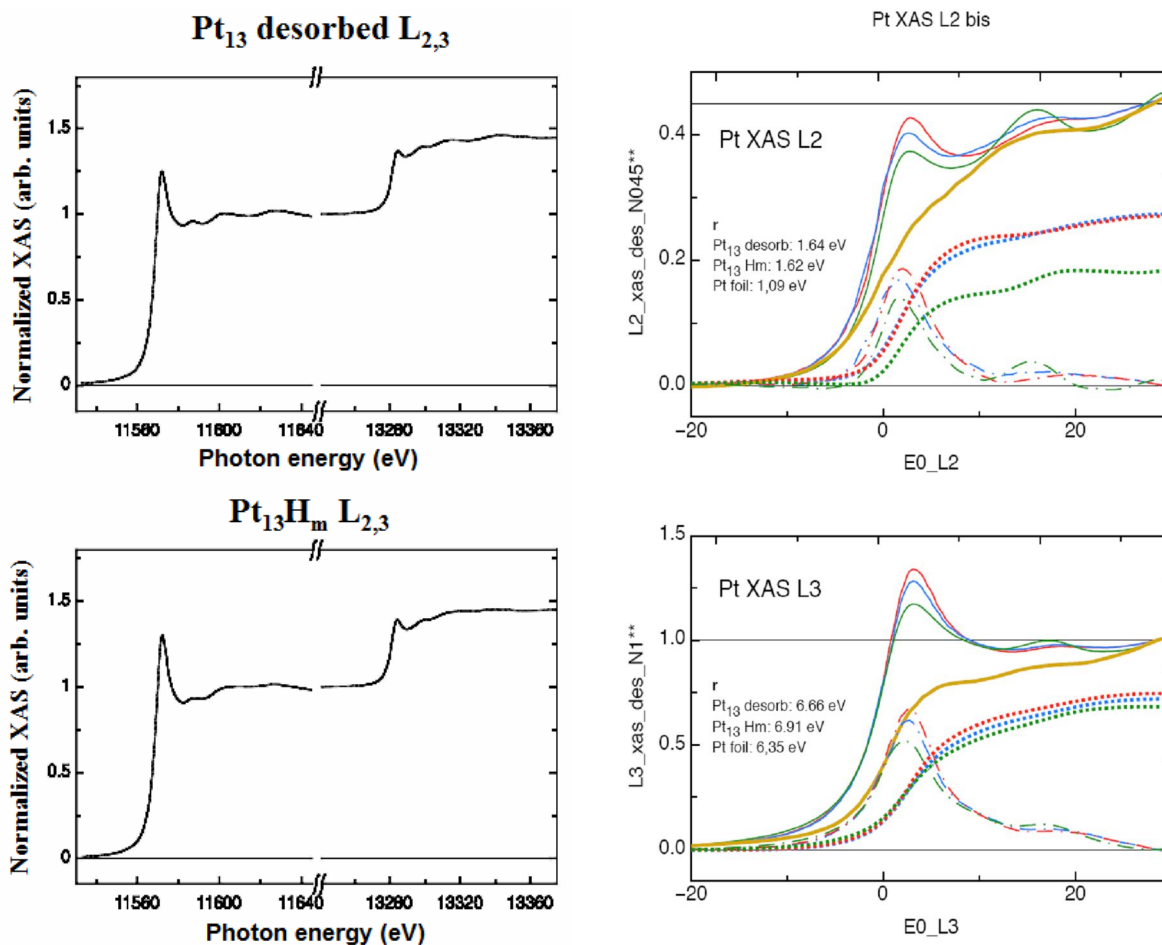


Figure 6.3: Left: XAS at the L₃ and L₂ edges of the Pt₁₃ desorbed and hydrogenated compounds, normalized to 1 for L₃ and 0.45 for L₂. Right: Comparison of XAS spectra at the L₃ and L₂ edges of the Pt₁₃ desorbed (blue), hydrogenated (red), Pt metal film (green) and Au metal film (yellow). The differences with respect to the Au white lines are shown (dash dots). The integrated difference areas “r” are shown (dotted line). (Measurements and analyses were performed by the group of J. Bartolomé)

The calculation of n_h was done according to [120] with the help of the theoretical numbers of d holes in three steps. In the first step, the difference between n_h values of Pt

metal and the Au metal $\tilde{n}_h = n_h^{Pt} - n_h^{Au} = 0.98$ ($n_h^{Pt} = 1.73$ and $n_h^{Au} = 0.75$) was calculated [120]. The scaling factor $C^{-1} = \frac{\tilde{n}_h}{r_{Pt\text{film}}} = 0.132$ holes/eV was found in the

second step from the experimental value of the Pt film, $r_{\text{film}} = 7.44$ eV. The final step gave the absolute number of holes for each Pt cluster by $n_h = n_h^{Au} + C^{-1}r$ (Table 6.1).

The number of holes per Pt atom is found as an averaged value in the sample, whether including in a cluster or not. A clear increase in n_h was obtained for the Pt₁₃ cluster compared to that in the Pt foil, and a small but detectable increase in the number of holes was obtained by hydrogenation of Pt₁₃ cluster.

6.3.2 XMCD Measurements

The differences of the integrated white line intensities recorded with RCP and LCP as A (L₃ edge) and B (L₂ edge) with an excellent signal to noise ratio are shown in Fig. 6.4.

Through the sum rules [117, 118], the spin and orbital moments averaged over all Pt atoms were calculated and included in Table 6.1. The n_h values and the constant $C = (I_{L2} + I_{L3}) / n_h$ were determined in the previous section. The spin (m_s) and orbital (m_L) component of the magnetic moment can be calculated by the sum rule equations;

$(A-2B) = -Cm_s / \mu_B$ and $(A+B) = -3Cm_L / 2\mu_B$, respectively [113]. A and B are the integrated areas of the L₃ and L₂ XMCD peaks, respectively, and the parameters in Fig. 6.4 are shown as $p = A$ and $q = A+B$.

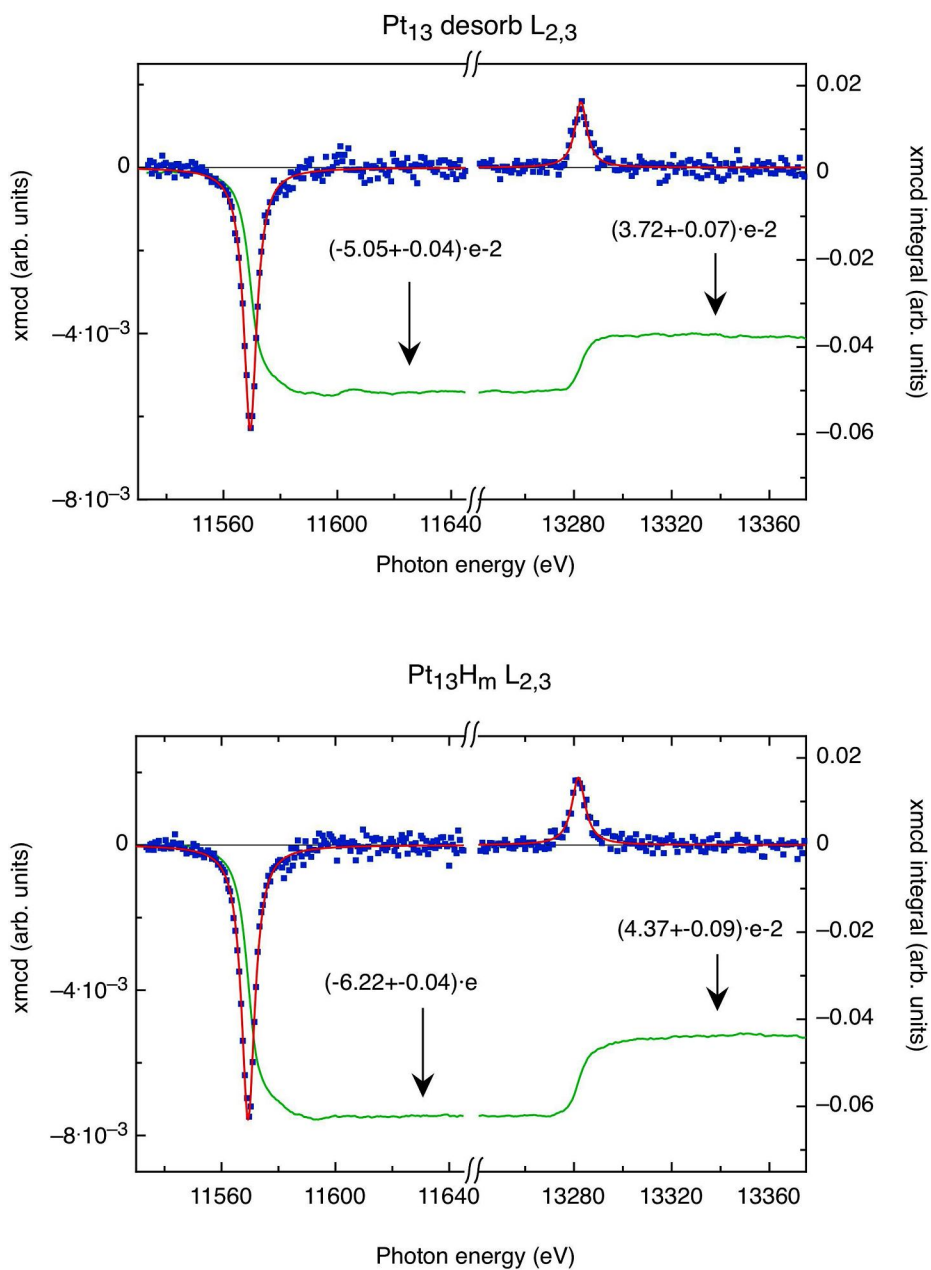


Figure 6.4: XMCD measurements at the L₃ and L₂ edges of the Pt₁₃ (top) and Pt₁₃H_m (down) samples (blue). The red lines show fit results of the Lorentzian functions and the green lines show the integral area of the Lorentzian functions. The arrows indicate the higher limit of the p and q integrals. (Measurements and analyses were performed by the group of J. Bartolomé)

Magnetization measurements at constant energy (*i.e.* at the energy of the peak, by changing the helicity of the incoming beam) and varying the field from -6 to +6 T were performed. The absolute scale, in μ_B/Pt , was fixed at $H = 6$ T to the values of total magnetic moment, m_T , derived above from the sum rules. The resulting field dependence $M(H)$ data fit to Langevin function are shown in Fig. 6.5.

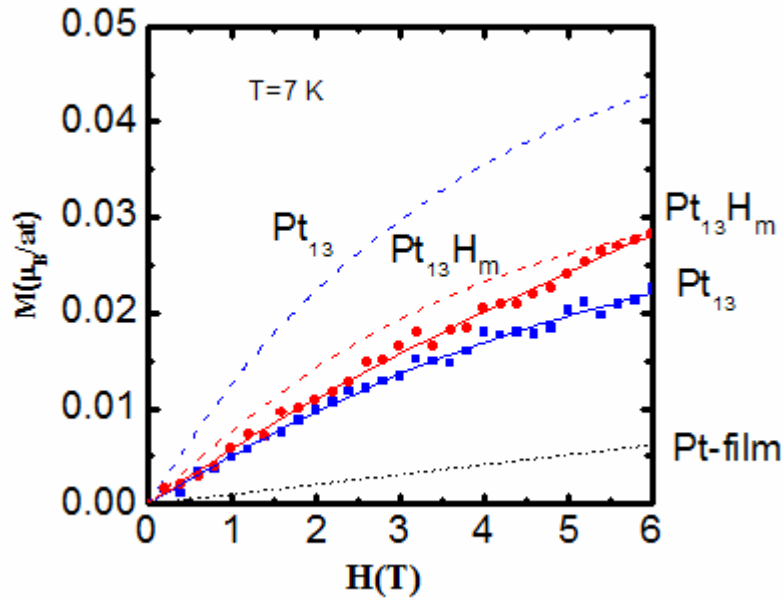


Figure 6.5: Comparison of $M(H)$ curves: SQUID measurement at 1.8 K, scaled in field to 7 K by the corresponding states law (dash line), XMCD results: For Pt_{13} desorbed (blue dots), Pt_{13}H_m (red dots). Fits to the Langevin function (thick lines). Extrapolation for Pauli paramagnetic bulk Pt polarized magnetization by the applied field, from XMCD data [119]. (Measurements and analyses were performed by the group of J. Bartolomé)

The magnetizations of the Pt_{13} clusters are higher than that of bulk Pt metal as shown from magnetic measurements $m = 2.27 \times 10^{-3} \mu_B/\text{Pt}$, at $T = 4.2$ K and $H = 6$ T [29], or for a Pt thin film (Table 6.1 and Fig. 6.5). The XMCD results are similar to the SQUID data

but contrary to the SQUID results, the Pt₁₃ sample has a lower magnetization than that of Pt₁₃H_m. The comparison of XMCD and SQUID results will be shown in the next chapter with an additional calculation of SQUID parameters.

6.3.3 Fraction of Magnetic Pt₁₃ Clusters

Magnetization measurements of Pt₁₃ clusters using a superconducting quantum interference device (SQUID) were already published by Liu et. al [7]. The M(H) measurements at 1.8 K were fitted to the Langevin function:

$$M(H) = N\mu \left[\coth\left(\frac{\mu H}{k_B T}\right) - \frac{k_B T}{\mu H} \right] + \chi_0 H \quad (6.1)$$

where μ is the average magnetic moment per particle, N is the number of particles per mol, T is the temperature, H is the magnetic field, χ_0 is a temperature independent susceptibility due to a possible Pauli paramagnetic state of Pt, and M is given in units of emu/mol.

Taking the data from this M(H) figure from Ref. [7] and applying the same fit but considering it in two parts, new results were obtained. The prefactor in the first term of Eq. 6.1 scales the Langevin curve, giving information on the total magnetic moment in the sample, and therefore on the number of atoms that have magnetic moments, while the shape of the Langevin curve gives the magnetic moment of the individual particle. This curvature does not depend on the total magnetization; therefore, it is possible to obtain two independent informations; the magnetic moment, μ , of the particle and the fraction of magnetic atoms, f, per mol in the sample.

Table 6.2 summarizes the fit results of the new calculation and the results from Ref. [7] for Pt₁₃ and Pt₁₃H_m samples. The magnetic moment per magnetic cluster is $\mu \approx 5.9 \mu_B$ and $5.6 \mu_B$ (in terms of magnetic moment per Pt; $m_{at} = 0.45$ and $0.43 \mu_B$) for the desorbed and hydrogenated Pt₁₃ clusters, respectively. These results are one order of magnitude larger than the values in Ref. [7]; $m_{at} = 0.059$ for Pt₁₃ and $0.038 \mu_B$ for Pt₁₃H_m. But, the

parameter M_s in the Table 6.2 ($M_s = N\mu$) shows the saturation magnetization and provides the fraction of Pt atoms which are forming part of the magnetic clusters.

Table 6.2: Fit parameters performed by the group of J. Bartolomé and derived information from Ref. [7].

Compound	Pt ₁₃	Pt ₁₃ H _m
$\mu(\mu_B/\text{cluster})$	5.9007 ± 0.1651	5.6316 ± 0.0988
$m_{\text{at}}(\mu_B/\text{Pt atom})$	0.4539 ± 0.0127	0.4332 ± 0.0076
$M_{S=N\mu}$ (emu/mol)	346.7513 ± 5.3593	234.9212 ± 2.3844
$f m_{\text{at}}(\mu_B/\text{Pt atom})$	0.0621	0.0419
$f=13N/N_A$	0.136	0.097
$\chi_0(\text{emu/mol}) \times 10^4$	0.3134 ± 0.8088	-1.2023 ± 0.3555
$\mu(\mu_B/\text{atom})/13^{[7]}$	0.059	0.038
$\chi_0(\text{emu/mol})^{[7]} \times 10^4$	4	1

A new analysis of the inverse susceptibility data derived from Ref. [7] has been done for Pt₁₃ clusters taking into account the fraction of magnetic Pt clusters. From the fit to $\chi^{-1} = (T-\Theta)/C_m = A+BT$, the slopes $B = C_m^{-1} = 18.53$ and 48.78 mol/emu.K are obtained for Pt₁₃ and Pt₁₃H_m, respectively (Table 6.3). The formula for the Curie term for a mol of magnetic entities, each with an identical moment μ_{eff} in Bohr Magneton, is:

$$C_m (\text{emu} / \text{mol.K}) = N_A \mu_{\text{eff}}^2 / 3k_B = 0.1250 \mu_{\text{eff}}^2 \quad (6.2)$$

However, the actual formula for a system of identical clusters, each consisting of 13 atoms with moment μ for each cluster and only a fraction f of Pt atoms forming (part of) the magnetic clusters, is:

$$C_m (\text{emu} / \text{mol.K}) = N_{\text{Pt}}^{\text{clusters}} \mu^2 / 3k_B = (fN_A / 13) \mu^2 / 3k_B \quad (6.3)$$

therefore, $f\mu^2 / 13 = \mu_{\text{eff}}^2$.

Table 6.3: Fit parameters and magnetic moments deduced from the $\chi(T)$ data of Ref. [7].
(Analyses were performed by the group of J. Bartolomé)

	B	C_m	μ_{eff}^2	$\mu_{\text{eff}}(\mu_B)$	f	$\mu(\mu_B)$
Pt ₁₃	18.53	0.05397	0.43242	0.65759	0.136	6.4292
Pt ₁₃ H _m	48.78	0.0205	0.16426	0.4053	0.097	4.692

Substituting μ_{eff} obtained from Eq. 6.2 and $f = 0.136$ and 0.097 as deduced from the $M(H)$ fit, respectively, the magnetic moment of Pt₁₃ and Pt₁₃H_m clusters $\mu = 6.5$ and $4.7 \mu_B$ are obtained (Eq. 6.3). These values are comparable with the values of $\mu = 5.9$ and $5.6 \mu_B$ per cluster obtained from the $M(H)$ fit of XMCD and SQUID data, respectively.

6.3.4 Comparison of XMCD and SQUID results

Since the XMCD is an element selective technique, only the magnetization that arises from Pt is detected. Other possible magnetic impurities (Fe) give a contribution to the total magnetization during SQUID measurements but by subtracting magnetization of the same amount of sample without Pt can solve this problem. Besides, the orbital and spin magnetic moment contributions to the average magnetic moment can be determined by measuring XMCD at the $L_{2,3}$ Pt edges of Pt₁₃ and Pt₁₃H_m clusters.

SQUID results from Ref. [7] have been reanalyzed in the previous section, and the same analysis method has been applied to the XMCD data. To compare with the $M(H)$ SQUID data for $T = 1.8$ K, it was scaled to $T = 7$ K, since it is known that $M(H/T)$ is a common corresponding states law curve in H/T . Also, the magnetization is now given in μ_B per Pt, since this is the magnitude obtained from the XMCD results.

XMCD data fits have been done in three different ways; A) using free fit parameters (Fig. 6.6), B) the $\chi_0 = 0$ is fixed, meaning that no other magnetic contribution than that contributed by the Pt₁₃ is present (Fig. 6.7), C) the parameters of μ are fixed to the value determined in the $M(H)$ fits (Table 6.2, Fig 6.8).

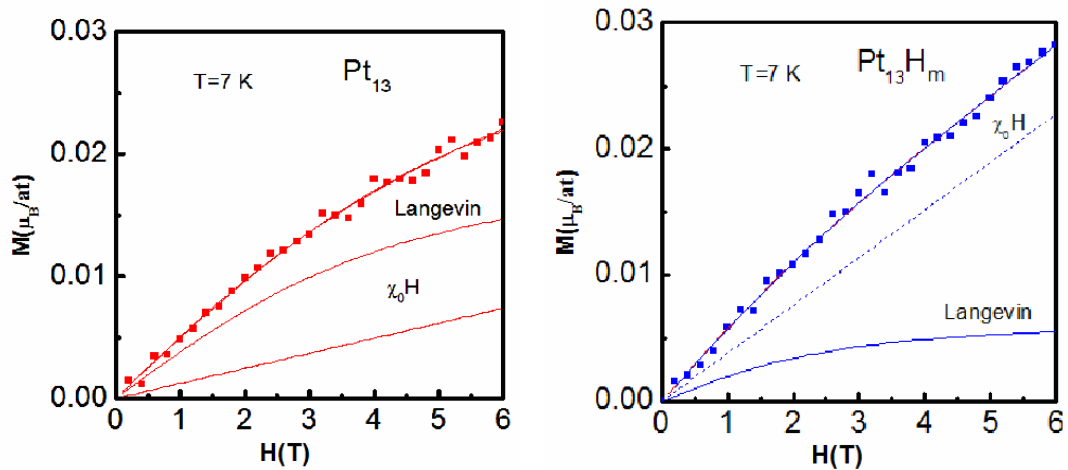


Figure 6.6: Fit of XMCD data to Eq. 6.1 The fitted curve is composed of a Langevin contribution plus a linear term.

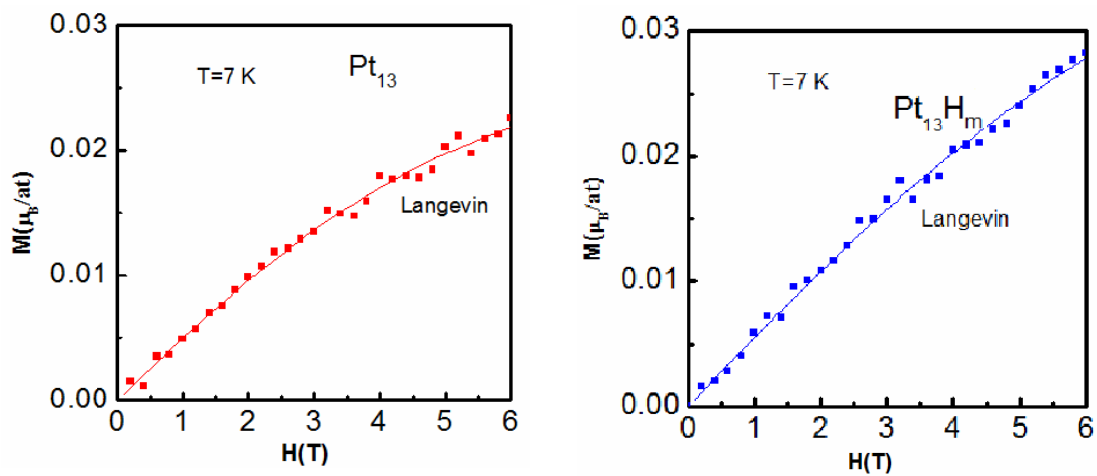


Figure 6.7: Fit of XMCD data to Eq. 6.1, with $\chi_0=0$. The fitted curve is just a Langevin function.

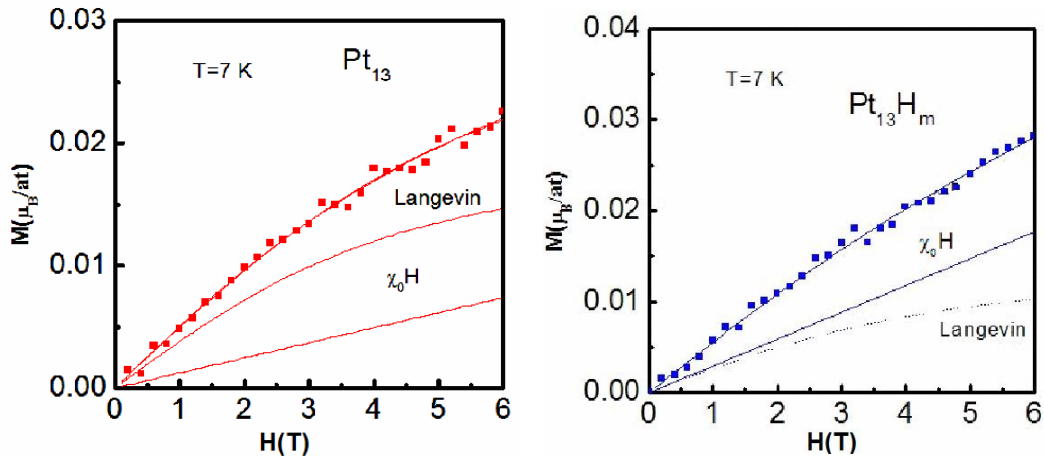


Figure 6.8: Fit of XMCD data to Eq. 6.1, with μ at fixed to the values from the fits to data in Ref. [7] (Table 6.2). The fitted curve is composed of a Langevin contribution plus a linear term. (Measurements and analyses were performed by the group of J. Bartolomé)

The quality of the fit is practically identical in all three cases. The fit results of Fig. 6.6 and 6.7, and the SQUID results (Table 6.2) of Pt_{13} with Eq.6.1 are shown in Table 6.4.

Table 6.4: Fit parameters for Eq.6.1, to the SQUID and XMCD data of Pt_{13} . (Analyses were performed by the group of J. Bartolomé)

Data	μ_{at}	μ	f	$\chi_0 \times 10^4$
SQUID	0.4539 ± 0.0127	5.9007 ± 0.1651	0.13681	0.3134 ± 0.8088
XMCD (Fig.6.6)	0.4569 ± 0.1721	5.9397 ± 2.2373	0.04423	0.00128 ± 0.0013
XMCD (Fig.6.7)	0.3448 ± 0.0210	4.4824 ± 0.2730	0.10184	0 ± 0

The moments per Pt₁₃ cluster, $\mu = 5.9 \mu_B/\text{cluster}$ ($\mu_{\text{at}} = 0.45 \mu_B$), determined from M(H) SQUID and XMCD (case A) show that two measurements are in full agreement. Besides, the percentage of magnetic Pt clusters is found to be 4.4% by XMCD, instead of 14% as obtained from the SQUID. The fit with the assumption that there is no linear term contribution leads to a minimum limit in the value of the cluster magnetic moment $\mu = 4.48 \mu_B$ with a fraction of magnetic Pt, $f = 10\%$, that is similar to derived from the M(H) SQUID fits. Therefore, the difference of f values between XMCD (case A) and SQUID fits originates from a temperature independent linear susceptibility contribution $\chi_0 H$.

On the other hand, the fit results of the Pt₁₃H_m sample for Eq. 6.1 to the SQUID and XMCD data depends very strongly on the constraints of the fit. Therefore, this determination for the magnetic moment and the fraction constant is not reliable.

Some other magnetic Pt samples in different size and configuration are shown along with our results in Table 6.5. The quality of the XMCD signal is excellent and the values obtained are reliable; $m_s = 17.1 \times 10^{-3} \mu_B$, $m_L = 15.5 \times 10^{-3} \mu_B$, and $m_L/m_s = 0.32$ for Pt₁₃ clusters. But, of course the data inform on the magnitudes averaged over all Pt atoms in the sample. The values of m_s and m_L for Pt₁₃ are about three times larger than that for the Pt foil that is assumed to have Pauli paramagnetism. This excludes Pauli paramagnetism as the type of field induced magnetism causing the XMCD observed signal in Pt₁₃. However, our results are one order of magnitude smaller than the observed ones in PtCo alloys, nanoparticles and bilayers [119, 121-126]. But, the previous analysis shows that only between 5 and 10% of the Pt is magnetic in the sample. Therefore, multiplication of m_s and m_L by 10 gives the same order of magnitude as for the other system in Table 6.5. This analysis shows that the hypothesis of the fraction of Pt contribution to the magnetization is robust. It is also interesting to note that the ratio of $m_L/m_s = 0.32$ is similar to the values of other Pt systems.

Table 6.5: Comparison of magnetic moment constants for Pt from this study and literature values. (Prepared by the group of J. Bartolomé)

System	H_{appl} (T)	m_L/m_S	$m_L \times 10^3$ (μ_B/Pt)	$m_S \times 10^3$ (μ_B/Pt)	$m_{\text{at}} \times 10^3$ (μ_B/Pt)
Pt ₁₃ desorbed	6	0.32(2)	5.49(9)	17.1(6)	22.6(9)
Pt ₁₃ H _m	6	0.29(2)	6.39(7)	21.8(6)	28.2(9)
Pt foil [119]	7	0.38	2.1	5.5	7.6
Pt/Co bilayer [122]	5				180
Pt ₅₀ Fe ₅₀ Nanoparticles [121]	2.8	0.13	54	410	464
Pt ₅₀ Co ₅₀ Nanoparticles [123]	0.6	0.30	70.1	230	300
Pt ₅₀ Co ₅₀ Thin film [124]	5	0.27	90	350	440
CoPt ₃ Thin film [126]	4	0.26	58	220	278

7 Summary

The present work is composed of three parts that deal with the characterization of supported paramagnetic Pt species in terms of electronic, structural, chemical and magnetic features. X-band EPR, XANES, EXAFS, FTIR and XMCD techniques were used as characterization techniques. The first part is focused on the synthesis of non-classical oxidation states of Pt in different zeolites (NaA, NaX, NaY and NaUSY) by an oxygen calcination method. The second part concentrates on the CO adsorption on the well-defined Pt₁₃ clusters in NaY. The last part studies magnetic properties of Pt₁₃ clusters using XMCD, and is concerned with magnetic analysis of Pt₁₃ clusters.

In order to prepare Pt samples in zeolites, a series of preparation methods must be carried out. A precursor complex of Pt(NH₃)₄²⁺ is introduced into the zeolites by an aqueous ion-exchange method. Na⁺ cations used for charge balance in zeolites with a low Si/Al ratio can easily exchange with the Pt(NH₃)₄²⁺ complex at 343 K. The subsequent calcination is done under oxygen flow at 573 K to decompose the amino groups. The heating rate and oxygen flow rate are two important parameters to control the autoreduction of Pt cations. The autoreduction occurs at high temperatures by hydrogen atoms released from amino groups. But, low heating rate (0.5 K min⁻¹) under high oxygen flow rate (100 mL min⁻¹ g⁻¹) avoids Pt^{δ+} from autoreduction. The chemical composition and structure of zeolites also influences the formation of Pt after calcination.

Monovalent and trivalent platinum cations called non-classical oxidation states, were both stabilized in NaX zeolite after oxygen calcination. The low Si/Al ratio (Si/Al = 1.23) of the zeolite and the formation of Brønsted acid centers during the autoreduction process

help to obtain these states. Characterization of the Pt cations was done by XANES, EXAFS, FTIR and mainly X-band EPR.

- (1) The comparison of XANES spectra of calcined Pt in NaX, NaY and NaA zeolites with PtO₂ and bulk Pt shows that Pt has higher oxidation states after calcination. Isolated Pt cations coordinated only by zeolite framework oxygen and Si(Al) atoms but not with other Pt atoms were determined from EXAFS measurements.
- (2) Paramagnetic Pt⁺ and Pt³⁺ cations were assigned by X-band EPR spectroscopy. Their appearance and interchange were confirmed by applying slow (0.5 K min⁻¹) and fast (1.25 K min⁻¹) calcination heating rate experiments, hydrogen adsorption experiments and comparison with literature *g* values.
- (3) Pt³⁺ could not be obtained in NaY (Si/Al = 2.31) after calcination, but Pt⁺ could be stabilized with various calcination procedures. This situation completely agrees with the expectation that the lower aluminum content which goes along with less negative charge on the lattice cannot stabilize highly charged cations. The EPR result of activated Pt⁺ in NaY, *g*_{iso} = 2.33, shows a very similar value of *g*_{iso} = 2.34 for Pt⁺ in NaX.
- (4) FTIR spectroscopy using CO as a probe molecule also permits the assignment of Pt oxidation states, including those of the diamagnetic ions. Pt²⁺ is not the only product upon oxygen calcination, in agreement with EPR it was found that also Pt⁺ and Pt³⁺ can be obtained in significant amounts (7% of total Pt) in NaX zeolite.
- (5) When Linde type A zeolite (LTA) is used instead of faujasite, the final formation of paramagnetic Pt is affected by the structure difference, and a well defined Pt dimer was obtained instead of isolated ions. EPR spectra reveal orthorhombic symmetry and a multiplet that represent properly the distribution of the Pt isotopes based on their natural abundance.

The simultaneous stabilization of the oxidation states 0, + 1, + 2 and + 3 in polar zeolites may be beneficial to oxidation catalysis as it should allow high flexibility in single electron transfer processes. This has not yet been explored experimentally. The Pt dimer

was obtained without using hydrogen reduction, in future it is therefore worth checking for the formation of other Pt_n species ($n > 2$) on oxygen calcination in NaA zeolites. The calcination step was followed by hydrogen reduction to synthesize Pt_{13} clusters in NaY zeolites. The bigger Pt particles could be obtained if the $Pt(NH_3)_4^{2+}$ complexes are directly reduced by hydrogen at high temperatures. Therefore, calcination is a crucial step to get small nanoparticles. The hydrogen flow rate ($25 \text{ mL min}^{-1} \text{ g}^{-1}$), heating rate (6 K min^{-1}) and maximum temperature (473 K) are the important parameters for the synthesis of Pt_{13} clusters. In addition, CO molecules can diffuse into channels and pores, and react with the cluster. CO adsorption leads to a complete decomposition of the cluster and to the formation of new $Pt_2(CO)_m$ ($m = 4, 5$) species, most probably stabilized by the zeolite walls. Paramagnetic properties of these Pt samples were utilized to investigate the structure of the small clusters by using EPR hyperfine structure. Before the CO adsorption, an EPR multiplet with 13 splitting was assigned to a Pt_{13} cluster ($g_{iso} = 2.35$) with 12 equivalent surface Pt atoms, and one core Pt atom without unpaired electron density. However, after the CO adsorption, the multiplet disappeared and a new spectrum ($g_{iso} = 1.98$) with one main signal and two satellites on both sides was assigned to a Pt dimer. In-situ EXAFS measurements which are consistent with EPR results showed that the 13-atom Pt cluster decomposed into Pt dimers. Furthermore, two different Pt-C contributions were detected, one at 1.95 \AA and the other at 2.14 \AA with coordination numbers of 0.8 and 1.7, respectively. The number of bonded CO on a per Pt atom basis is difficult to obtain but the analysis of C-O stretching frequencies helped in determining one type of linearly adsorbed CO at 2080 cm^{-1} , and two bridge bonded CO at $\nu_s = 1893 \text{ cm}^{-1}$ and $\nu_{as} = 1840 \text{ cm}^{-1}$, which is again compatible with EXAFS results. In addition, a further bridge bonded species at 1813 cm^{-1} is preferentially formed during desorption-adsorption cycles. A cationic platinum carbonyl species has also been seen with a band at 2108 cm^{-1} , but the main complex has an absorption band at 2080 cm^{-1} , belonging to the neutral Pt_2^0 -CO structure.

This study also demonstrates the use of the various complementary methods to understand the structure of small clusters. Although EPR spectroscopy is not yet used extensively in the field of catalysis, paramagnetism offers a good possibility to follow chemical reactions and to understand the geometry of the species.

Although bulk Pt is not magnetic, small Pt₁₃ clusters show extraordinary magnetization depending on their high spin ground state. Magnetic behavior of Pt₁₃ clusters have already been studied by SQUID [7], but the analysis was repeated in terms of a Langevin and a linear field dependent term, and in contrast the element specific technique of XMCD was used to find out spin (m_S) and orbital (m_L) magnetic moments. The number of holes in 5*d* band (n_h), m_S and m_L values of Pt clusters were found to be several times larger than in metallic Pt by XMCD.

The reanalysis of SQUID data revealed that the average moment per cluster is $\mu = 5.9$ and $5.6 \mu_B$ for the Pt₁₃ and Pt₁₃H_m clusters, respectively with quite different results than 8.45 and $5.8 \mu_B$ [7]. Furthermore, the amount of Pt located in magnetic clusters was found to be 14 and 10%, respectively.

The XMCD L_{2,3} Pt edge experiments for Pt₁₃ followed the Langevin type of dependence of the M(H) curve expected from SQUID measurements. The data obtained from XMCD measurements fitted to the same Langevin equation and gave a value of $\mu = 5.9 \mu_B$ identical to that found in the SQUID data. On the other hand, the percentage of Pt participating in magnetic cluster formation falls to 5%, and there is a more appreciable magnetic field dependent contribution. The magnetic moment of Pt₁₃H_m obtained from the M(H) fitting depended on the constraints of the fit, therefore it is not reliable.

The fraction of Pt₁₃ that forms magnetic clusters would be an explanation for getting very low EPR active Pt₁₃ cluster signals. EXAFS experiments showed that most Pt atoms form clusters, so a large number of Pt₁₃ clusters could be EPR silent or diamagnetic.

Zusammenfassung

Die vorliegende Arbeit besteht aus drei Teilen, die sich mit der Charakterisierung von geträgerten paramagnetischen Pt-Spezies hinsichtlich ihrer elektronischen, strukturellen, chemischen und magnetischen Eigenschaften befassen. Dabei kamen folgende Techniken zum Einsatz: X-Band-ESR, XANES, EXAFS, FTIR und XMCD. Der erste Teil fokussiert sich auf die Synthese nicht-klassischer Pt-Oxidationszustände in unterschiedlichen Zeolithen (NaA, NaX, NaY und NaUSY) durch eine Calcinierung mit Sauerstoff. Der zweite Teil konzentriert sich auf die CO-Adsorption auf umfassend charakterisierten Pt₁₃-Clustern in NaY. Der letzte Teil handelt von den magnetischen Eigenschaften der Pt₁₃-Cluster charakterisiert durch XMCD und beschäftigt sich mit der Untersuchung des Magnetismus der Pt₁₃-Cluster.

Für die Darstellung von Pt-Zeolith-Proben muss eine Reihe von Präparationsmethoden durchgeführt werden. Durch wässrigen Ionenaustausch kann der Edukt-Komplex Pt(NH₃)₄²⁺ in den Zeolith überführt werden. Die zur Elektroneutralität bei Zeolithen mit niedrigem Si/Al-Verhältnis vorhandenen Na⁺-Ionen können bei 343 K einfach durch den Pt(NH₃)₄²⁺-Komplex ausgetauscht werden. Die anschließende Calcinierung unter Sauerstofffluss wurde bei 573 K zur Abspaltung der Amin-Liganden durchgeführt. Die Heizrate und der Sauerstofffluss sind zwei zentrale Parameter zur Kontrolle der Autoreduktion der Pt-Kationen. Die Autoreduktion tritt bei hohen Temperaturen durch die Freisetzung von Wasserstoffatomen aus den Amin-Liganden auf. Allerdings kann bei einer niedrigen Heizrate (0.5 K min⁻¹) unter hohem Sauerstofffluss (100 mL min⁻¹ g⁻¹)

$\text{Pt}^{\delta+}$ durch Autoreduktion vermieden werden. Ebenso beeinflusst die Zusammensetzung und Struktur der Zeolithe die Bildung von Pt nach der Calcinierung.

Einwertige und dreiwertige Pt-Kationen werden als nicht-klassische Oxidationszustände bezeichnet. Beide waren nach der Calcinierung mit Sauerstoff im Zeolith NaX stabil. Das niedrige Si/Al-Verhältnis ($\text{Si/Al} = 1.23$) des Zeoliths und die Bildung von Brønsted-Säurezentren während des Autoreduktionsprozesses helfen diese Zustände zu erhalten. Die Charakterisierung dieser Pt-Kationen wurde mit XANES, EXAFS, FTIR und hauptsächlich X-Band-ESR durchgeführt.

- (1) Der Vergleich der XANES-Spektren von calciniertem Platin in den Zeolithen NaX, NaY und NaA mit PtO_2 und Pt-bulk zeigt, dass Pt nach der Calcinierung einen höheren Oxidationszustand besitzt. Isolierte Pt-Atome koordinieren nur mit den Sauerstoff-, Silicium- und Aluminiumatomen des Zeolithgerüsts, aber nicht mit anderen Pt-Atomen, wie EXAFS-Messungen ergaben.
- (2) Paramagnetische Pt^+ - und Pt^{3+} -Kationen wurden durch X-Band-ESR-Spektroskopie bestimmt. Ihr Auftreten und gegenseitiger Austausch wurde experimentell unter Variation der Heizrate (0.5 K min^{-1} bis 1.25 K min^{-1}), durch Versuche zur Wasserstoffadsorption und den Vergleich mit Literaturwerten von g -Faktoren bestätigt.
- (3) Pt^{3+} konnte nach Calcinierung in NaY ($\text{Si/Al} = 2.31$) nicht erhalten werden, aber Pt^+ konnte mithilfe diverser Abläufe der Calcinierung stabilisiert werden. Dieser Umstand steht in völliger Übereinstimmung mit der Erwartung, dass ein niedriger Aluminiumgehalt, der mit einer niedrigen Gesamtladung des Zeolithgerüsts einhergeht, keine hoch geladenen Kationen stabilisieren kann. Das ESR-Ergebnis für aktiviertes Pt^+ in NaY, $g_{\text{iso}} = 2.33$, zeigt einen ähnlichen Wert für $g_{\text{iso}} = 2.34$ für Pt^+ in NaX.
- (4) Die FTIR-Spektroskopie, die CO als Testmolekül benützt, ermöglicht ebenfalls die Zuweisung der Oxidationszustände von Pt und diamagnetischer Ionen. Pt^{2+} ist nicht das einzige Produkt nach der Calcinierung mit Sauerstoff. In Übereinstimmung mit

ESR wurde festgestellt, dass außerdem Pt^+ und Pt^{3+} in erheblicher Menge (7% des gesamten Platins) im Zeolith NaX erhalten wurden.

- (5) Bei der Verwendung des Zeoliths Linde Typ A (LTA) anstelle von Faujasite wird die endgültige Bildung paramagnetischen Platins durch die Unterschiede in der Struktur beeinflusst und ein wohl definiertes Pt-Dimer anstelle isolierter Ionen erhalten. Die ESR-Spektren zeigen orthorhombische Symmetrie und ein Multiplett, das die genaue Aufteilung der Pt-Isotope bezogen auf ihre natürliche Häufigkeit wiedergibt.

Die gleichzeitige Stabilisierung der Oxidationszustände 0, +1, +2 und +3 in polaren Zeolithen ist eventuell förderlich für die oxidative Katalyse, da sie eine hohe Flexibilität für Ein-Elektronen-Transfer-Prozesse ermöglicht. Dies wurde experimentell bisher nicht untersucht. Das Pt-Dimer wurde ohne die Reduktion von Wasserstoff erhalten. In Zukunft wäre es daher sinnvoll, nach der Calciniierung mit Sauerstoff den Zeolith NaA auf die Bildung anderer Pt_n -Spezies ($n > 2$) zu überprüfen.

Zur Synthese von Pt_{13} -Clustern im Zeolith NaY folgt auf die Calciniierung eine Reduktion mit Wasserstoff. Falls die $\text{Pt}(\text{NH}_3)_4^{2+}$ -Komplexe bei höheren Temperaturen direkt reduziert werden, entstehen größere Pt-Partikel. Deshalb ist die Calciniierung ein entscheidender Schritt, um kleine Nanopartikel zu erhalten. Der Wasserstofffluss ($25 \text{ mL min}^{-1} \text{ g}^{-1}$), die Heizrate (6 K min^{-1}) und die Endtemperatur (473 K) sind die wichtigsten Parameter für die Synthese von Pt_{13} -Clustern. Ferner können die CO-Moleküle in die Kanäle und Poren diffundieren und mit den Clustern reagieren. Die CO-Adsorption führt zu einem vollständigen Zerfall der Cluster und zur Bildung neuer $\text{Pt}_2(\text{CO})_m$ -Spezies ($m = 4.5$), die vermutlich größtenteils durch das Zeolithgerüst stabilisiert werden. Die paramagnetischen Eigenschaften dieser Pt-Proben werden dazu benutzt, um die Struktur dieser kleinen Cluster mithilfe der ESR-Hyperfein-Struktur zu erforschen. Vor der CO-Adsorption wurde dem Multiplett mit 13 Linien ein Pt_{13} -Cluster ($g_{\text{iso}} = 2.35$) mit 12 äquivalenten Pt-Atomen an der Oberfläche des Clusters und ein Pt-Atom im Zentrum des Clusters ohne Elektronendichte zugeordnet. Nach der CO-Adsorption verschwand das Multiplett. Dem neuen Spektrum ($g_{\text{iso}} = 1.98$) mit einem Hauptsignal und je einem Satellit auf beiden Seiten wurde ein Pt-Dimer zugeordnet. In-situ-EXAFS-Messungen,

die mit den ESR-Ergebnissen übereinstimmen, zeigten, dass der 13-atomige Pt-Cluster in Pt-Dimere zerfällt. Darüber hinaus wurden zwei verschiedene Pt-C-Beiträge detektiert, einer bei 1.95 Å und der andere bei 2.14 Å mit entsprechenden Koordinationszahlen von 0.8 und 1.7. Die Anzahl pro Pt-Atom gebundener CO-Moleküle ist schwierig zu erhalten, jedoch ist die Analyse der C-O-Streckfrequenzen bei der Bestimmung der einzelnen Banden hilfreich. Ein linear adsorbiertes CO-Molekül bei 2080 cm⁻¹ und zwei verbrückt gebundene CO-Moleküle bei $\nu_s = 1893$ cm⁻¹ und $\nu_{as} = 1840$ cm⁻¹ wurden gemessen und stimmten erneut mit den EXAFS-Ergebnissen überein. Zusätzlich wird eine weitere, vornehmlich verbrückt gebundene Spezies bei 1813 cm⁻¹ im Verlauf von Desorptions-Adsorptions-Zyklen gebildet. Außerdem wurde eine kationische Platin-Carbonyl-Spezies mit einer Bande bei 2108 cm⁻¹ beobachtet während der Hauptkomplex eine Absorptionsbande zugehörig zur neutralen Pt₂⁰-CO-Struktur bei 2080 cm⁻¹ besitzt.

Diese Untersuchungen zeigen auch den Nutzen unterschiedlicher, sich ergänzender Methoden, die zum besseren Verständnis der Struktur kleiner Cluster beitragen. Obgleich die ESR-Spektroskopie noch nicht umfassend auf dem Feld der Katalyse zum Einsatz kommt, bietet der Paramagnetismus eine gute Möglichkeit, chemische Reaktionen zu verfolgen und die Geometrie einer Spezies zu verstehen.

Obwohl Pt-bulk nicht magnetisch ist, zeigen kleine Pt₁₃-Cluster eine außergewöhnliche Magnetisierung in Abhängigkeit von ihrem high-spin-Grundzustand. Das magnetische Verhalten der Pt₁₃-Cluster wurde bereits mehrfach durch SQUID-Messungen studiert [7]. Die Auswertung wurde unter Langevin-Bedingungen und Bedingungen linearer Feldabhängigkeit wiederholt. Im Gegensatz hierzu wird die grundlegende und präzise Technik der XMCD zur Feststellung des magnetischen Spin- (m_S) und Bahnmoments (m_L) benutzt. Durch XMCD wurde herausgefunden, dass die Anzahl an Löchern im 5d-Band (n_h) und die Werte für m_S und m_L der Pt-Cluster mehrfach größer sind als bei metallischem Platin.

Die erneute Analyse der SQUID-Daten zeigte, dass das durchschnittliche Moment pro Cluster für Pt₁₃ $\mu = 5.9$ und für Pt₁₃H_m 5.6 μ_B beträgt, mit jeweils verschiedenen

Ergebnissen von 8.45 und 5.8 μ_B [7]. Außerdem wurde für die in magnetischen Clustern gebundene Menge an Platin entsprechend ein Wert von 14 und 10% des gesamten Platins gefunden.

Die XMCD-Experimente für Pt₁₃ zur L_{2,3}-Pt-Grenze folgten dem Langevin-Typ für die Abhängigkeit der M(H)-Kurve wie sie bei SQUID-Messungen erwartet wird. Die aus XMCD-Messungen erhaltenen Daten wurden an dieselbe Langevin-Funktion angepasst und ergaben einen Wert von $\mu = 5.9 \mu_B$, der identisch mit dem aus SQUID-Messungen gefundenen Wert ist. Andererseits fällt der an der magnetischen Clusterbildung beteiligte Anteil an Pt auf 5% und zeigt einen nennenswerten Beitrag zur magnetischen Feldabhängigkeit. Das erhaltene magnetische Moment aus der M(H)-Anpassung für Pt₁₃H_m ist von deren Grenzen abhängig und deshalb nicht verlässlich.

Der Bruchteil an Pt₁₃, der magnetische Cluster bildet, könnte eine Erklärung für die sehr niedrige ESR-aktive Pt₁₃-Cluster-Signalintensität sein. EXAFS-Experimente zeigten, dass die meisten Pt-Atome Cluster bilden, so dass eine große Zahl an Pt₁₃-Clustern ESR-inaktiv oder diamagnetisch sein könnte.

Abbreviation

α	electron-spin state with $M_s = +1/2$
β	electron-spin state with $M_s = -1/2$
β_e	Bohr magneton
β_n	nuclear magneton
δ_j	overall phase shift
ΔE	difference of energy
θ	angle
Θ	Curie-Weiss temperature
λ	spin-orbit coupling constant
μ	magnetic moment
μ_{ez}	electron dipole moment
μ_{nz}	nuclear dipole moment
μ_B	Bohr magneton
μ_{eff}	effective magnetic moment
σ	Debye-Waller like factor
ν	frequency
χ	magnetic susceptibility
χ_{CW}	Curie-Weiss susceptibility
χ_0	temperature independent magnetic susceptibility

χ_m	molar magnetic susceptibility
$ \psi_0 ^2$	probability of finding the electron at the nucleus
A	area of the circle
A	hyperfine coupling tensor
A_{iso}	isotropic hyperfine coupling constant
Abs	X-ray absorbing atom
B	external magnetic field
B_s	backscatterer
C_m	molar Curie constant
CN	coordination number
cw	continuous wave
DFT	density functional theory
E	energy
E_f	Fermi energy level
EPR	electron paramagnetic resonance
ESR	electron spin resonance
EXAFS	extended X-ray adsorption fine structure
FTIR	fourier transform infrared
g	g factor
g_e	g factor of free electron
g_n	nuclear g factor
G	gauss
h	Planck's constant
H	magnetic field
\hat{H}	spin Hamiltonian operator
i	effective circulating electric current

I	primary quantum number of nuclear spin
\hat{I}	nuclear spin vector
$I(E)$	transmitted X-ray intensity
$I_0(E)$	incident X-ray intensity
F_j	backscattering amplitude
k_B	Boltzmann constant
KL	potassium form of zeolite L
\hat{L}	total electronic orbital angular momentum operator
LCP	left- circularly polarized X-rays
LTA	Linda type A
m	mass of particle
M	magnetization
M_{rem}	remanent magnetization
m_{at}	atomic magnetic moment
m_L	orbital magnetization
m_S	spin magnetization
m_T	total magnetization
M_s	saturation magnetization
M_S	secondary quantum number for electron-spin angular momentum
M_I	secondary quantum number for nuclear-spin angular momentum
N_A	Avogadro's number
NaA	sodium form of zeolite A
NaUSY	sodium form of zeolite ultra stable Y
NaX	sodium form of zeolite X
NaY	sodium form of zeolite Y
n_h	number of holes
N_j	number of neighbor atoms
NMR	nuclear magnetic resonance

PEMFC	polymer electrolyte membrane fuel cell
PVP	poly-N-vinyl-2-pyrrolidone
q	charge of a particle
R-factor	quality of fit
RCP	right- circularly polarized X-rays
r	radius
r	distance between the electron and nuclear dipole moment
r_j	distance of atoms j from the X-ray absorbing atom
\hat{S}	electron spin operator
S_0^2	amplitude reduction factor
SOMO	semiooccupied atomic or molecular orbital.
SQUID	superconducting quantum interference device
T	temperature
T	tesla
T_b	blocking temperature
T_C	Curie temperature
T_N	Néel temperature
U	energy
XANES	X-ray absorption near edge structure
XMCD	X-ray magnetic circular dichroism

List of Figures

1.1	Structures of Pt ₁₃ and Pt ₁₃ H ₁₂ clusters.....	11
2.1	Structure of LTA zeolite with possible cationic sites.....	15
2.2	Structure of a faujasite zeolite.....	17
2.3	Principle of EPR spectroscopy; scanning the magnetic field to get resonance condition of a system with a nuclear spin number $I = 1$	21
2.4	Normalized XANES spectra comparing the L _{III} absorption edges of the 5 <i>d</i> metals Re through Au.....	25
4.1	Pt L _{III} -edge XANES spectra of zeolite samples after O ₂ calcination compared with PtO ₂ and Pt foil.....	39
4.2	Experimental $k^3 \cdot \chi(k)$ functions and the Fourier transforms of the filtered data of Pt/zeolite samples calcined with oxygen.....	41
4.3	EPR spectrum of the 6% Pt/NaX after calcination with a rate of 1.25 K min ⁻¹ recorded at 20 K and the corresponding simulation for Pt ⁺ and Pt ³⁺ ions.....	44
4.4	Comparison of the products of two different calcination rates: 1.25 K min ⁻¹ and 0.5 K min ⁻¹	47
4.5	Simulation and EPR spectrum of 6%Pt/NaX after O ₂ calcination at a rate of 0.5 K min ⁻¹ recorded at 20 K for Pt ⁺ (g _i) and Pt ³⁺ (g _i [↓]).....	48
4.6	Comparison of EPR spectra recorded at 20 K of the products obtained with three different calcination rates: 1.25 K min ⁻¹ , 0.5 K min ⁻¹ , and 0.15 K min ⁻¹	49

4.7	X-band EPR spectra of NaX loaded with (A) 12% (a), 6% (b), 0.5% (c) Pt and recorded at 20 K after O ₂ calcination with a rate of 0.5 K min ⁻¹ , and (B) enhanced spectrum obtained with 0.5% Pt/NaX	50
4.8	X-band EPR spectra of NaX loaded with 6% Pt after O ₂ calcination with a rate of 0.5 K min ⁻¹ , and recorded at 4, 10, 15, 20, 25, 30, 35, 40, 50, 60, and 75 K.....	51
4.9	Product of magnetization times temperature versus temperature and the reciprocal of magnetization versus temperature plots obtained with doubly integrated EPR spectra of 6% Pt/NaX after O ₂ calcination with a rate of 0.5 K min ⁻¹ recorded at different temperatures.	52
4.10	X-band EPR spectrum of 6% Pt/NaX recorded at 20 K after O ₂ calcination with a rate of 0.5 K min ⁻¹ , and after H ₂ addition to the same sample	53
4.11	FTIR spectra of CO adsorbed at 80 K on O ₂ calcined 6% Pt/NaX followed by evacuation at RT for 30 min (a), 40 min (b), 50 min (c), 60 min (d).....	55
4.12	Comparison of EPR spectra of the products recorded at 20 K, before CO adsorption and after CO adsorption at liquid nitrogen temperature and at room temperature	56
4.13	X-band EPR spectrum of 6% Pt/NaY recorded at 20 K after O ₂ calcination with a rate of 0.5 K min ⁻¹ up to 573 K, and up to 673 K.....	58
4.14	Experimental EPR spectrum of 6% Pt/NaY after O ₂ calcination at a rate of 0.5 K min ⁻¹ recorded at 20 K and simulation based on two different Pt ⁺ species	59
4.15	Simulated and experimental EPR spectrum of 1% Pt/NaA after O ₂ calcination with a rate of 0.5 K min ⁻¹ recorded at 20 K based on the Pt ₂ ^{x+}	60

4.16	Experimental EPR spectrum of 1% Pt/NaA, PtPd/NaA, and Pd/NaA after O ₂ calcination with a rate of 0.5 K min ⁻¹ up to 623 K recorded at 20 K.	61
4.17	Experimental EPR spectrum of 1% Pt/NaA, PtPd/NaA, and Pd/NaA after O ₂ calcination at 673 K.	62
4.18	Comparison of PtPd/NaA (673 K) with the sum of PtPd/NaA (623K) and Pd/NaA (673K).....	63
4.19	Structure fragment of faujasite Y zeolite, Al/Si atoms sitting at the vertices connected by an oxygen atom and the cation positions	65
5.1	XANES spectra of Pt/NaY samples measured at the Pt L _{III} -edge (11564 eV) at different stages of <i>in-situ</i> treatment.....	71
5.2	Experimental EXAFS function, its Fourier transform and theoretical fit to the experimental data of Pt ₁₃ H _m /NaY.....	73
5.3	Experimental EXAFS function, its Fourier transform and fit to the experimental data of Pt ₂ (CO) _m /NaY.....	75
5.4	Experimental EXAFS function and its Fourier transform of Pt ₁₃ H _m /NaY and Pt ₂ (CO) _m /NaY	76
5.5	X- band EPR of Pt ₁₃ D _m recorded at 20 K before and after adsorption of different doses CO and evacuation at room temperature; 50 mbar, 100 mbar, 125 mbar, 500 mbar	77
5.6	EPR spectra of ¹⁹⁴ Pt ₂ (CO) _m and natural abundance Pt ₂ (CO) _m recorded at 20 K after saturation adsorption of CO at room temperature.....	78
5.7	FTIR spectra recorded after CO adsorption (500 mbar) at 298 K on Pt ₁₃ H _m /NaY followed by evacuation at the same temperature for 3 min, 25 min, 45 min, 90 min.....	79
5.8	FTIR spectra recorded after CO adsorption (500 mbar) at 298 K on Pt ₁₃ H _m /NaY followed by evacuation at 298 K, 348 K, 373 K, 473 K, 523 K	80
5.9	FTIR spectra of CO adsorbed on Pt ₁₃ H _m /NaY at 500 mbar: initial sample, and after one, two, and three-fold CO adsorption-desorption cycles.....	81

5.10 EPR spectra of $\text{Pt}_2(\text{CO})_m/\text{NaY}$ sample recorded at 20 K and corresponding simulation.....	85
5.11 Schematic structure of $\text{Pt}_2(\text{CO})_m$ along with the possible types of CO bonding....	88
6.1 The representation of the <i>d</i> -band in bulk Pt metal and of the energy level structures and populations in Pt_{13} and $\text{Pt}_{13}\text{H}_{30}$	91
6.2 Electronic transitions in L-edge X-ray absorption, and XMCD illustrated in a one-electron model.....	93
6.3 XAS at the L_3 and L_2 edges of the Pt_{13} desorbed and hydrogenated compounds. Comparison of XAS spectra at the L_3 and L_2 edges of the Pt_{13} desorbed hydrogenated, Pt metal film, and Au metal film.....	96
6.4 XMCD measurements at the L_3 and L_2 edges of the Pt_{13} and Pt_{13}H_m samples.	98
6.5 Comparison of $M(H)$ curves of SQUID an XMCD results.....	99
6.6 Fit of XMCD data to the Langevin equation.....	103
6.7 Fit of XMCD data to the Langevin equation, with $\chi_0=0$	103
6.8 Fit of XMCD data to the Langevin equation with μ at fixed to the values from the fits to data in Ref [7].....	104

List of Tables

Table 2.1: Calculated average charge q_o on oxygen.....	19
Table 4.1: Fit results of all EXAFS data of calcined Pt in zeolites.....	41
Table 4.2: EPR parameters from simulation of Pt species.....	45
Table 4.3: Fraction of total EPR active Pt species.....	50
Table 4.4: Carbonyl complexes observed in this study and some literature data.....	55
Table 5.1: Fit results of all EXAFS data.....	74
Table 5.2: EPR parameters from spectral simulation obtained with Pt samples.....	86
Table 6.1: Parameters determined from XAS and XMCD measurements.....	95
Table 6.2: Fit parameters and derived information from Ref. [7].....	101
Table 6.3: Fit parameters and magnetic moments deduced from the $\chi(T)$ data of Ref. [7].....	102
Table 6.4: Fit parameters for Eq.6.1, to the SQUID and XMCD data of Pt ₁₃	104
Table 6.5: Comparison of magnetic moment constants for Pt from this study and literature values.....	106

Bibliography

1. J. Zheng, J. L. Dong, and Q. H. Xu, *Stud. Surf. Sci. Catal.*, 1994, **84**, 1641.
2. M. S. Tzou, B. K. Teo, and W. M. H. Sachtler, *J. Catal.*, 1988, **113**, 220.
3. W. M. H. Sachtler, *Catal. Today*, 1992, **15**, 419.
4. Z. Jusys, and R. J. Behm, *J. Phys. Chem. B*, 2001, **105**, 10874.
5. S. Ciccariello, A. Benedetti, F. Pinna, G. Strukul, W. Juszczyk, and H. Brumberger, *Phys. Chem. Chem. Phys.*, 1999, **1**, 367.
6. Y. Yamamoto, T. Miura, Y. Nakae, T. Teranishi, M. Miyake, and H. Hori, *Physica B*, 2003, **329**, 1183.
7. X. Liu, M. Bauer, H. Bertagnolli, J. van Slageren, F. Phillipp, and E. Roduner, *Phys. Rev. Lett.*, 2006, **97**, 253401.
8. X. Liu, H. Dilger, R. A. Eichel, J. Kunstmann, and E. Roduner, *J. Phys. Chem. B*, 2006, **110**, 2013.
9. T. Schmauke, R. A. Eichel, A. Schweiger, and E. Roduner, *Phys. Chem. Chem. Phys.*, 2003, **5**, 3076.
10. V. L. Zholobenko, G. D. Lei, B. T. Carvill, B. A. Lerner, and W. M. H. Sachtler, *J. Chem. Soc. Faraday Transactions*, 1994, **90**, 233.
11. J. Novakova, L. Kubelkova, L. Brabec, Z. Bastl, N. Jaeger, and G. Schulz-Ekloff, *Zeolites*, 1996, **16**, 173.
12. J. Novakova, *Phys. Chem. Chem. Phys.*, 2001, **3**, 2704.
13. K. Chakarova, K. Hadjiivanov, G. Atanasova, and K. Tenchev, *J. Mol. Catal. Chem.*, 2007, **264**, 270.
14. G. J. Li, T. Fujimoto, A. Fukuoka, and M. Ichikawa, *Catal. Lett.* 1992, **12**, 171.
15. T. Schmauke, E. Moller, and E. Roduner, *Chem. Comm.*, 1998, **23**, 2589.
16. J. R. Katzer, G. C. A. Schuit, and J. H. C. Vanhooff, *J. Catal.*, 1979, **59**, 278.

17. K. Chakarova, M. Mihaylov, and K. Hadjiivanov, *Microporous and Mesoporous Mater.*, 2005, **81**, 305.
18. A. Raizman, A. Schoenberg, and J. T. Suss, *Phys. Rev. B*, 1979, **20**, 1863.
19. S. Geschwind, and J. P. Remeika, *J. Appl. Physics*, 1962, **33**, 370.
20. R. A. J. van Santen, *J. Chem. Soc., Faraday Trans*, 1987, **8**, 1915.
21. B. L. Mojet, M. J. Kappers, J. T. Miller, and D. C. Koningsberger, 11th International Congress on Catalysis - 40th Anniversary, 1996, **101**, 1165.
22. M. J. Kappers, J.T. Miller, and D. C. Koningsberger, *J. Phys. Chem.*, 1996, **100**, 3227.
23. Y. Akdogan, C. Vogt, M. Bauer, H. Bertagnolli, L. Giurgiu, and E. Roduner, *Phys. Chem. Chem. Phys.*, 2008, **10**, 2952.
24. B. L. Mojet, J. T. Miller, and D. C. Koningsberger, *J. Phys. Chem. B*, 1999, **103**, 2724.
25. A. Y. Stakheev, E. S. Shpiro, N. I. Jaeger, and G. Schulz-Ekloff, *Catal. Lett.*, 1995, **34**, 293.
26. B. L. Mojet, and D. C. Koningsberger, *Catal. Lett.*, 1996, **39**, 191.
27. B. Xu, and L. Kevan, *J. Chem. Soc. Faraday Transactions*, 1991, **87**, 2843.
28. J. Michalik, and L. Kevan, *J. Amer. Chem. Soc.*, 1986, **108**, 4247.
29. J. Zielinski, *J. Phys. F-Metal Physics*, 1977, **7**, 1973.
30. E. Roduner, *Chem. Soc. Rev.*, 2006, **35**, 583.
31. R. M. Milton, in *Molecular Sieves*, Soc. Chem. Ind, London, 1968, p. 199.
32. E. M. Flanigen, *Stud. Surf. Sci. Catal.*, 1991, **58**, 13.
33. *Database of Zeolite Structures, International Zeolite Association.*
34. D. W. Breck, *Zeolite Molecular Sieves*, Robert Krieger Publishing Company, 1984.
35. J. Warzywoda, and R. W. Thompson, *Zeolites*, 1991, **11**, 577.
36. W. Loewenstein, *Amer. Mineral.*, 1954, **39**, 92.

37. F. Porcher, M. Souhassou, H. Graafsma, A. Puig-Molina, Y. Dusausoy, and C. Lecomte, *Acta Crystallographica Section B-Structural Science*, 2000, **56**, 766.
38. Union Carbide, French Patent, 128613, 1962.
39. F. Delprato, PhD Thesis, Universite de Haute Alsace, 1989.
40. S. Buttefey, A. Boutin, C. Mellot-Draznieks, and A. H. Fuchs, *J. Phys. Chem. B*, 2001, **105**, 9569.
41. P. Fletcher, and R. P. Townsend, *Zeolites*, 1983, **3**, 129.
42. D. Barthomeuf, *Stud. Surf. Sci. Catal.*, 1980, **5**, 55.
43. D. Barthomeuf, *Stud. Surf. Sci. Catal.*, 1991, **65**, 157.
44. E. Zavoisky, *J. Phys. U.S.S.R*, 1945, **9**, 211.
45. N. F. Ramsey, *Bull. Magn. Reson*, 1985, **7**, 94.
46. J. A. Weil, and J. R. Bolton, *Electron Paramagnetic Resonance Elementary Theory and Practical Applications*, Wiley Interscience, 2007.
47. J. R. Morton, and K. F. Preston, *J. Magn. Reson.*, 1978, **30**, 577.
48. J. H. Sinfelt, and G.D. Meitzner, *Accounts Chem. Res.*, 1993, **26**, 1.
49. F. K. Richtmyer, S.W. Barnes, and E. Ramberg, *Phys. Rev.*, 1934, **46**, 0843.
50. G. Meitzner, G. H. Via, F. W. Lytle, and J. H. Sinfelt, *J. Phys. Chem.*, 1992, **96**, 4960.
51. W. Coffey, Y. P. Kalmykov, and J. T. Waldron, *The Langevin Equation*, World Scientific, 1996.
52. E. Roduner, *Nanosopic Materials Size-Dependent Phenomena*, RSC, 2006.
53. K. I. Hadjiivanov, and G. N. Vayssilov, *Adv. Catal.*, 2002, **47**, 307.
54. R. I. Masel, *Principles of Adsorption and Reaction on Solid Surfaces*, Wiley, 1996.
55. N. Sheppard, and T. T. Nguyen, *Adv. Infrared Raman Spectrosc.*, 1978, **5**, 67.
56. M. Hohne, *Phys Rev B Condens Matter*, 1992, **45**, 5883.
57. F. M. Hoffmann, *Surface Science Reports*, 1983, **3**, 107.
58. P. Bazin, O. Saur, J.C. Lavalley, M. Daturi, and G. Blanchard, *Phys. Chem. Chem. Phys.*, 2005, **7**, 187.

59. G. Doyen, and G. Ertl, *Surf. Sci.*, 1974, **43**, 197.
60. G. Blyholder, *J. Phys. Chem.*, 1964, **68**, 2772.
61. M. Mihaylov, K. Chakarova, K. Hadjiivanov, O. Marie, and M. Daturi, *Langmuir*, 2005, **21**, 11821.
62. M. J. Kappers, and J. H. Vandermaas, *Catal. Lett.*, 1991, **10**, 365.
63. L. C. deMenorval, A. Chaqroune, B. Coq, and F. Figueras, *J. Chem. Soc. Faraday Transactions*, 1997, **93**, 3715.
64. A. Trovarelli, *Catal. Rev.*, 1996, **38**, 439.
65. S. P. Mehandru, and A. B. Anderson, *J. Phys. Chem.*, 1989, **93**, 2044.
66. D. W. Daniel, *J. Phys. Chem.*, 1988, **92**, 3891.
67. M. Primet, J. M. Basset, M. V. Mathieu, and M. Prettre, M., *J. Catal.*, 1973, **29**, 213.
68. M. Newville, P. Livins, Y. Yacoby, J. J. Rehr, and E. A. Stern, *Phys. Rev. B*, 1993, **47**, 14126.
69. T. S. Ertel, H. Bertagnolli, S. Huckmann, U. Kolb, and D. Peter, *Appl. Spectrosc.*, 1992, **46**, 690.
70. S. J. Gurman, N. Binsted, and I. Ross, *J. Phys. C*, 1984, **17**, 143.
71. E. A. Stern, *Phys. Rev. B.*, 1993, **48**, 9825.
72. N. Binsted, in *EXCURV98: CCLRC Daresbury Laboratory computer program manual*, CCLRC, Daresbury, 1998.
73. M. Newville, *J. Synchrotron Rad.*, 2001, **8**, 322.
74. M. Newville, *J. Synchrotron Rad.*, 2005, **12**, 537.
75. J. F. Jia, Y. Kou, L. W. Lin, Z. S. Xu, T. Zhang, J. Z. Niu, and D. B. Liang, *React. Kinetics and Catal. Lett.*, 1998, **63**, 391.
76. P. Bera, K. R. Priolkar, A. Gayen, P. R. Sarode, M. S. Hegde, S. Emura, R. Kumashiro, V. Jayaram, and G. N. Subbanna, *Chem. Mater.*, 2003, **15**, 2049.
77. K. Dyrek, and M. Che, *Chem. Rev.*, 1997, **97**, 305.
78. D. Goldfarb, M. Bernardo, K. G. Strohmaier, D. E. W. Vaughan, and H. Thomann, *J. Amer. Chem. Soc.*, 1994, **116**, 6344.

79. A. Watterich, R. Voszka, H. Sothe, and J. M. Spaeth, *J. Phys. C*, 1987, **20**, 3155.
80. G. Damian, V. Miclaus, O. Cozar, M. Todica, L. David, V. Chis, D. Ristoiu, and S. Farcas, *J. Mol. Struct.*, 1999, **483**, 287.
81. J. A. Hodges, R. A. Serway, and S. A. Marshall, *Phys. Rev.*, 1966, **151**, 196.
S. Huber, and H. Knozinger, *Appl. Catal.*, 1999, **181**, 239.
83. G. Hubner, G. Rauhut, H. Stoll, and E. Roduner, *E., Phys. Chem. Chem. Phys.*, 2002, **4**, 3112.
84. A. Delabie, K. Pierloot, M. H. Groothaert, B. M. Weckhuysen, and R. A. Schoonheydt, *Microporous and Mesoporous Mater.*, 2000, **37**, 209.
85. F. E. Mabbs, *Chem. Soc. Rev.*, 1993, **22**, 313.
86. R. J. VanZee, and W. Weltner, *Chem. Phys. Lett.*, 1997, **266**, 403.
87. P. J. Alonso, R. Alcalá, R. Uson, and J. Fornies, *J. Phys. Chem. Solids*, 1991, **52**, 975.
88. L. M. Giurgiu, *Studia Universita Babeş-Bolyai, Physica XLVIII*, 2003, **85**.
89. T. Ishiyama, T. Fukuda, Y. Yamashita, and Y. Kamiura, *Physica B*, 2006, **376**, 89.
90. T. Krigas, and M.T. Rogers, *J. Chem. Phys.*, 1971, **55**, 3035.
91. A. J. Freeman, J. N. Mallow, and P. S. Bagus, *J. Appl. Phys.*, 1970, **41**, 1321.
92. R. E. Watson, and A. J. Freeman, *Hyperfine Interactions*, Academic Press, New York, 1967.
93. E. Simanek, Z. Sroubek, K. Zdansky, J. Kaczer, and L. Novak, *Phys. Status Solidi*, 1966, **14**, 333.
94. X. Liu, PhD Thesis, University of Stuttgart, 2006.
95. M. G. Samant, and M. Boudart, *J. Phys. Chem.*, 1991, **95**, 4070.
96. D. C. Koningsberger, B. Mojet, J. Miller, and D. E. Ramaker, *J. Synchrotron Rad.*, 1999, **6**, 135.
97. D. C. Koningsberger, M. K. Oudenhuijzen, J. H. Bitter, and D. E. Ramaker, *Top. Catal.*, 2000, **10**, 167.
98. Y. Y. Ji, A. M. J. van der Eerden, V. Koot, P. J. Kooyman, J. D. Meeldijk, B. M. Weckhuysen, and D. C. Koningsberger, *J. Catal.*, 2005, **234**, 376.

99. R. J. Goodfellow, I. R. Herbert, and A. G. Orpen, *J. Chem. Soc. Chem. Comm.*, 1983, **23**, 1386.
100. Torigoe, K., H. Remita, G. Picq, J. Belloni, and D. Bazin, *J. Phys. Chem. B*, 2000, **104**, 7050.
101. E. P. Kundig, D. Mcintosh, M. Moskovit, and G. A. Ozin, *J. Amer. Chem. Soc.*, 1973, **95**, 7234.
102. M. Doerr, and G. Frenking, *ZAAC*, 2002, **628**, 843.
103. J. Weitkamp, and L. Puppe, *Catalysis and Zeolites*, Springer, 1999.
104. H. J. Vonbardeleben, D. Stievenard, M. Brousseau, and J. H. J. Barrau, *Phys. Rev. B*, 1988, **38**, 6308.
105. G. Blyholder, *J. Phys. Chem.*, 1975, **79**, 756.
106. T. Visser, T. A. Nijhuis, A. M. J. van der Eerden, K. Jenken, Y. Y. Ji, W. Bras, S. Nikitenko, Y. Ikeda, M. Lepage, and B. M. Weckhuysen, *J. Phys. Chem. B*, 2005, **109**, 3822.
107. Q. Xu, Y. Souma, B. T. Heaton, C. Jacob, and K. Kanamori, *Angew. Chem. Int. Ed.*, 2000, **39**, 208.
108. R. M. Watwe, B. E. Spiewak, R. D. Cortright, and J. A. Dumesic, *Catal. Lett.*, 1998, **51**, 139.
109. H. F. J. Van't blik, J. B. A. D. Vanzon, T. Huizinga, J. C. Vis, D. C. Koningsberger, and R. Prins, *J. Amer. Chem. Soc.*, 1985, **107**, 3139.
110. H. F. J. Van't blik, J. B. A. D. Vanzon, D. C. Koningsberger, and R. Prins, *J. Mol. Catal.*, 1984, **25**, 379.
111. L. L. Sheu, H. Knozinger, and W. M. H. Sachtler, *J. Amer. Chem. Soc.*, 1989, **111**, 8125.
112. V. Kumar, and Y. Kawazoe, *Phys. Rev. B*, 2002, **66**, 144413.
113. J. Stohr, *J. Magn. Magn. Mater.*, 1999, **200**, 470.
114. J. L. Erskine, and E. A. Stern, *Phys. Rev. B*, 1975, **12**, 5016.
115. J. Stohr, and R. Nakajima, *J. Res. Develop.*, 1998, **42**, 73.
116. J. Als-Nielsen, and D. McMorrow, *Phys. Rev. Lett.*, 1993, **70**, 694.

118. B. T. Thole, P. Carra, F. Sette, and G. B. T. Vanderlaan, *Phys. Rev. Lett.*, 1992, **68**, 1943.
119. A. Rogalev, private communication.
120. I. Galanakis, M. Alouani, and H. Dreysse, *J. Magn. Magn. Mater.*, 2002, **242**, 27.
121. C. Antoniak, J. Lindner, M. Spasova, D. Sudfeld, M. Acet, M. Farle, K. Fauth, U. Wiedwald, H. G. Boyen, P. Ziemann, F. Wilhelm, A. Rogalev, and S. H. Sun, *Phys. Rev. Lett.*, 2006, **97**, 117201.
122. J. Geissler, E. Goering, M. Justen, F. Weigand, G. Schutz, J. Langer, D. Schmitz, H. Maletta, and R. Mattheis, *Phys. Rev. B*, 2002, **65**, 020405.
123. W. Grange, I. Galanakis, M. Alouani, M. Maret, J. P. Kappler, and A. Rogalev, *Phys. Rev. B*, 2000, **62**, 1157.
124. W. Grange, M. Maret, J. P. Kappler, J. Vogel, A. Fontaine, F. Petroff, G. Krill, A. Rogalev, J. Goulon, M. Finazzi, and N. B. Brookes, *Phys. Rev. B*, 1998, **58**, 6298.
125. N. Jaouen, D. Babonneau, J. M. Tonnerre, D. Carbone, F. Wilhelm, A. Rogalev, T. K. Johal, and G. van der Laan, *Phys. Rev. B*, 2007, **76**, 104421.
126. P. Pouloupoulos, M. Angelakeris, E. T. Papaioannou, N. K. Flevaris, D. Niarchos, M. Nyvlt, V. Prosser, S. Visnovsky, C. Mueller, P. Fumagalli, F. Wilhelm, and A. Rogalev, *J. Appl. Phys.*, 2003, **94**, 7662.

Curriculum Vitae

Yaşar Akdoğan

Born on March 09th, 1981 in Aksaray, Turkey

School Education:

1987 - 1992 Primary school education at Genç Osman İlkokulu in Aksaray, Turkey

1992 - 1996 Secondary school education at Hazım Kulak Anadolu Lisesi in Aksaray, Turkey.

1996 - 1999 Higher secondary school education at Fen Lisesi in Aksaray, Turkey

College Education:

Sep 1999 - June 2004

Studied B.Sc. in Chemistry at the Bilkent University, Ankara, Turkey

Sep 2004 - Jan 2006

Studied M.Sc. in Chemistry at the Bilkent University, Ankara, Turkey

Thesis Title: Synthesis and Characterization of CdS, ZnS and $Zn_xCd_{1-x}S$ Nanoparticles.

Advisor: Prof. Dr. Ömer Dağ

Doctoral Work:

Feb 2006 – Feb 2009

Doctoral work at the Institute of Physical Chemistry, University of Stuttgart, Stuttgart, Germany

Thesis Title: Synthesis, Characterization and Chemical Behaviour of Small Paramagnetic Pt Species inside Zeolites Studied by EPR, XAS and FTIR.

Advisor: Prof. Dr. Emil Roduner